

University of Genoa
Faculty of Engineering
DICAT

Royal Institute of Technology of Stockholm
Department of Mechanics
Linné Flow Centre



Master's thesis

A Numerical Model of Retinal Detachment

Supervisor: Prof. Jan Pralits

Co-supervisors: Prof. Rodolfo Repetto
Prof. Shervin Bagheri

Author: Rondanina Emanuele

May 2014

Abstract

The retinal detachment is a common pathology of the human eye which involves the separation of the sensory retina from the underlying retinal pigment epithelium. There are numerous variations in the pathogenesis of a retinal detachment. They include developmental factors, as myopia, that affect the overall size and shape of the globe; vitreoretinal disorders; metabolic disease; trauma; inflammation and degenerative conditions. A retinal detachment can have devastating visual consequences depending on its displacement and extent. If the detachment reaches the macula, the most sensitive part of the eye, the patient could experience a significant reduction of his field of vision or lose his eyesight in the worst cases.

The retinal detachment could be divided into rhegmatogenous and nonrhegmatogenous detachment, where the difference is due to the presence of a break in the neurosensory retina. In the first case a vitreous traction generates a break, called *retinal tear*, while in the second case the detachment is formed without any break. In this thesis we analyzed two types of rhegmatogenous detachments, called *retinal break* and *retinal hole*. The first type occurs when a localized traction generates a break inside the retinal layer, leading to a flap which is free to move. The second type is characterized by the presence of an hole inside the retinal layer, due to the action of the vitreous humor which is able to remove a certain area of the retina. The thesis is focused on the study of the forces the detached retina exerts on the regions not affected by this pathology, in order to verify which type of detachment facilitates a further separation.

This work has been developed through virtual experiments in a two dimensional domain, where the eye wall has been considered as a flat surface, while the detached retina is approximated using clamped filaments. We used a modified version of the *Fractional Step Method* to solve the fluid dynamics, while the *Immersed Boundary Method* is adopted to take in account the interaction between the filament and the fluid.

An existing code has been modified using the geometry of our problem and the parameters defining the retina. From our simulations we observed how in presence of a *retinal hole* higher forces are generated on the attached point leading to a further detachment. We also demonstrated how the filaments act in compression, on the surface to which they are clamped, during the accelerated phase of the saccade, while in the following deceleration phase a traction force is mostly applied. Eventually we analyzed the dependence of the forces and torque on the parameters we used, obtaining the following results. Considering the *retinal hole* the exerted force increases with the length of the filaments, while the torque does not have a significant dependence on the length for both cases.

Sommario

Il distacco della retina é una comune patologia dell'occhio umano che riguarda la separazione della neuroretina dal sottostante epitelio pigmentato. Le cause che possono portare a tale difetto sono molteplici, queste possono includere fattori di sviluppo che influenzano le dimensioni e la forma del globo oculare, come la miopia; disturbi legati al corpo vitreo; fattori metabolici; malattie vascolari; traumi; infiammazioni e condizioni degenerative. Il distacco di retina puó avere devastanti conseguenze sulla vista del soggetto a seconda della sua localizzazione e grandezza. Se infatti il distacco dovesse raggiungere la macula, ossia la parte piú sensibile agli stimoli luminosi, il soggetto potrebbe subire una restrizione significativa del suo campo visivo o perdere quasi del tutto la vista.

Il distaccamento retinico viene diviso in regmatogeno e non regmatogeno, a seconda dalla presenza o meno di uno strappo nella neuroretina. Nel primo caso la trazione esercitata dal corpo vitreo genera una rottura, definita *retinal tear*, mentre nel secondo caso il distacco si manifesta senza alcuna rottura. In questa tesi vengono presi in analisi due tipi di distaccamenti regmatogeni denominati *retinal breaks* e *retinal holes*. I primi si verificano quando una trazione localizzata genera una rottura nel tessuto retinico, portando alla formazione di un lembo libero di muoversi. I *retinal holes* sono invece caratterizzati dalla mancanza di una determinata sezione della retina, staccatasi sempre a causa dell'azione del corpo vitreo. La tesi si concentra sullo studio delle forze che la retina distaccata esercita sui punti non ancora affetti dalla patologia, al fine di verificare quale caso favorisce un'ulteriore separazione.

Questo studio é stato sviluppato tramite delle simulazioni virtuali svoltesi in un dominio bidimensionale, dove la parete dell'occhio é stata considerata come una superficie piana, mentre la parte di retina distaccata é approssimata tramite dei filamenti incastrati. Tali simulazioni sfruttano una versione modificata del metodo *Fractional Step* per la soluzione della dinamica del fluido ed il metodo *Immersed Boundary* per l'interazione tra il filamento ed il fluido. Un codice esistente é stato modificato applicando la geometria del nostro problema ed i parametri che definiscono la retina. Dalle simulazioni effettuate abbiamo potuto osservare come in presenza di *retinal holes* vengano generate delle forze maggiori sul punto di attacco che favoriscono la propagazione del distacco. Abbiamo inoltre dimostrato come i filamenti esercitino un'azione di compressione durante la fase di accelerazione della saccade, mentre nella fase successiva di decelerazione viene applicata prevalentemente una forza in trazione. Infine analizzando la dipendenza della forza e dei momenti dai parametri utilizzati abbiamo ricavato i seguenti risultati. Nel caso di *retinal holes* la forza esercitata cresce all'aumentare della lunghezza dei filamenti, mentre per entrambi i casi il momento non ha una significativa dipendenza dalla lunghezza considerata.

Contents

1	The human eye	7
1.1	Anatomy of the eye	7
1.2	Retinal Disease	8
1.2.1	Retinal Detachment	9
1.2.2	Retinal Breaks	10
1.3	Clinical management	11
1.3.1	Scleral Buckling	11
1.3.2	Pneumatic Retinopexy	12
2	Review of the existing models of retinal detachment	16
2.1	Saccadic eye movement	16
2.2	Models for Retinal Detachment	18
3	Formulation of the problem	21
3.1	The model	21
3.2	The Immersed Boundary Method	22
3.3	Filament Models	25
3.3.1	The method by Newren <i>et al.</i>	25
3.3.2	The method by Huang <i>et al.</i>	26
3.4	Boundary conditions	26
3.4.1	The method by Newren <i>et al.</i>	27
3.4.2	The method by Huang <i>et al.</i>	28
3.5	Time and spatial discretization	30
3.5.1	Navier-Stokes equation	30
3.5.2	Eulerian force density and filament velocity	32
3.5.3	Filament motion equation	32
3.5.4	The method by Newren <i>et al.</i>	32
3.5.5	The method by Huang <i>et al.</i>	34
3.6	The staggered grid	35
4	Simulations and results	38
4.1	Numerical Implementation	38
4.1.1	Grid convergence	38
4.1.2	Defining the computational domain	40
4.2	Configuration of the simulations	44
4.3	Results with Newren <i>et al.</i> model	46
4.4	Results with Huang <i>et al.</i> model	53

5	Conclusions and future developments	74
6	Acknowledgments	81
	Bibliography	89

Chapter 1

The human eye

1.1 Anatomy of the eye

The eye is the organ of the visual system and is designed to acquire environment information, converting light into electrical signals. These signals are sent through the optic nerve to the brain for the further processing necessary for perception.

The eye is a slightly deformed sphere, composed by three layers of tissue, which enclose a gel-like fluid, the vitreous humour. The outer layer is composed of a tough white fibrous tissue, the sclera, which contain collagen and elastic fibers. At the front of the eye, this layer is transformed into the cornea, a specialized transparent tissue that permits light rays to enter the eye. The middle layer of tissue includes three distinct but continuous structures: the iris, the ciliary body, and the choroid. The iris is the colored portion of the eye that can be seen through the cornea. It contains two sets of muscles with opposing actions, which allow the size of the pupil to be adjusted under neural control. The ciliary body is a ring of tissue that encircles the lens and includes a muscular component that is important for adjusting the refractive power of the lens, and a vascular component that produces the fluid that fills the front of the eye. The choroid is composed of a rich capillary bed that serves as the main source of blood supply for the photoreceptors of the retina and it's formed by connective tissue. The innermost layer, the retina, is the light sensitive part of the eye. It contains neurons that are sensitive to light and are capable of transmitting visual signals to the brain through the fibers in the optic nerve.

The light, in order to reach the retina, passes through the cornea, the lens, and two distinct fluid environments, the aqueous humour and the vitreous humour. The anterior chamber, the space between the lens and the cornea, is filled with aqueous humor, a transparent watery liquid that supplies nutrients to the posterior cornea, the lens and the anterior vitreous. It also maintains the intraocular pressure (IOP), which is an important parameter for the eye health since high values of IOP are correlated with the occurrence of glaucoma, a very serious sight threatening condition. The aqueous humour is produced by the ciliary processes in the posterior chamber, which is the region between the lens and the iris, and flows into the anterior chamber through the pupil. A specialized meshwork of cells that lies at the junction of the iris and the cornea is responsible for its uptake. Under normal conditions, the rates of aqueous humor production and uptake are in equilibrium, ensuring a

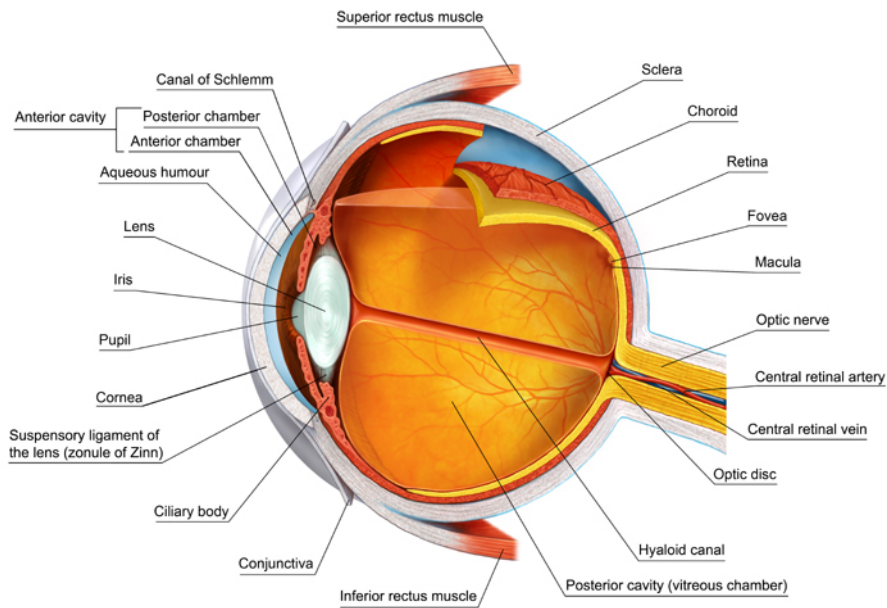


Figure 1.1: Vertical sagittal section of human eye.

constant intraocular pressure.

The space between the back of the lens and the surface of the retina is filled with a thick, gelatinous substance called the vitreous humour, which accounts for about 80% of the volume of the eye. In addition to maintaining the shape of the eye, the vitreous humor contains phagocytic cells that remove blood and other debris that might otherwise interfere with light transmission.

The light eventually reaches the macula, which is an oval-shaped highly pigmented spot near the center of the retina that gives central vision. Near its center there is the fovea, a small pit that contains the largest concentration of cone cells in the eye and it is responsible for high resolution vision.

1.2 Retinal Disease

The retina is a thin layer of neural tissue that lines the back of the eye. It is part of the central nervous system and its neural network converts the electrical activity of photoreceptors into action potentials that travel to the brain via axons in the optic nerve.

The retina is formed by different layers of neurons, displaced between the nerve fiber layer, which is the inner part of the retina, and the pigment epithelium, which is the outer part. This epithelium is a thin structure containing melanin that reduces backscattering of the light that enters the eye. It also plays a critical role in the regulation and maintenance of photoreceptors. There are two types of photoreceptors: rods and cones. Rods function mainly in dim light and provide black-and-white vision, while cones support daytime vision and the perception of color.

There is no real anatomic junctions between the cells of the neurosensory retina

(NSR) and the retinal pigment epithelium (RPE), therefore the forces of adhesion between these two layers are weak. They can be classified into mechanical and metabolic forces.

Mechanical factors are also divided into those outside and those inside the subretinal space. The first type include fluid and vitreous pressures. The aqueous humor usually exits the eye mainly through the trabecular meshwork, however a small aqueous fraction tends to exit from the vitreous space to the choroid, due to intraocular and choroidal oncotic pressures. Since the retina and retinal pigment epithelium resist to this fluid flow, this fluid movement tends to push the retina against the RPE. Mechanical forces inside the subretinal space include matrix material between the NSR and RPE, which act as a glue, and the connection between the RPE microvilli and the photoreceptors [1].

Metabolic factors that affect retinal adhesion include oxygenation. Retinal adhesion decreases tremendously postmortem and is restored with oxygenation.

There are several diseases that might affect the retina. In this thesis we consider the mechanics associated with breaks and retinal detachment. These could occur when the forces of adhesion between the NSR and the RPE are overwhelmed due to different mechanisms. Regardless of the mechanism, all types of retinal detachments and retinal breaks have one characteristic in common, the accumulation of subretinal fluid.

1.2.1 Retinal Detachment

A retinal detachment is a separation of the sensory retina from the underlying retinal pigment epithelium. There are numerous variations in the pathogenesis of a retinal detachment. They include developmental factors, as myopia, that affect the overall size and shape of the globe; vitreoretinal disorders, as retinal dysplasia; metabolic disease, such as diabetic retinopathy; vascular disease; trauma; inflammation and degenerative conditions.

Retinal detachments can be classified as rhegmatogenous or nonrhegmatogenous.

Rhegmatogenous Retinal Detachment

This is the most common type of retinal detachment and results from a break in the sensory retina. The break is most often caused by vitreous traction on the surface of the retina. This traction physically pulls a small section of the sensory retina away from the pigment epithelium, resulting in what is called a *retinal tear*. Traction at the tear flaps can initiate retinal detachment surrounding the tear by pulling on the surface of the adjacent retina. The break in the retina may also cause fluid from the vitreous cavity to flow into the subretinal space. Thus, a rhegmatogenous retinal detachment caused by a retinal tear is the result of both vitreous traction and fluid flow into the potential space between the sensory retina and the pigment epithelium.

Nonrhegmatogenous Retinal Detachment

This type of retinal detachment could occur in two cases. The most common results from the accumulation of subretinal fluid in the subretinal space, due to a damage of

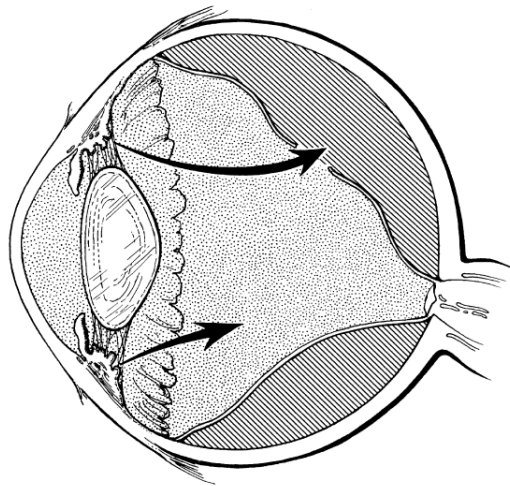


Figure 1.2: Posteriorly directed fluid flow through the vitreous into the subretinal space in an eye with rhegmatogenous retinal detachment.

the RPE, induced for instance by as hypertension, rather than from a retinal break. Sometimes a nonrhegmatogenous retinal detachment is caused by shear traction, without the production of a retinal tear.

1.2.2 Retinal Breaks

Any discontinuity of the neurosensory retina is called a retinal break. When a break results from vitreous traction, it is referred to as a *tear*, while when the break results from a focal loss of retinal tissue, it is atrophic and it is referred to as a *retinal hole*

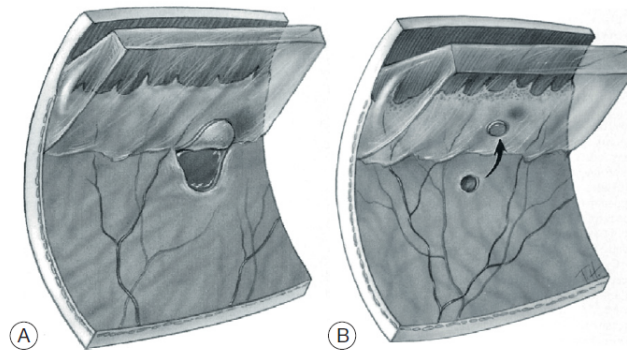


Figure 1.3: Irregular posterior extensions of the vitreous due to horseshoe-shaped retinal tears (A) and retinal hole with a free operculum (B).

Atrophic Retinal Holes

Atrophic retinal holes are retinal break that is not caused by viterous traction but are produced by an atrophic process, typically due to vascular insufficiency of the

underlying choriocapillaris. Thinning and degeneration of blood vessels eventually lead to the clinical appearance of small, round defects in area where the retina is thinner. Most retinal holes occur in the temporal half of the retina and are usually confined to the region between the equator and the ora serrata.

Horseshoe and Linear Retinal Tears

Significant localized vitreous traction can cause horseshoe (flap) or linear retinal tears. Horseshoe tears, which are much more common than linear tears, are the results of vitreous traction pulling a horseshaped thin curvilinear flap of sensory retina into the vitreous cavity. Pulled away from its blood supply, this flap which is attached at the anterior margin of the tear, contracts to become smaller than the break. Such tears can exist in any region of the peripheral retina.

1.3 Clinical management

The treatment an ophthalmologist can choose in order to deal with a retinal break or detachment may vary, depending on the state of the patient. Among the treatments used the most important are scleral buckling, often associated with vitrectomy and pneumatic retinopexy.

1.3.1 Scleral Buckling

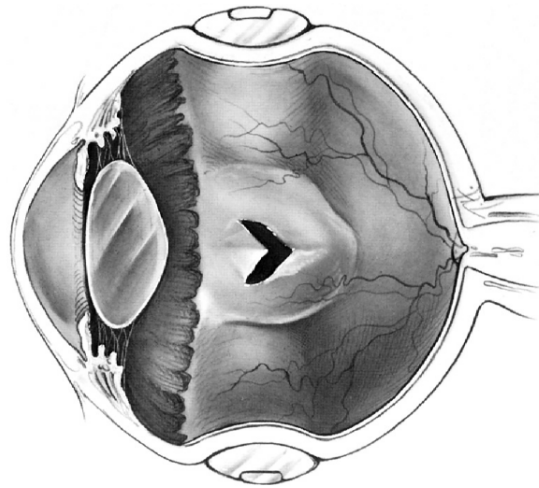


Figure 1.4: Retinal tear with an encircling buckle.

This type of surgery consists in sewing an encircling elastic band around the circumference of the sclera of the eye. The buckles are made of either solid silicone rubber or silicone sponges and come in a variety of sizes and shapes. Once the patient is under local or general anesthesia the surgeon could cut the conjunctiva, the thin layer surrounding the sclera, and separates it from the eye ball using blunt

scissors. Thereafter the extraocular muscles are isolated, with a specific hook, in order to allow the disposition of the elastic band which goes around the eye. Once it is fixed to the eyeball, the surgeon proceeds with the vitrectomy. Three holes are performed in order to handle an infusion pump, to keep positive the pressure inside the eye; a light source and a vitrector, the instrument which cuts away the vitreous. The placement of the retinal detachment is locate with precision, no aspect of scleral buckling is more critical than accurate placement of the buckle on the sclera. Only if the buckle is exactly under the retinal break or hole the reattachment of the retina could be achieved. In order to remove the fluid underneath the retina, the humor vitreous around the hole is replaced with air using the vitrector. This will avoid a change of volume of the eye ball. In order to accomplished an adhesion between the RPE and the eye a thermal injury is induced with a laser. The surgeon uses a laser beam around the detachment creating a sort of scar tissue, this will avoid a future detachment through that hole. The air is then replaced with a surgical gas (the most commonly used are sulfur hexafluoride SF_6 , perfluoroethane C_2F_6 and perfluoropropane C_3F_8) or a silicone oil. The gas mixture will be reabsorbed within the next 10 or 14 days while the removal of the silicone oil require an additional procedure. Eventually the conjunctive is sealed.

The scleral buckling technique frequently results in tissue trauma, complications, relatively high expense and use of a hospital or surgical operating room. Pneumatic retinopexy was developed as an attempt to minimize these problems.

1.3.2 Pneumatic Retinopexy

This surgical procedure for retinal reattachment consists of an intavitreal gas injection with transconjunctival cryopexy or laser photocoagulation, followed by appropriate head positioning. Dissimilar to scleral buckling, no cut on the conjunctiva is required, only tiny holes are performed in order to use the surgical instrumentation. Sulfur hexafluoride SF_6 and perfluoropropane C_3F_8 are the most frequently used gasses with retinopexy, success also has been reported with sterile room air. The characteristics of the intraocular bubble are based on three features: buoyancy, surface tension and isolation of retinal tears from intraocular currents. Buoyancy applies upward pressure on the detached retina. The surface tension of the bubble closes the retinal break and prevents the bubble from passing into the subretinal space. With the break closed, the pigment epithelial pump removes the subretinal fluid.

The position and the dimensions of the tear are crucial parameters for the surgery. Referring to a quadrant clock-hour map, as shown in Figure (1.5), breaks spanning more the one clock hour can be treated with retinopexy. Single or multiple tears spanning up to three clock hours pose no particular problem either. Also giant retinal tears have been cured with retinopexy, however scleral buckling or vitrectomy is usually preferred. Most cases involving breaks in the inferior four clock hours of the eye have been difficult to treat with retinopexy.

The surgical procedure starts with topical anesthesia, usually with subconjunctival anesthesia. Pneumatic retinopexy can be done in one session, with cryopexy applied

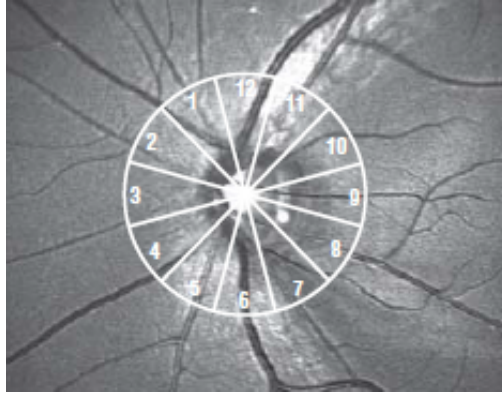


Figure 1.5: Imaginary clock-hour map drawn on the optic nerve.

to the retinal breaks just before gas injection, or as a two-session procedure, with initial gas injection followed by laser photocoagulation one or two days later when the retina is reattached. The first case always involve cryopexy, since laser cannot be applied to detached retina, while laser is required if a tear develops overlying a previously placed scleral buckle, since cryopexy cannot penetrate the silicone.

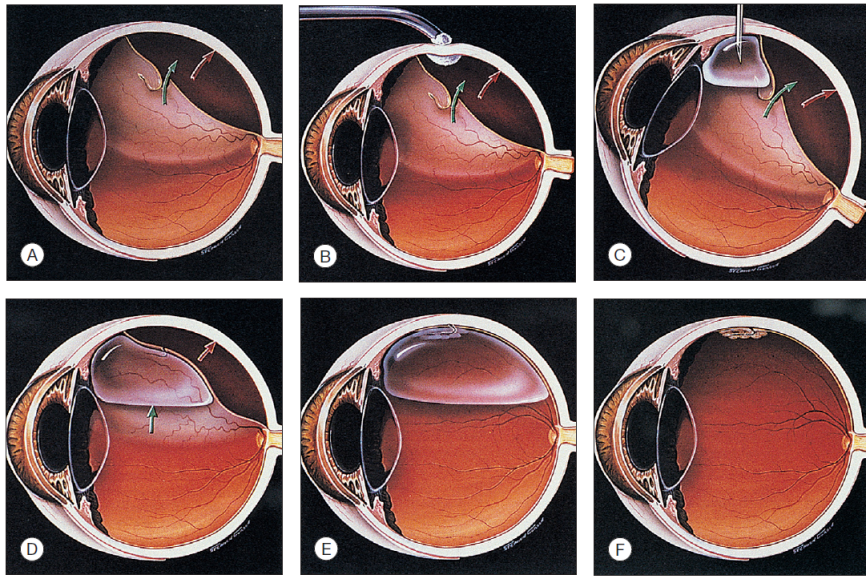


Figure 1.6: Summary of pneumatic retinopexy. A, the volume of the subretinal fluid is determined by inflow of fluid vitreous (green arrow) and the outflow through the retinal pigment epithelial pump into the choroid (red arrow). B, the area of the retinal break is treated with multiple contiguous applications of transconjunctival cryotherapy. C, injection of the gas bubble through the needle. D, the head is positioned so that the intravitreal gas bubble closes the retinal break. E, with the beak closed, the retina usually reattached by the first postoperative day. F, the gas bubble is spontaneously absorbed.

After the sterilization of the ocular surface, a paracentesis is used to prevent the increase of intraocular pressure and to avoid the gas moves inside the anterior chamber. The next step is the intraocular gas injection. The needle is directed toward the center of the vitreous which allows the placement of the gas bubble under the retinal detachment. This procedure requires a gas bubble large enough to cover all detached breaks simultaneously for about five days. After the surgical operation the patients is instructed to maintain a specific head position. The patient is instructed not to lie on his back facing upward because prolonged gas contact with the lens may cause a cataract or, in the case of an aphakic eye, pupillary block with angle-closure galucoma. The appropriate position, with the retinal break uppermost, should be maintained at least during waking hours for 5 days.

Chapter 2

Review of the existing models of retinal detachment

2.1 Saccadic eye movement

In order to simulate the behavior of retinal detachment we first need to consider the characteristics of eye movements, since eyes rotations are the leading mechanisms producing fluid flow in the vitreous chamber [REF].

The eyes are subjected to various kinds of movements. In this thesis we focus on the so-called *saccadic eye movements* that, due to their characteristics, are the main responsible of vitreous motion. A saccade is a fast movement of the eye, which purpose is to acquire the environment information around the subject by redirecting the light towards the fovea. In this way small parts of a scene can be sensed with greater resolution.

Physiologic characteristics of the eye movements are reported in detail in Becker (1989)[2], where it is discussed that the basic features of such movements are the following:

1. a high initial angular acceleration (up to $30\,000\text{s}^{-2}$);
2. a less intense deceleration which is however capable of inducing a very efficient stop of the movement;
3. a peak angular velocity, the value of which is approximately proportional to the saccadic amplitude for small range of rotations and saturate to a maximum value varying between $400\text{ deg}\cdot\text{s}^{-1}$ and $600\text{ deg}\cdot\text{s}^{-1}$ for large amplitude movements;
4. a saccade amplitude which range goes from 0.05° (microsaccades) to 80° - 90° . High saccade amplitudes are accompanied by head rotations.

David *et al.* (1998) [3] have studied the motion of vitreous humour during the saccadic process. Their aim was to demonstrate a relation between retinal detachment and shear stress at the retina during saccadic movements. In particular they wanted to find how the size of the eye influences the retinal detachment. The authors used a thin-shelled sphere in order to model the eyeball and they simulated

the movement with a sinusoidal function, based on the experiments of Weber and Daroff (1972)[4]. They modelled the vitreous humour as a viscoelastic fluid, using a Maxwell-Voigt model. They showed how, in presence of sinusoidal movements, a viscous wave propagates towards the center of the eye and the characteristic length of this wave is a function of the Womersley number. Furthermore they demonstrated that the maximum shear stress is proportional to $R_0\sqrt{\nu^*\omega^3}$ where R_0 is the eye radius, ν^* the complex viscosity and ω the sinusoidal frequency. This result shows that myopic eyes, which are on average larger than normal ones, are at a higher risk of developing retinal detachments.

Repetto *et al.* (2005) [5] proposed an human eye model in order to investigate the motion of the vitreous humor. The vitreous chamber was modelled as a spherical cavity carved within a perspex cylinder which was able to rotate following a prescribed time law. They filled the cavity with glycerol, which is a high viscosity Newtonian fluid, to simulate the behavior of the vitreous humour. In this work the elastic properties of the vitreous must be excluded from the analysis since the previous study of David *et al.* (1998) [3] showed that the elastic component plays a relatively minor role in the flow field with respect to the viscous one and they don't influence the maximum shear stress at the wall, which is the fundamental parameter in the evaluation of retinal detachment. They let the cylinder move with a fifth degree polynomial law simulating in time a real saccadic eye rotation where all the parameters were based on the study made by Becker (1989) [2]. The authors used the following linear law to evaluate the saccade duration :

$$D = D_0 + dA \quad (2.1)$$

where D is the duration, the intercept D_0 typically ranges between 0.02 and 0.03 s, the slope d approximately assumes the value of $0.0025 \text{ s deg}^{-1}$ and A is in the range of 5° A 50° .

The average angular velocity during a saccadic movement was defined as $\bar{\Omega} = A/D$. From the experiments of Becker (1989) the ratio $\Omega_p/\bar{\Omega}$ between the peak and the mean velocities is fairly constant value near to 1.64.

The time law used by Repetto *et al.* [5] in order to describe the angular displacement of the eye is the following :

$$\theta(t) = c_0 + c_1t + c_2t^2 + c_3t^3 + c_4t^4 + c_5t^5 \quad (2.2)$$

The coefficients c_i are computed imposing the following conditions:

1. the initial and final position of the saccade movement are defined as $\theta(0) = 0$ and $\theta(D) = A$;
2. the first derivative of the angular displacement is defined such that $\dot{\theta}(0) = 0$ and $\dot{\theta}(D) = 0$;
3. the value of the maximum velocity corresponds to $\dot{\theta}(t_p) = \Omega_p$;
4. the second derivative of the angular displacement calculated in t_p is equal to zero, $\ddot{\theta}(t_p) = \Omega_p$

conditions of the displacement, velocity and acceleration. Each saccadic movement was then followed by a time of rest with a duration of five times the saccade duration to allow a complete stop of the fluid motion. On Figure (2.1) different saccadic eye movements are shown at different saccadic amplitudes. In this figure the angular velocity is represented by $\Omega(t) = d\theta/dt$.

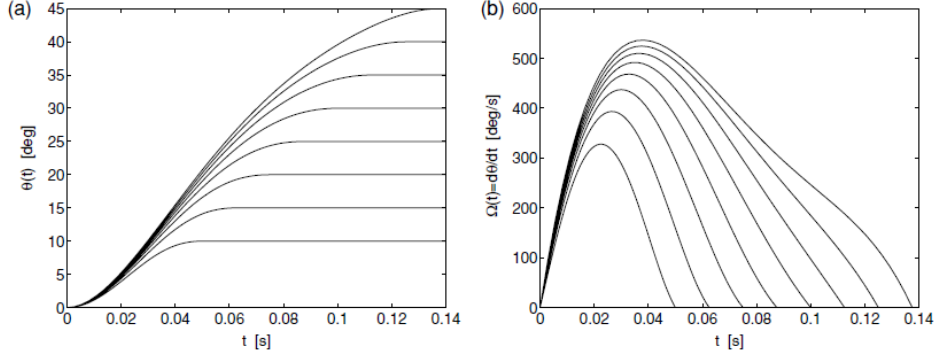


Figure 2.1: Example of saccadic eye movement, at different amplitudes, used by Repetto *et al.* [5]. (a) Angular displacement $\theta(t)$; (b) angular velocity $\Omega(t) = d\theta/dt$.

From this experiment they noticed that the fluid motion, which starts from the rest, is initially confined within a narrow region in close proximity to the wall and its thickness increases with time. Using the measured velocity profiles they derived the shear stresses on the globe showing that during a saccadic movement, both positive and negative shear stresses are exerted on the wall, though the maximum values was positive. This means that the fluid generates a shear stress on the sphere mainly in the opposite direction with respect to the wall motion. Moreover they found that small saccades induce in the inner part of the domain a weaker motion in respect with the motion due to larger saccades. Studying the dependence of maximum shear stress at the wall from the saccade amplitude they demonstrate how a weak correlation can be found between different eye rotations and the maximum shear stress. This means that small amplitude saccade could be as responsible as large amplitude saccade for the retinal detachment. Furthermore, since small amplitude saccade are more common, this implies that they are the main cause of stress on the retina. They also showed that the maximum shear stress increases with the viscosity and for this reason it would be suggested to employ a low viscosity fluid during surgical operations as vitrectomy.

2.2 Models for Retinal Detachment

Different types of models have been studied to analyze the behavior of the detached retina. In this section will be reviewed the fundamental models we referred to in order to set up our own simulations.

Clemens *et al.* (1987) [6] developed an experimental study on the mechanism of retinal detachment after a buckling procedure. Their aim was to demonstrate that

the absorption of subretinal fluid is not only due to a flux through the retinal pigment epithelium, but is also due to the presence of the buckle as an obstacle to fluid movements. The authors used a rectangular glass container filled with water and they glued a waterproof thin film on the bottom surface of the tank. These components simulated the vitreous chamber and the detached retina respectively. Moreover they fixed a plastic tube on the transverse axis of the vessel, underneath the film, to analyze how the buckle influence the flow. After that, they created a retinal hole exactly overlying the buckle. They set on movement the tank using a sinusoidal velocity. They demonstrated that the same fluid movements which cause a retinal detachment are also responsible for the reduction of subretinal fluid in a presence of a scleral buckle. This was achieved only if the buckle was placed beneath the fabric hole, otherwise no reattachment was observed. The authors also proposed a preliminary qualitative analysis. Considering a laminar flow of the fluid against the detached retina, this produced a higher hydrostatic pressure inside the subretinal space inducing a flow through the retinal hole.

Foster *et al.* (2009) [7] tried to model the experiment made by Clemens numerically model using a FEM solver (COMSOL Multiphysics) and performing 2D simulations. They simulated the sclera the indentation created by the scleral buckle as a rigid half circle, placed exactly under the retinal hole. The detached retina was implemented as two horizontally flexible filaments suspended above the rigid sclera. By imposing a laminar fluid flow, they simulated the movement of the subretinal fluid during REM-like movements and slower saccadic eye movements. They demonstrated that the first type of eye movement promote fluid outflow more efficiently than slow reading movements.

In the 2011 Foster [8] proposed a similar model in order to calculate the vitreous traction and detachment forces on the edge of the retinal hole, without a scleral buckle. The model had the same structure proposed in their previous work [7], except for the introduction of a spring between the two end points of the filament, in order to simulate the traction the vitreous humor exerts on the retina. He compared different experimental sets with two different types of velocity, a 400°s^{-1} saccadic eye movement and 15°s^{-1} reading speed, and different directions of traction, downstream and upstream or both of them. He was able to demonstrate how the fluid flow, from the vitreous chamber to the subretinal space, has a minimal dependence on fluid velocity and how a traction applied on both edges of the detached retina increased significantly the amount of subretinal fluid. Eventually he described how traction on retinal hole can create an area of low pressure in the subretinal space.

Regarding the force that the vitreous humour could exerts on the retina Repetto *et al.* proposed two different models (2004 [9] and 2010 [10]) to evaluate this traction during saccadic eye movements. A traction from the vitreous humour could arise during aging, or after certain intraocular processes, which may lead to a liquefaction of the vitreous. This will result in the separation of the chamber into two regions, one with a liquefied vitreous and the other with the normal vitreous, due to the formation of membranes. The authors employed a rigid spherical container divided into two regions by an impermeable stretched elastic membrane, whose boundary is attached to the rigid wall. One region was occupied by the detached vitreous, modelled as an elastic viscous solid, the other was filled with a Newtonian fluid

to emulate the liquefied vitreous. This system was tested with saccadic eye movement, described by Repetto *et al.* (2005) [5]. After different configurations of the experimental set, obtained with a FEM solver (COMSOL Multiphysics), the results showed that the natural frequencies of oscillation of the membrane decrease significantly due to the presence of a Newtonian fluid. The oscillations of the stretched membrane were excited by rotations of the sphere with the frequencies of microsaccadic eye movements (amplitudes lower than 1° and frequencies ranging between 5 and 30 Hz). Moreover, the authors noticed how the maximum traction on the retina increases with the elastic parameter of the solid vitreous. Therefore the traction on the retina is more affected by the value of the viscosity of the solid phase and its peak corresponds to the acceleration phase of the motion. Eventually the normal and tangential traction at the attachment points increase with the rotation amplitude of saccade movement.

Chapter 3

Formulation of the problem

3.1 The model

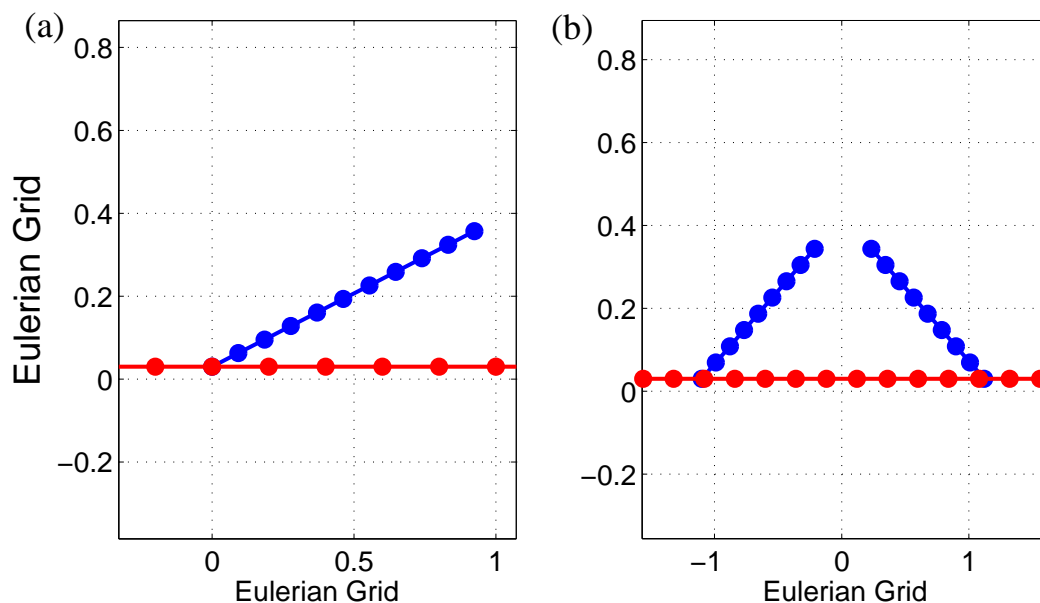


Figure 3.1: An example of the geometry used in two dimensions. Figure (a) represents a rigid plate with one filament, which simulates the retinal break. In Figure (b) two filaments are used for the retinal hole. In this case a fictitious spring, working only in traction, is added between them to create a connection which resembles the original case in three dimensions.

The aim of this thesis is to determine the detachment forces for two cases of retinal detachments: retinal tears and retinal holes. In order to evaluate these quantities a two dimensional model has been developed to simulate the movement of the detached retina. Based on the work made by Foster (2010) [7], we considered a transverse section of the detached retina and supposed that the part of the eye which is affected by the detachment is small with respect to the dimensions of the

whole eye globe such that the curvature of the eye could be neglected. For this reason the sclera and the attached part of the retina are approximated with a rigid horizontal plate while the detached retina is represented by a moving filament. We decided to clamp the filament on the plate in order to take into account the rigidity the detached retina should have in three dimensions. Eventually a certain relaxed position was defined at the beginning of the simulation. For the retinal tear only one filament has been used with a free moving end, while two filaments were used for the retinal hole. Since the two ends of the filaments represent the edges of an hole appearing within the detached layer of the retina, a fake spring was introduced between the two end points of the two filaments in order to simulate its inextensibility. The explained geometry is illustrated in Figure (3.1) where the red plate represents the moving section of the eye-wall considered and the blue filament is the detached retina. In Figure (3.1) the distance between the two filaments was chosen in a way that the fluid was allowed to move outside the simulated subretinal space. This structure was able to move according to the time law defined by Repetto (2005) [5], which is explained in the Chapter 2.

To represent the motion of the filaments inside a fluid we used the Immersed Boundary Method created by Peskin (2002) [11]. This is a numerical method which allows to simulate the movement of a (visco-)elastic incompressible material surrounded by a viscous fluid, in combination with another numerical method to describe the behavior of the filaments. To do so we used two different models, the first one was described by Newren *et al.* [12] where the filament was approximated as a certain number of Lagrangian points linked one another by springs, while the second one, introduced by Huang *et al.* [13], considers the filament as a beam and its motion is dictated by the d'Alembert formulation for an elastic string.

3.2 The Immersed Boundary Method

The immersed boundary method was introduced by Peskin (1972) [14] in order to study the flow around heart valves and in general to study the interaction between the fluid and a certain structure within it. It is based on a mathematical formulation and a numerical scheme. The mathematical formulation employs a mixture of Eulerian and Lagrangian variables, related with a Dirac delta function. In the numerical scheme the Eulerian variables are defined on a fixed Cartesian mesh, while the Lagrangian variables are defined on a curvilinear mesh which represent the material able to move inside the fluid. In order to analyze the problem a computational box is used as domain of the simulation. This box is defined by a stretched Eulerian grid, where its grid spacing is kept constant in the region where the movement takes place. Therefore the Eulerian grid is supplemented by a Lagrangian grid to define the moving object. The incompressible viscous Navier-Stokes equations are discretized on the Eulerian lattice while the filament equations are discretized on the moving Lagrangian points, which do not necessarily coincide with the fixed Eulerian mesh points of the fluid computation. The interaction between the filament and the fluid is handled by a smoothed approximation of the Dirac delta function.

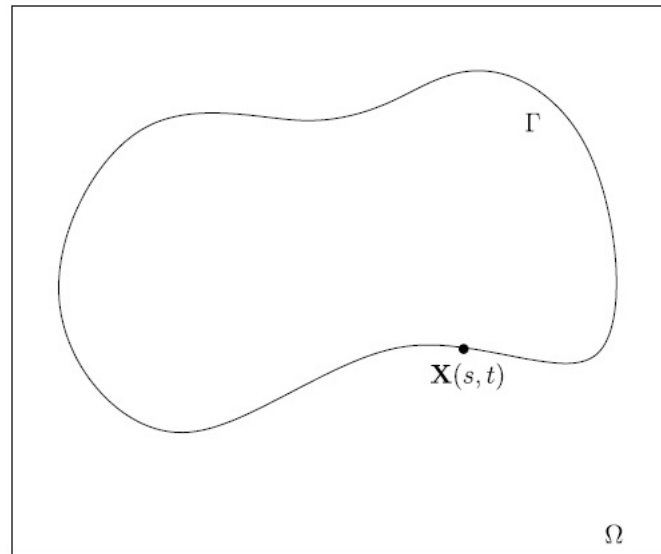


Figure 3.2: Example of a generic immersed body, defined by the domain Γ and the function $\mathbf{X}(s,t)$, immersed in a full-filled region Ω .

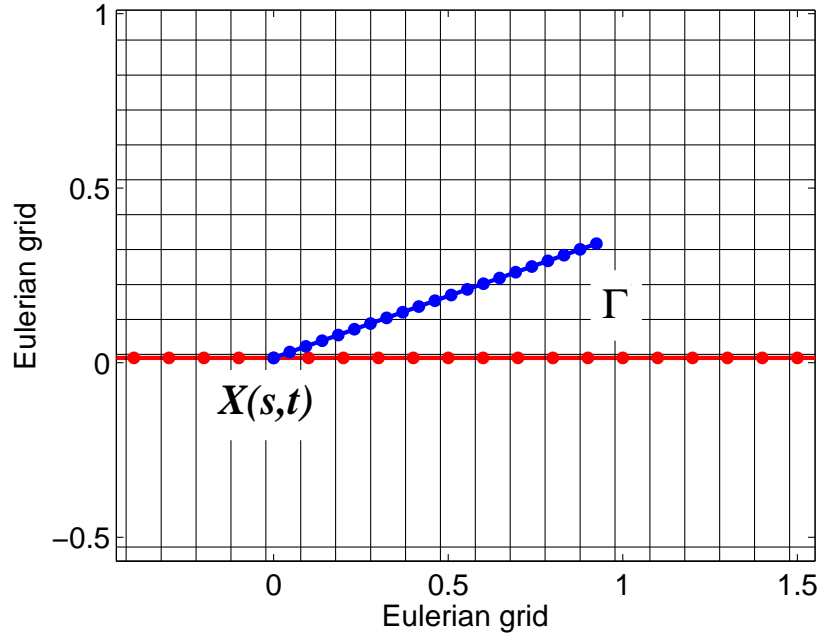


Figure 3.3: The immersed body used in this work, defined by the Lagrangian points $\mathbf{X}(s,t)$. The edges of the computational box Ω are placed at a certain distance from the domain Γ such that the boundaries won't affect the movement of the body. The black lines represent the Eulerian stretched grid.

Figure (3.2) illustrates a generic domain for the Immersed Boundary Method. The moving body is represented by the Lagrangian points $\mathbf{X}(s,t)$, which define the domain the object Γ , while the movement take place inside the region denominated Ω . In Figure (3.3) the geometry used in our work is shown, where the red line approximates the eye-wall while the blue line represents the detached part of the retina and the dots identify the Lagrangian points $\mathbf{X}(s,t)$, which define the domain Γ of the whole body. From this figure it could be noticed also how we defined the filament with twice the Lagrangian points of the plate. Moreover the Eulerian grid is shown. The mesh is defined by a specific grid spacing law, the distance of each Eulerian point is kept constant near the filament and in the region where the filament will move, while in the remaining areas the grid is stretched. Eventually the computational domain Ω is placed at a distance such that the flow at the border will not effect the movement of the body.

In our work we identified the Cartesian coordinates $\mathbf{x} = (x,y)$ and the time t as independent Eulerian variables, while the independent Lagrangian variables are the curvilinear material coordinate s and the time t . The dependent Eulerian variables are the velocity $\mathbf{u}(\mathbf{x},t)$, the pressure $p(\mathbf{x},t)$, the density $\rho(\mathbf{x},t)$, and the Eulerian force density $\mathbf{f}(\mathbf{x},t)$. The dependent Lagrangian variables are the position of filament $\mathbf{X}(s,t)$, the Lagrangian force density $\mathbf{F}(s,t)$, and the filament velocity $\mathbf{U}(s,t)$. The dimensionless governing equations are :

$$\frac{\partial \mathbf{u}}{\partial t}(\mathbf{x},t) + \mathbf{u}(\mathbf{x},t) \cdot \nabla \mathbf{u}(\mathbf{x},t) = -\nabla p(\mathbf{x},t) + \frac{1}{Re} \nabla^2 \mathbf{u}(\mathbf{x},t) + \mathbf{f}, \quad (3.1)$$

$$\nabla \cdot \mathbf{u} = 0, \quad (3.2)$$

$$\frac{\partial \mathbf{X}}{\partial t}(s,t) = \mathbf{U}(s,t), \quad (3.3)$$

$$\mathbf{f}(\mathbf{x},t) = \int_{\Gamma} \mathbf{F}(s,t) \delta(\mathbf{x} - \mathbf{X}(s,t)) ds, \quad (3.4)$$

$$\rho(\mathbf{x},t) = \rho_0, \quad (3.5)$$

$$\mathbf{U}(s,t) = \int_{\Omega} \mathbf{u}(\mathbf{x},t) \delta(\mathbf{x} - \mathbf{X}(s,t)) d\mathbf{x}, \quad (3.6)$$

Equation (3.1) is the Navier-Stokes equation, neglecting the gravity effect, considering the density of the fluid ρ_0 constant and with the incompressible assumption of the Equation (3.2). Equation (3.3) is related to the motion of the filament, with no-slip condition, where $\mathbf{U}(s,t)$ is the velocity of the filament. Eventually, the interaction between the Eulerian and Lagrangian grid is governed by a smoothed approximation of the two dimensional Dirac δ_h function. In this model, considering $\mathbf{x} = (x,y)$ and $r = \frac{\mathbf{x}}{\Delta h}$, the δ_h function used is :

$$\delta_h(r) = \begin{cases} \frac{1}{6\Delta h} \left[5 - 3\frac{|r|}{\Delta h} - \sqrt{-3\left(1 - \frac{|r|}{\Delta h}\right)^2 + 1} \right] & \text{for } 0.5\Delta h \leq |r| \leq 1.5\Delta h, \\ \frac{1}{3\Delta h} \left[1 + \sqrt{-3\left(\frac{r}{\Delta h}\right)^2 + 1} \right] & \text{for } |r| \leq 0.5\Delta h, \\ 0 & \text{otherwise,} \end{cases} \quad (3.7)$$

where Δh is the minimum grid spacing for the Eulerian grid.

The Equations (3.1) - (3.11) have been non-dimensionalized by introducing the following characteristic scales : the reference filament length L_f for length, the maximum velocity of a saccadic movement U_s , L_f/U_s for time, $\rho_0 U_s^2$ for pressure and $\rho_0 U_s^2 / L_f$ for the forcing component \mathbf{f} .

3.3 Filament Models

3.3.1 The method by Newren *et al.*

To evaluate the elastic force, we based our considerations on the study made by Newren *et al.* [12] and we referred to the work made by Zhu and Peskin [15] on a flapping filament inside a flowing soap film to define the bending force of the filament. The entities we used are the following :

$$\mathbf{F} = \mathbf{F}_s(s, t) + \mathbf{F}_b(s, t) = \frac{\partial \mathbf{T} \hat{\boldsymbol{\tau}}}{\partial s} - \frac{\partial E_b}{\partial \mathbf{X}}, \quad (3.8)$$

$$T = K_s \left(\left| \frac{\partial \mathbf{X}}{\partial s} \right| - 1 \right), \quad (3.9)$$

$$\hat{\boldsymbol{\tau}} = \frac{\frac{\partial \mathbf{X}}{\partial s}}{\left| \frac{\partial \mathbf{X}}{\partial s} \right|}, \quad (3.10)$$

$$E_b = \frac{1}{2} K_b \int \left| \frac{\partial^2 \mathbf{X}}{\partial s^2} \right|^2 ds. \quad (3.11)$$

The Lagrangian force density $\mathbf{F}(s, t)$ consists on two terms: the stretching and compression force $\mathbf{F}_s(s, t)$, and the bending force $\mathbf{F}_b(s, t)$. The stretching force represents the opposition the filament offers at the action of elongation, in our simulations the maximum elongation performed by the filament was around 1%. To compute its value the tension T of the filament is used, applying the Hook's law, where $\hat{\boldsymbol{\tau}}$ is the unit tangent vector defined at each point of the filament. As the stretching force, the bending force is the resistance of filament at the action of changing its curvature and it is obtained by taking the Frechet derivative of the bending energy E_b , which is defined by Eq. (3.11). Both the stretching force and the bending force are defined by using a stiffness parameter: K_s is the filament stretching coefficient which is chosen in such a way the filament has almost no stretch; while K_b is the bending

rigidity computed using the physiological parameters of the eye. These parameters are made dimensionless, following the same notation as the previous section, with $\rho_0 U_s^2 L_f$ for the stretching stiffness K_s and $\rho_0 U_s^2 L_f^3$ for the bending stiffness K_b .

3.3.2 The method by Huang *et al.*

In the work by Huang *et al.* [13] the governing equations of the filaments are based on the d'Alembert formulation for an elastic string, which can be written in a Lagrangian form as follows :

$$\rho_1 \frac{\partial^2 \mathbf{X}}{\partial t^2} = \frac{\partial}{\partial s} \left(T \frac{\partial \mathbf{X}}{\partial s} \right) - \frac{\partial^2}{\partial s^2} \left(K_b \frac{\partial^2 \mathbf{X}}{\partial s^2} \right) + \rho_1 \mathbf{g} - \mathbf{F}, \quad (3.12)$$

where s is the arclength, T is the tension force along the filament as the previous case, K_b is the bending stiffness, \mathbf{F} is the Lagrangian force exerted on the filament by the surrounding fluid, the term $-\frac{\partial^2}{\partial s^2} \left(K_b \frac{\partial^2 \mathbf{X}}{\partial s^2} \right)$ corresponds to the bending force \mathbf{F}_b and ρ_1 denotes the density difference between the filament and the fluid. Defining the density of the fluid as ρ_0 and the density of the filament as ρ_f , ρ_1 is equal to $\rho_f - \rho_0 A$, where A is the sectional area of the filament. Nevertheless we decided to consider a filament with the same density of the surrounding fluid and to avoid the action of the gravity, this allows us to simplify the Equation (3.12) as follow:

$$\mathbf{F} = \frac{\partial}{\partial s} \left(T \frac{\partial \mathbf{X}}{\partial s} \right) + \mathbf{F}_b. \quad (3.13)$$

This equation is coupled with the inextensibility condition, expressed by:

$$\frac{\partial \mathbf{X}}{\partial s} \cdot \frac{\partial \mathbf{X}}{\partial s} = 1. \quad (3.14)$$

From Equation (3.13) and Equation (3.14) the tension T is determined, which leads to the Poisson equation:

$$\frac{\partial \mathbf{X}}{\partial s} \cdot \frac{\partial^2}{\partial s^2} \left(T \frac{\partial \mathbf{X}}{\partial s} \right) = - \frac{\partial \mathbf{X}}{\partial s} \cdot \frac{\partial}{\partial s} (\mathbf{F}_b - \mathbf{F}). \quad (3.15)$$

Since Eq. (3.4) has to be valid also in this method, the scale chosen for the non-dimensionalization of the Lagrangian force \mathbf{F} is $\rho_0 U_s^2 L_f$ and consequentially the scale for the bending stiffness is $\rho_0 U_s^2 L_f^3$ and $\rho_0 U_s^2 L_f$ for the tension T .

3.4 Boundary conditions

Since the domain has to be finite, in order to execute our simulations, boundary conditions are needed. There are different types of boundary conditions that could be used, in this project Dirichlet and Neumann boundary conditions have been applied along with periodic boundary conditions. Moreover, additional conditions have to be chosen for the attached point and the free end of the filament, in order to define its behavior.

3.4.1 The method by Newren *et al.*

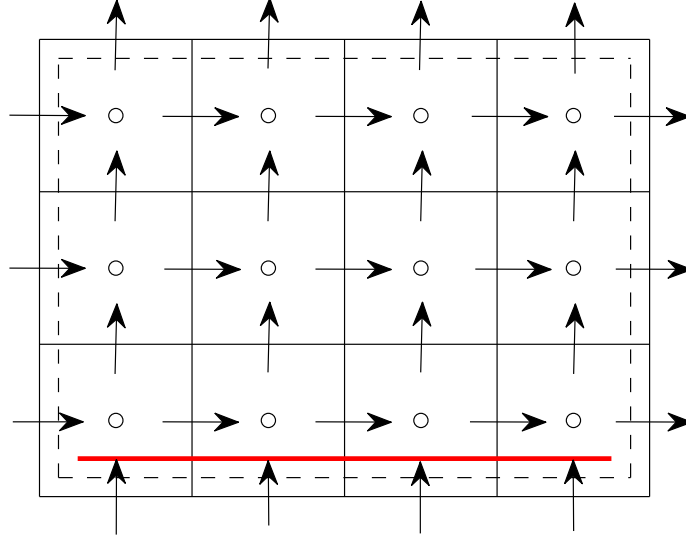


Figure 3.4: Dirichlet and Neumann boundary conditions: the velocity and its derivative at the edges of the box are equal to zero; the dashed line is the computational domain while the red line is the plate.

With the solution proposed by Newren *et al.* we decided to apply Dirichlet and Neumann homogeneous boundary conditions at the edges of the computational domain, which means the velocity and its derivative are equal to zero along those regions. In specific, considering the velocity vector of the fluid as $\mathbf{u}(u, v)$, the boundary conditions can be written as follow for the horizontal borders :

$$v|_{\Omega_b} = v|_{\Omega_u} = 0 \quad \& \quad \left. \frac{du}{dy} \right|_{\Omega_b} = \left. \frac{du}{dy} \right|_{\Omega_u} = 0, \quad (3.16)$$

where Ω_b is the bottom side of the box and Ω_u is the upper side; while for the vertical borders:

$$u|_{\Omega_l} = u|_{\Omega_r} = 0 \quad \& \quad \left. \frac{dv}{dx} \right|_{\Omega_l} = \left. \frac{dv}{dx} \right|_{\Omega_r} = 0, \quad (3.17)$$

where Ω_l is the left side and Ω_r is the right side.

As shown in Figure (3.2), these specific conditions imply no inflow or outflow through the boundaries of the domain. For this reason the distance between the box and the filament must not be too small, otherwise the boundary conditions will interfere with the flow around the body.

Regarding the conditions for the filament, we imposed no constrictions at the free end while at the attached point we considered the clamped condition, which is implemented by choosing a percentage of the filament that will be maintained fixed during the whole simulation and the angle between the plate and the filament. To do so, we overlapped a certain number of Lagrangian points of the plate with the Lagrangian points of the filament defined by the same coordinates. In Figure (3.5) there is an example of the boundary condition used to clamp the filament. In this specific case we fixed the 2% of the filament length adding two supplementary Lagrangian points at the plate.

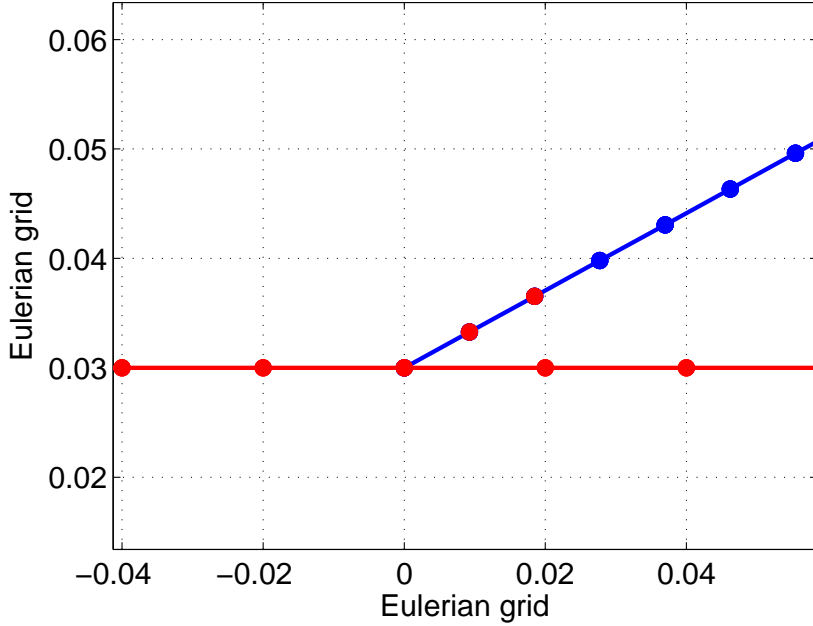


Figure 3.5: Clamped condition at the fixed end of the filament. The red dots represents the Lagrangian points of the plate, while the blue dots are the Lagrangian points of the filament.

3.4.2 The method by Huang *et al.*

To apply the method by Huang *et. al* we took into account periodic boundary conditions along with the Dirichlet and Neumann conditions. As shown in Figure (3.6) the computational domain, shown with the dashed line, corresponds to the whole grid without the last column. In these regions the velocities are known and are equal to the values in the first column which means that the structure inside the domain is repeated infinite times on the left and right sides of the box. This condition can be written as follow :

$$\mathbf{u}|_{\Omega_l} = \mathbf{u}|_{\Omega_r} , \quad (3.18)$$

where Ω_l and Ω_r are the left and right margins of the domain. For this reason the dimensions of the computational box has to be chosen such that the phenomena

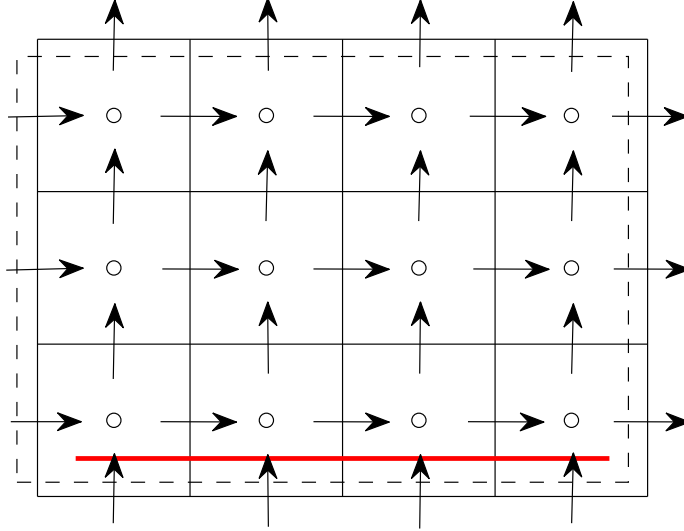


Figure 3.6: Periodic boundary conditions: the velocity .

which take place at the border won't effect the movement of the object.

As the previous case Dirichlet and Neumann boundary conditions are taken in account, the velocities and their derivatives are equal to zero only through Ω_b and Ω_u . They have the same expression of the one enunciated in Equation (3.17).

The periodic conditions are taken into account along with the Dirichlet and Neumann boundary conditions but in this case the velocities and their derivatives are equal to zero only through the horizontal borders of the computational box. Their formulation is equal to the one expressed in Equation (3.17).

Also in this case the filament is considered clamped at the plate and to satisfy this condition the attachment point and the derivative with respect to the arclength are fixed.

$$\mathbf{X}|_{s=0} = \mathbf{X}_0 \quad \& \quad \left. \frac{\partial \mathbf{X}}{\partial s} \right|_{s=0} = (\cos\theta, \sin\theta), \quad (3.19)$$

where θ is the angle between the plate and the filament. The free end is able to move without any restriction, which means the following conditions have to be verified

$$T|_{s=l} = 0, \quad \left. \frac{\partial^2 \mathbf{X}}{\partial s^2} \right|_{s=l} = (0, 0), \quad \left. \frac{\partial^3 \mathbf{X}}{\partial s^3} \right|_{s=l} = (0, 0), \quad (3.20)$$

Eventually the interaction force between the fluid and the Immersed Boundary

has to be taken in account.

$$\mathbf{F} = \alpha \int_0^t (\mathbf{U} - \mathbf{U}_{fil}) dt' + \beta (\mathbf{U} - \mathbf{U}_{fil}), \quad (3.21)$$

where α and β are large negative free constants, \mathbf{U} is the fluid velocity obtained by interpolation at the IB, defined by Equation (3.6) and \mathbf{U}_{fil} is the velocity of the filament expressed as $\mathbf{U}_{fil} = d\mathbf{X}/dt$. The Equation (3.21) implies that the adjacent fluid points are linked with the IB by a set of identical stiff springs with damping.

3.5 Time and spatial discretization

In order to solve the flow equations a discretization in time and space is needed. Time is represented by N discrete points with a step size of $\Delta t = \frac{T}{N}$. Denoting $\mathbf{u}^n(\mathbf{x})$ the approximation of the actual velocity vector $\mathbf{u}(\mathbf{x}, n\Delta t)$ at time $n\Delta t$, similarly $\mathbf{X}^n(s)$ and p^n respectively stand for $\mathbf{X}(s, n\Delta t)$ and $p(\mathbf{x}, n\Delta t)$; while spatial discretization is obtained using a cell-centered Cartesian grid for the Eulerian variables, and one more discrete Lagrangian grid for the IB variables. The filament is defined by K discrete points with a step size of $\Delta s = \frac{L}{K}$, where L is the length of the filament. From now on the values $n = 0, 1, 2, \dots, N$ and $k = 0, 1, 2, \dots, K$ are used to identify then-th time step and the k -th spatial step.

3.5.1 Navier-Stokes equation

The time discretization of the Navier-Stokes equation has been handled using an explicit second-order Adams-Bashfort scheme for the non linear convective terms and an implicit Crank-Nicholson scheme for the diffusive terms. Therefore the Equation (3.1) and (3.2) can be written as:

$$\begin{cases} \frac{(\mathbf{u}^{n+1} - \mathbf{u}^n)}{\Delta t} + \left[\frac{3}{2}N(\mathbf{u}^n) - \frac{1}{2}N(\mathbf{u}^{n-1}) \right] = -G(p^{n+1}) + \frac{L(\mathbf{u}^{n+1}) + L(\mathbf{u}^n)}{2Re} + bc_1 \\ D(\mathbf{u}^n) = bc_2 \end{cases} \quad (3.22)$$

Where G, D, L and N are the discrete values of the following operators:

$$\begin{aligned} \nabla p &\Rightarrow G(p) \\ \nabla \cdot \mathbf{u} &\Rightarrow D(\mathbf{u}) - bc_1 \\ \nabla^2 \mathbf{u} &\Rightarrow L(\mathbf{u}) + bc_2 Re \\ \nabla \cdot (\mathbf{u}\mathbf{u}) &\Rightarrow N(\mathbf{u}) \end{aligned} \quad (3.23)$$

Grouping the terms with \mathbf{u}^{n+1} on the left side of the equation:

$$\begin{cases} \frac{\mathbf{u}^{n+1}}{\Delta t} - \frac{L(\mathbf{u}^{n+1})}{2Re} + G(p^{n+1}) = \frac{\mathbf{u}^n}{\Delta t} - \left[\frac{3}{2}N(\mathbf{u}^n) - \frac{1}{2}N(\mathbf{u}^{n-1}) \right] + \frac{L(\mathbf{u}^n)}{2Re} + bc_1 \\ D(\mathbf{u}^n) = bc_2 \end{cases} \quad (3.24)$$

Introducing the following definitions

$$\begin{aligned} A &= \frac{1}{\Delta t} - \frac{L}{Re}; \\ \mathbf{r}^n &= \frac{\mathbf{u}^n}{\Delta t} - \left[\frac{3}{2}N(\mathbf{u}^n) - \frac{1}{2}N(\mathbf{u}^{n-1}) \right] + \frac{L(\mathbf{u}^n)}{2 Re}, \end{aligned} \quad (3.25)$$

the system become:

$$\begin{cases} A(\mathbf{u}^{n+1}) + G(p^{n+1}) = \mathbf{r}^n + bc_1 \\ D(\mathbf{u}^n) = bc_2 \end{cases} \quad (3.26)$$

Applying a spatial discretization, the system (3.26) could be written as an algebraic linear system:

$$\begin{bmatrix} A & G \\ D & 0 \end{bmatrix} \begin{bmatrix} \mathbf{u}^{n+1} \\ p^{n+1} \end{bmatrix} = \begin{bmatrix} \mathbf{r}^{n+1} \\ 0 \end{bmatrix} + \begin{bmatrix} bc_1 \\ bc_2 \end{bmatrix} \quad (3.27)$$

An approximation of this linear system has been introduced by Perot [16]:

$$\begin{bmatrix} A & 0 \\ D & -(\Delta t D)G \end{bmatrix} \begin{bmatrix} I & (\Delta t)G \\ 0 & I \end{bmatrix} \begin{bmatrix} \mathbf{u}^{n+1} \\ p^{n+1} \end{bmatrix} = \begin{bmatrix} \mathbf{r}^{n+1} \\ 0 \end{bmatrix} + \begin{bmatrix} bc_1 \\ bc_2 \end{bmatrix} \quad (3.28)$$

This approximation introduce a small error given by:

$$\left(\frac{\Delta t}{2 Re} \right) L G p^{n+1}, \quad (3.29)$$

since $(\Delta t A)G = (I - \frac{\Delta t L}{2 Re})G \cong G$.

To solve the system (3.28) the LU decomposition is introduced such that the large indefinite system is split into two smaller problems

$$\begin{bmatrix} A & 0 \\ D & -(\Delta t D)G \end{bmatrix} \begin{bmatrix} \mathbf{u}^* \\ p^{n+1} \end{bmatrix} = \begin{bmatrix} \mathbf{r}^{n+1} \\ 0 \end{bmatrix} + \begin{bmatrix} bc_1 \\ bc_2 \end{bmatrix} \quad (3.30)$$

$$\begin{bmatrix} I & (\Delta t)G \\ 0 & I \end{bmatrix} \begin{bmatrix} \mathbf{u}^{n+1} \\ p^{n+1} \end{bmatrix} = \begin{bmatrix} \mathbf{u}^* \\ p^{n+1} \end{bmatrix} \quad (3.31)$$

Where \mathbf{u}^* is an intermediate variable which is defined either by Eq. (3.30) or Eq. (3.31). This system can also be written in this way:

$$\begin{aligned} A \mathbf{u}^* &= \mathbf{r}^n + bc_1 \\ \Delta t D G p^{n+1} &= D \mathbf{u}^* - bc_2 \\ \mathbf{u}^{n+1} &= \mathbf{u}^* - \Delta t G p^{n+1} \end{aligned} \quad (3.32)$$

3.5.2 Eulerian force density and filament velocity

The integral relations of the Eq. (3.4) and Eq. (3.6) can be discretized by :

$$\mathbf{f}^n(\mathbf{x}) = \sum_k \mathbf{F}^n(s) \delta_h(\mathbf{x} - \mathbf{X}^n(s)) \Delta s, \quad (3.33)$$

$$\mathbf{U}^{n+1}(s) = \sum_{\mathbf{x}} \mathbf{u}^{n+1}(\mathbf{x}) \delta_h(\mathbf{x} - \mathbf{X}^n(s)) h^2, \quad (3.34)$$

where the notation \sum_k means the sum over all the discrete points of the form $s = k\Delta s$. The notation $\sum_{\mathbf{x}}$ means the sum over all the discrete points of the form $\mathbf{x} = (ih, jh)$, where i and j are integers and h is the grid spacing of the grid.

3.5.3 Filament motion equation

With $\mathbf{U}^{n+1}(s)$ known, the filament motion equation (3.3) is discretized as follows:

$$\frac{\mathbf{X}^{n+1}(s) - \mathbf{X}^n(s)}{\Delta t} = \mathbf{U}^{n+1}(s). \quad (3.35)$$

3.5.4 The method by Newren *et al.*

Lagrangian stretching and compression force

Representing the filament by a discrete number of points, $s = k\Delta s$, where k is an integer, the filament tension and unit tangent are defined at the ‘‘half-integer’’ points given by $s = (k + 1/2)\Delta s$. For any function $\phi(s)$ we define the discrete approximation of the first order derivative of the arclength as :

$$(D_s \phi)(s) = \frac{\phi\left(s + \frac{\Delta s}{2}\right) - \phi\left(s - \frac{\Delta s}{2}\right)}{\Delta s}, \quad (3.36)$$

$$(D_s^+ \phi)(s) = \frac{\phi(s + \Delta s) - \phi(s)}{\Delta s},$$

$$(D_s^- \phi)(s) = \frac{\phi(s) - \phi(s - \Delta s)}{\Delta s}.$$

(3.37)

Then the equations (3.9) and (3.10) can be discretized as :

$$T^n = K_s (|D_s \mathbf{X}^n| - 1), \quad (3.38)$$

$$\hat{\boldsymbol{\tau}}^n = \frac{D_s \mathbf{X}^n}{|D_s \mathbf{X}^n|}, \quad (3.39)$$

As demonstrated by Newren *et al.* [12], the stretching force \mathbf{F}_s , showed in the Equation (3.8), is discretized by writing the force at an immersed boundary point

as a difference in the tensions on either side of that point. Assuming a single closed boundary with no external links, this can be written as:

$$(\mathbf{F}_s)_k = \frac{(T_{k+1/2}(t)\hat{\boldsymbol{\tau}}_{k+1/2}(t)) - (T_{k-1/2}(t)\hat{\boldsymbol{\tau}}_{k-1/2}(t))}{\Delta s} \quad (3.40)$$

$$(\mathbf{F}_s)_k = \frac{\left(\frac{K_s}{\Delta s} (\|\mathbf{X}_{k+1}(t) - \mathbf{X}_k(t)\| - \ell_0) \frac{\mathbf{X}_{k+1}(t) - \mathbf{X}_k(t)}{\|\mathbf{X}_{k+1}(t) - \mathbf{X}_k(t)\|} \right)}{\Delta s} - \frac{\left(\frac{K_s}{\Delta s} (\|\mathbf{X}_{k-1}(t) - \mathbf{X}_k(t)\| - \ell_0) \frac{\mathbf{X}_{k-1}(t) - \mathbf{X}_k(t)}{\|\mathbf{X}_{k-1}(t) - \mathbf{X}_k(t)\|} \right)}{\Delta s}, \quad (3.41)$$

where the expression $(\mathbf{F}_s)_k$ denotes the value of the Lagrangian variable \mathbf{F}_s at the k -th gridpoint, while ℓ_0 is the resting length of the ‘‘springs’’ connecting the immersed boundary points.

The reason for calling the connection between IB points a ‘‘spring’’ because in the Equation (3.41) $K_s/\Delta s$ serves as a spring constant, $\|\mathbf{X}_i - \mathbf{X}_k\| - \ell_0$ is the length by which the connection between the point i and k has been stretched and $(\mathbf{X}_i(t) - \mathbf{X}_k(t))/\|\mathbf{X}_i(t) - \mathbf{X}_k(t)\|$ is the unit vector in the direction of the connection. This equation can be written considering S_k as the set of IB points which are connected to the k -th IB point:

$$(\mathbf{F}_s)_k = \sum_{i \in S_k} \frac{K_s}{\Delta s} (\|\mathbf{X}_i(t) - \mathbf{X}_k(t)\| - \ell_0) \frac{1}{\Delta s} \frac{\mathbf{X}_i(t) - \mathbf{X}_k(t)}{\|\mathbf{X}_i(t) - \mathbf{X}_k(t)\|}. \quad (3.42)$$

Lagrangian bending force

The bending energy Eq. (3.11) and the corresponding bending force \mathbf{F}_b in the Eq. (3.8) are discretized in this way [15]:

$$E_b = \frac{1}{2} K_b \sum_i |D_s D_s \mathbf{X}|^2 \Delta s = \frac{1}{2} K_b \sum_{i=2}^{n_f-1} \left[\frac{|\mathbf{X}_{i+1} + \mathbf{X}_{i-1} - 2\mathbf{X}_i|^2}{(\Delta s)^4} \right] \Delta s, \quad (3.43)$$

$$(\mathbf{F}_b)_k = \frac{K_b}{(\Delta s)^4} \sum_{i=2}^{n_f-1} (\mathbf{X}_{i+1} + \mathbf{X}_{i-1} - 2\mathbf{X}_i) (2\delta_{ik} - \delta_{i+1,k} - \delta_{i-1,k}), \quad (3.44)$$

employing the same notation used for the stretching force, $(\mathbf{F}_b)_k$ is the bending force at the k -th gridpoint, while n_f is the total number grid points of the filament and δ_{ik} is the Kronecker symbol whose definition is:

$$\delta_{ik} = \begin{cases} 1, & \text{if } i = k, \\ 0, & \text{if } i \neq k. \end{cases} \quad (3.45)$$

3.5.5 The method by Huang *et al.*

As for the previous case, the tension force is defined on the interfaces of the grid while the other variables are evaluated on the nodes. Using the same notation of Equation (3.36), D_s , D_{ss} and D_{sss} denote the difference approximation to the first, second and third order derivatives of the arclength s . Thus, the second order central difference approximation is expressed as:

$$D_s^+ D_s^- \phi = \frac{\phi(s + \Delta s) - 2\phi(s) + \phi(s - \Delta s)}{\Delta s^2}, \quad (3.46)$$

the same rules are applied for the time t .

Governing equation of the filament

Considering now the d'Alembert equation of the filament, illustrated by (3.13), it has been discretized with:

$$\mathbf{F}_k^n = [D_s(T^{n+1/2} D_s \mathbf{X}^{n+1})]_k + (\mathbf{F}_b^*)_k, \quad (3.47)$$

where $\mathbf{X}^* = 2\mathbf{X}^n - \mathbf{X}^{n-1}$ is called the predicted position of the filament

$$\mathbf{F}_b^* = \mathbf{F}_b(2\mathbf{X}^n - \mathbf{X}^{n-1}) \quad (3.48)$$

Tension and bending force

The tension term appearing in the Equation (3.13) is discretized in this way:

$$[D_s(T D_s \mathbf{X})]_k = \frac{T_{k+1/2}(D_s \mathbf{X})_{k+1/2} - T_{k-1/2}(D_s \mathbf{X})_{k-1/2}}{\Delta s}. \quad (3.49)$$

While the discrete bending force results in:

$$(\mathbf{F}_b)_k = - [D_s^+ D_s^- (K_b D_{ss} \mathbf{X})]_k = -K_b \frac{(D_{ss} \mathbf{X})_{k+1} - 2(D_{ss} \mathbf{X})_k + (D_{ss} \mathbf{X})_{k-1}}{\Delta s^2}, \quad (3.50)$$

where

$$(D_{ss} \mathbf{X})_k = \begin{cases} \mathbf{0}, & \text{if } k = 0, \\ (D_s^+ D_s^- \mathbf{X})_k, & \text{if } k = 1, 2, \dots, K-1. \end{cases} \quad (3.51)$$

Again using the knowledge obtained by Equation (3.47) along with the inextensibility condition $(D_s \mathbf{X} \cdot D_s \mathbf{X})^{n+1} = 1$ the Poisson equation can be written as

$$(D_s \mathbf{X}^*)_{k+1/2} \cdot [D_s(D_s(T^{n+1/2} D_s \mathbf{X}^*))]_{k+1/2} = -(D_s \mathbf{X}^*)_{k+1/2} \cdot [D_s(\mathbf{F}_b - \mathbf{F}^n)]_{k+1/2}, \quad (3.52)$$

Boundary

The conditions imposed at the fixed end, introduced in Equation (3.19) are discretized as follow:

$$(D_{ss}\mathbf{X})_N = \frac{(\cos\theta, \sin\theta) - (D_s\mathbf{X})_{N-1/2}}{0.5\Delta s}. \quad (3.53)$$

Eventually the interaction force term appearing in Equations (3.52) and (3.47) is treated in this way:

$$\mathbf{F}_k^n = \alpha \sum_j^n (\mathbf{U}_k^j - (\mathbf{U}_{fil})_k^j) dt' + \beta (\mathbf{U}_k^j - (\mathbf{U}_{fil})_k^j), \quad (3.54)$$

where \mathbf{U}_k^j is the velocity of the filament, expressed by Equation (3.34) at time j for the Lagrangian point k .

3.6 The staggered grid

At first sight one could think it would be a good idea to apply, on a regular collocated grid, a centered finite difference method to the spacial operator, in order to solve the Navier-Stokes equations. Figure (3.7) illustrates an example of a regular collocated grid, where the black dots indicate the points where the pressure is computed and the arrows correspond to the horizontal and vertical velocity. As shown, both of them are evaluated in the middle of each mesh, which implies the pressure and the velocity components will be unknown at the corners. Writing a discretization in a uniform 2D grid for the difference operators of the velocity and pressure:

$$\begin{aligned} \left[\frac{\partial p}{\partial x} \right]_{i,j}^{n+1} &\approx -\frac{p_{i+1,j}^{n+1} - p_{i-1,j}^{n+1}}{2\Delta x} \\ \left[\frac{\partial^2 u}{\partial y^2} \right]_{i,j}^n &\approx \frac{u_{i,j-1}^n - 2u_{i,j}^n + u_{i,j+1}^n}{\Delta y^2}, \end{aligned} \quad (3.55)$$

where Δx and Δy are uniform spatial cell sizes, $p_{i,j}^n$ and $u_{i,j}^n$ are the numerical value of pressure and velocity at the point with spacial index (i,j) at time level n . Nevertheless two types of instabilities will arise with this kind of discretization. Even if the velocities may be well approximated, the pressure can be highly oscillatory or even undetermined. The reason for this phenomenon is that the symmetric difference operators in the Eq.(3.55) will nullify the checkerboard pressures. In fact, considering the hole grid, the pressure computed in the center of a certain mesh won't be related to the pressures of adjacent cells. Hence, the pressure is undetermined by the discrete system and wild oscillations or overflow will occur. The second type of instability is visible as non-physical oscillations in the velocities at high Reynolds number.

For these reasons it is better to use a staggered grid instead of a collocated grid, as the work of Langtangen *et al.* has shown [17]. In this case, as shown in Figure

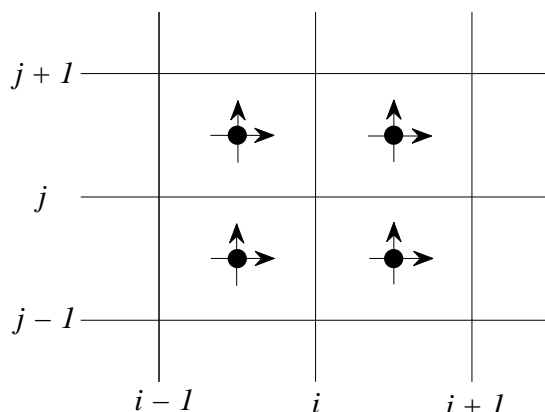


Figure 3.7: Collocated grid. The horizontal and vertical velocities are computed in the middle of each mesh with \rightarrow and \uparrow respectively, as for the pressures at each \bullet .

(3.8), the horizontal and vertical components of the velocities are computed at the borders of each mesh, while the pressure is evaluated at the centers of each cell, as the previous case. Figure (3.9) represents.

Referring to a certain point on the staggered grid, for instance defined by spacial indices $(i, j + \frac{1}{2})$ like in Figure (3.9), the discretized terms $-\partial p / \partial x$ and $\partial^2 u / \partial y^2$ now results in:

$$\begin{aligned} \left[\frac{\partial p}{\partial x} \right]_{i, j + \frac{1}{2}}^{n+1} &\approx -\frac{p_{i+\frac{1}{2}, j + \frac{1}{2}}^{n+1} - p_{i-\frac{1}{2}, j + \frac{1}{2}}^{n+1}}{2\Delta x} \\ \left[\frac{\partial^2 u}{\partial y^2} \right]_{i, j + \frac{1}{2}}^n &\approx \frac{u_{i, j - \frac{1}{2}}^n - 2u_{i, j + \frac{1}{2}}^n + u_{i, j + \frac{3}{2}}^n}{\Delta y^2}. \end{aligned} \quad (3.56)$$

The staggered grid is convenient for many of the derivatives appearing in the equations, like linear terms, but the nonlinear terms require an operation of averaging.

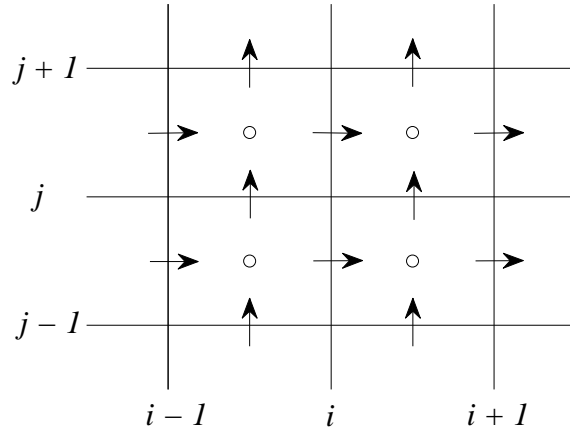


Figure 3.8: Staggered grid. The horizontal and vertical velocities are delineated with \rightarrow and \uparrow respectively at the edges of each mesh, while the pressures are computed in every \circ at each center.

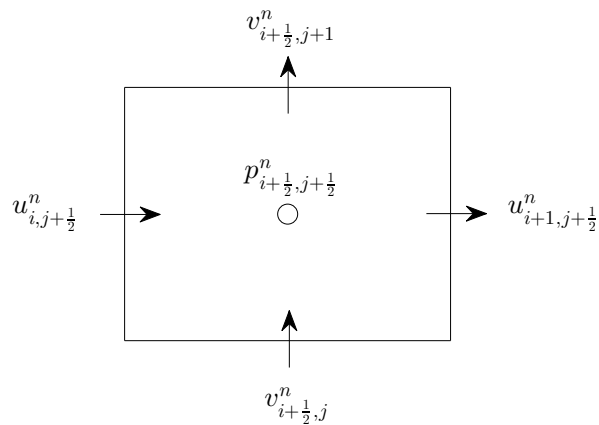


Figure 3.9: A cell of the staggered grid.

Chapter 4

Simulations and results

4.1 Numerical Implementation

The mathematical formulation of our problem, explained in the previous chapter, has been implemented in *MATLAB*[®] environment by Bagheri at the Linné Flow Centre in the 2012. This code was used by Bagheri, Mazzino and Bottaro [18] to demonstrate how a single filament, hinged on a bluff body, could generate a spontaneous symmetry breaking resulting in a net lift force. In their work they handled the implementation of the Immersed Boundary method and the filament model made by Newren *et al.*, while at the University of Genoa Natali [19] developed the code for the filament model introduced by Huang *et al.*

The first step we had to take in account was related to the dimensions of the computational box and the fineness of its meshes throughout convergence studies. The two distinct boundary conditions considered led to different values for the computational domain, while the grid fineness chosen for one case was maintained also for the other case. Once we established the dimensions of our domain and the grid spacing, we prepared a set of simulation in order to reproduce the movement of the detached retina and to confront retinal tears with retinal holes. The aim of this work is to define which case of retinal detachment generates highest values of stresses, in terms of forces and torques on the remaining attached retina, leading to a further detachment.

4.1.1 Grid convergence

With the purpose of determining a proper minimum grid spacing we evaluated a convergence test using the Stokes' second problem. It consists of an oscillating plate in a viscous incompressible fluid. By positioning the plate at the height $y = 0$ and imposing an oscillatory movement along the x plane which is dictated by the time law $U_{plate} = U \cos(\omega t)$, where U is a constant, ω is the oscillatory frequency and t is the time, the flow over the plate is governed by the following equation :

$$u(y, t) = U e^{-\frac{y}{k}} \cos\left(\frac{y}{k} - \omega t\right) \quad (4.1)$$

In the expression above $u(y, t)$ is the velocity of the fluid over the plate and k is

the boundary layer thickness which is equal to $\sqrt{\frac{2\nu}{\omega}}$.

Fixed a certain dimension for the computational box, we had executed different simulations with different grid spacing searching for a convergence of the grid. A rigid plate, with a thickness equal to the minimum grid spacing, has been implemented and it was allowed to move inside the computational box following the time law $U_{plate} = U\cos(\omega t)$. We compared the velocity of the fluid obtained by the code with the analytical solution of the Stokes' second problem, showed in Equation (4.1). On Figure (4.1) and Figure (4.2) the mean value of the absolute error between the analytical and numerical solutions is pointed out.

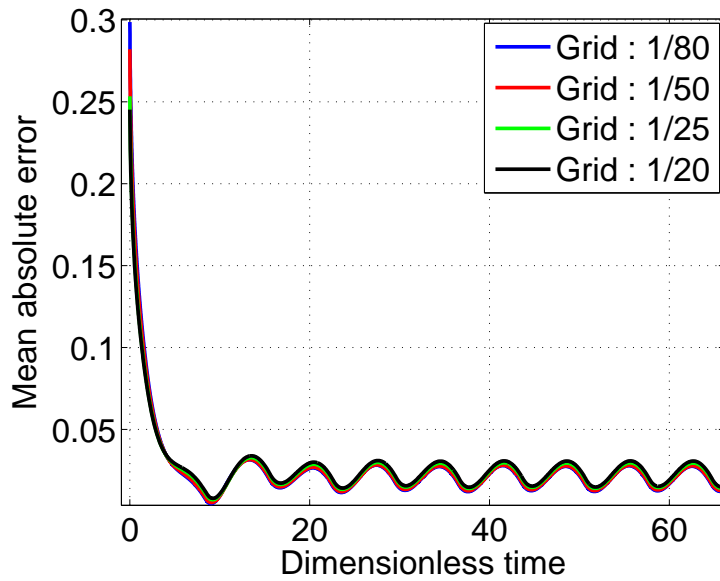


Figure 4.1: Mean absolute error of the numerical solution of the second Stokes' problem for different minimum grid spacing.

It could be noticed how the mean absolute error decreases with the minimum grid spacing and its value has the order of 10^{-2} . Since the difference between the results obtained with a grid spacing of 1/50 and 1/80 has the order of 10^{-3} , we decided to use the value 1/50 in order to reduce the execution time of the simulation.

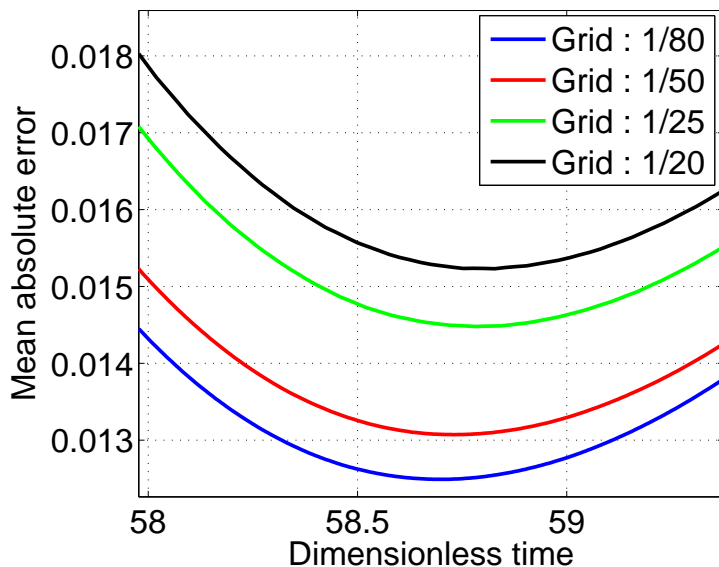


Figure 4.2: Magnification of the mean absolute error showed in Figure (4.1).

4.1.2 Defining the computational domain

Since we used Dirichlet and Neumann boundary conditions for Newren's *et al.* model and a combination of Dirichlet and periodic boundary conditions for Huang's *et al.* model, two different computational domains are used, which means two convergence studies are needed. In the first case the plate, used to simulate the wall of the eye-globe, is smaller than the computational box, while in the second case the length of the plate has the same value of the domain width. Since for the Dirichlet and Neumann conditions no inflow or outflow is allowed through the borders, the plate and the box cannot have the same length; while for the periodic conditions there is no issue having the same length thanks to Equation (3.18).

The method by Newren *et al.*

For this model we used a staggered grid with a constant grid spacing in the region of the domain where the plate will move, while the remaining space is defined by a stretched grid. During the convergence test we used a plate with only one filament clamped and chose temporary parameters for the filament and the grid spacing in order to define a plausible box.

In Figure (4.3) and Figure (4.4) we presents the results of our simulations for different sizes of the computational box. Using the same notation of the previous chapter, in particular referring to Figure (3.2), the computational domain Ω is defined by the vectors $A_x : [x_{min}, x_{max}]$, which is the range of values of x , and $A_y : [y_{min}, y_{max}]$, which is the range of values of y , such that $\Omega = A_x \cap A_y$. Inside Ω a smaller box, $\tilde{\Omega}$, has been adopted, containing only the region with a constant grid spacing. It is defined by $B_x : [x_1, x_2]$, the vector containing the range values of x , and $B_y : [y_1, y_2]$, the vector containing the range values of y , such that $\tilde{\Omega} = B_x \cap B_y$, where $x_1 > x_{min}$, $x_2 < x_{max}$, $y_1 > y_{min}$ and $y_2 < y_{max}$. The dimensions of the

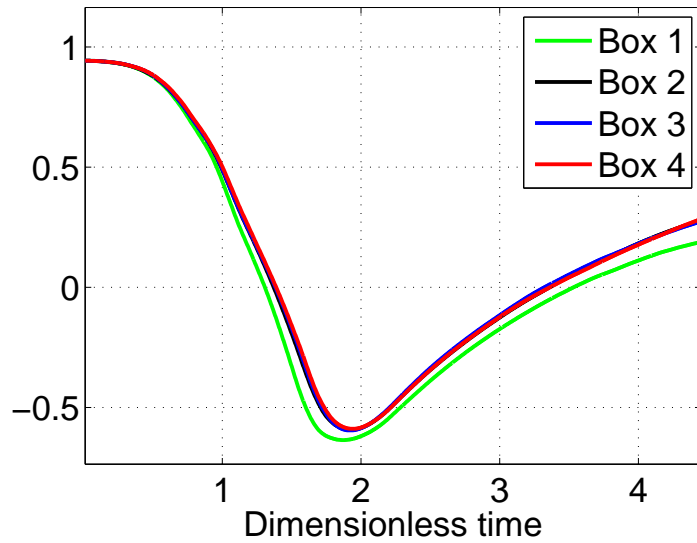


Figure 4.3: Position assumed by the end x -coordinate of the filament for different dimensions of the domain, from the smallest Box 1 (green line) to the biggest Box 4 (red line).

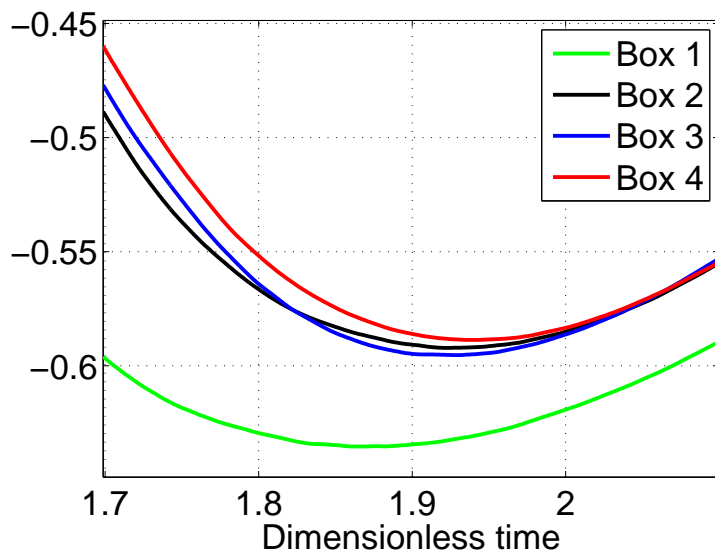


Figure 4.4: Detail of Figure (4.3).

smallest box are chosen such that way that all the Lagrangian points will be inside the space $\tilde{\Omega}$, while dimensions of Ω are investigated during the tests of convergence. Considering a saccade movement in the positive direction of the x -axis, we imposed x_1 as the left end point of the plate and x_2 as the x -coordinate the plate will assume at the end of the saccade movement. Since the movement is only on the positive side of the x -axis, the value x_{min} has been fixed a few points before x_1 . The value y_1 and y_{min} have been fixed such that at least three points in the domain are included to compute the discrete first order derivative of the arclength, while y_{max} has to be at least equal to the length of the filament plus the height of the plate, in this way the filament will be inside the smallest box during the whole simulation. In the convergence tests presented in Figures (4.3) and (4.4) four types of boxes are evaluated:

$$\mathbf{First\ Box:} \quad A_x : [x_{min}, x_1 + 2 \cdot L]; \quad B_y : [y_1, y_{plate} + L]$$

$$\mathbf{Box\ 2:} \quad A_x : [x_{min}, x_1 + 5 \cdot L]; \quad B_y : [y_1, y_{plate} + 3 \cdot L]$$

$$\mathbf{Box\ 3:} \quad A_x : [x_{min}, x_1 + 10 \cdot L]; \quad B_y : [y_1, y_{plate} + 5 \cdot L]$$

$$\mathbf{Box\ 4:} \quad A_x : [x_{min}, x_1 + 12 \cdot L]; \quad B_y : [y_1, y_{plate} + 6 \cdot L]$$

where L is the dimensionless length of the filament, y_{plate} is the vertical position of the plate. Moreover $B_x : [x_1, x_2]$, x_{min} and y_1 are maintained fixed through all four simulations.

With this test we noticed how the convergence is reached with a computational domain having the dimensions of Box 4, for this reason its values are used in further simulations.

The method by Huang *et al.*

In this case the period boundary conditions are used for the vertical edges of Ω , while Dirichlet and Neumann conditions are applied on the horizontal ones. In contrast with the previous method, this one allows us to use a smaller computational box. Since Equation (3.18) is verified, the plate could move through one of the vertical borders re-entering from the opposite one, the same is valid for the fluid. In order to save space and time execution of simulations, we set the same length for the computational box and the plate. Applying the same convergence tests we used in the previous method, we compared different computational boxes. We started with a domain Ω , called *First Box* in Figure (4.5), as reference and then we enlarged its width and height. The values used in details are:

First Box: $A_x : [x_{min}, 2.5 \cdot L]; A_y : [y_{min}, y_{plate} + 2 \cdot L];$
 $B_x : [x_{min}, 2.5 \cdot L]; B_y : [y_{min}, y_2]$

1.5·W: $A_x : [x_{min}, 1.5(2.5 \cdot L)]; A_y : [y_{min}, y_{plate} + 2 \cdot L];$
 $B_x : [x_{min}, 1.5(2.5 \cdot L)]; B_y : [y_{min}, y_2]$

1.5·H: $A_x : [x_{min}, 2.5 \cdot L]; A_y : [y_{min}, y_{plate} + 1.5(2 \cdot L)];$
 $B_x : [x_{min}, 2.5 \cdot L]; B_y : [y_{min}, y_2]$

2·W: $A_x : [x_{min}, 2(2.5 \cdot L)]; A_y : [y_{min}, y_{plate} + 2 \cdot L];$
 $B_x : [x_{min}, 2(2.5 \cdot L)]; B_y : [y_{min}, y_2]$

2·H: $A_x : [x_{min}, 2.5 \cdot L]; A_y : [y_{min}, y_{plate} + 2(2 \cdot L)];$
 $B_x : [x_{min}, 2.5 \cdot L]; B_y : [y_{min}, y_2]$

2·H & 2·W: $A_x : [x_{min}, 2(2.5 \cdot L)]; A_y : [y_{min}, y_{plate} + 2(2 \cdot L)];$
 $B_x : [x_{min}, 2(2.5 \cdot L)]; B_y : [y_{min}, y_2]$

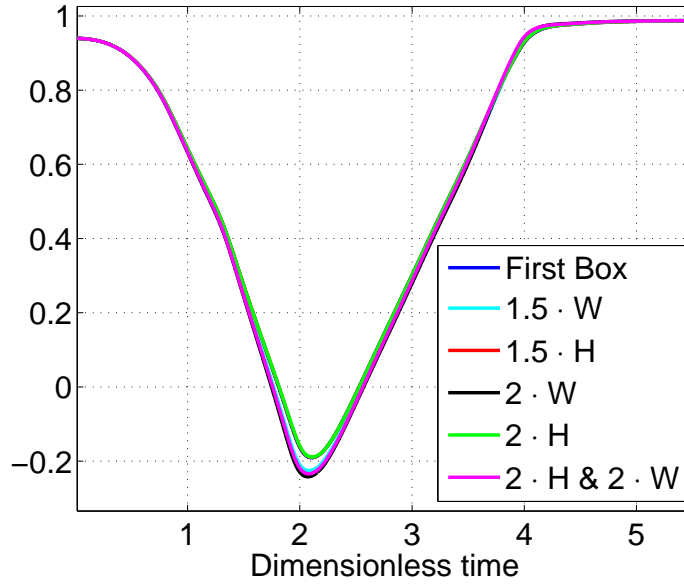


Figure 4.5: Position assumed by the end x -coordinate of the filament for different dimensions of the domain, where the notation $1.5 \cdot W$ and $2 \cdot W$ denotes a box width equal to 1.5 and 2 times the width of First Box, while with $1.5 \cdot H$ and $2 \cdot H$ the height of the box has been increased 1.5 and 2 times the height of First Box. Eventually the notation $2 \cdot H \& 2 \cdot W$ denotes a domain with twice the size of First Box.

From the results shown in Figures (4.5) and (4.6) we decided to take in account the computational box called $2 \cdot H \& 2 \cdot W$.

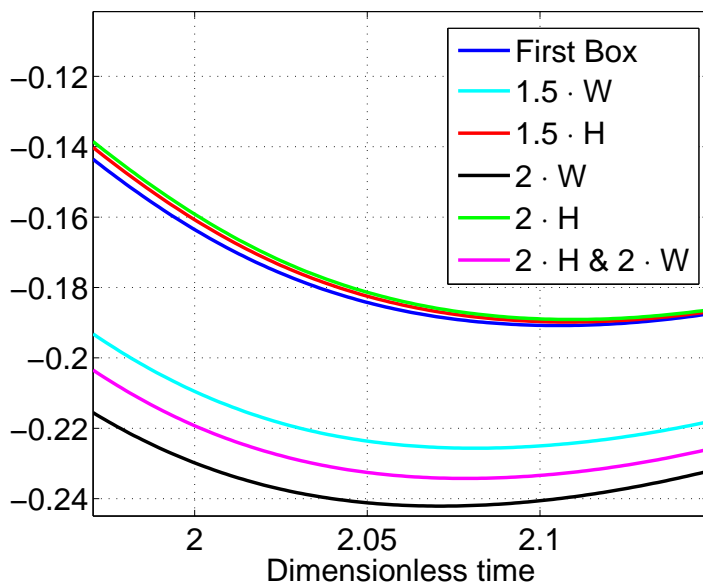


Figure 4.6: Detail of Figure (4.5).

4.2 Configuration of the simulations

In order to simulate the retinal detachment in two dimensions we employed two types of configurations. For the retinal detachment we used one flexible filament clamped at the wall with a certain angle, while for the retinal break we used two clamped filaments connected at their end points by a spring working only in traction. With Table 4.1 the physical parameters used in our simulations are shown, while in Table (4.2) the numerical parameters are enumerated.

Physical parameter	Symbol	Unit	Typical values	Reference
Retinal Young Modulus	E	Pa	$10^3, 10^4, 10^5$	[20] [21]
Retinal thickness	d	μm	200 - 350	[20] [22] [23]
Internal radius of eye shell	R	mm	12	[24] [25]
Saccadic amplitude	A	deg	8, 20	[5]

Table 4.1: List of the physical parameters used during our simulations.

In this table two different sets of parameters can be noticed, one for the filament model made by Newren *et al.* while the second has been chosen for Huang's *et al.* model. The reason of this choice is related to the simulations we executed. We began our trial runs with the Newren model using the extent of the detached retina as the characteristic lengths which was equal to 3 mm, and a saccade of 20 degrees to which corresponds a maximum velocity of 426 deg/s, used as characteristic velocity. These values are based on the studies made by Repetto *et al.* [5] for the saccadic movement and the research of Foster *et al.* [7] for the range of possible values of Reynolds number. Applying the same values in the model of Huang *et al.* the filament, during the simulation of retinal tear, eventually collided with the plate.

Numerical parameter	Symbol	Unit	Newren model	Huang model
Characteristic length	L	mm	3	2
Saccadic amplitude	A	deg	20	8
Characteristic velocity	U	mm/s	87.2	57.3
Characteristic time	T	s	0.033	0.035
Vitreous viscosity	ν	m ² /s	10 ⁻⁶	10 ⁻⁶
Vitreous density	ρ_0	Kg/m ³	10 ³	10 ³
Reynolds number	Re		267.6	114.6
Bending stiffness	K_b	Pa·m ⁴	10 ⁻¹¹ – 10 ⁻⁷	10 ⁻¹¹ – 10 ⁻⁷

Table 4.2: List of the numerical parameters used to simulate the filaments with the Newren and Huang models.

Since collisions are not modeled in this code, the following values has been used: the extent of the detached retina considered for the characteristic length was 2 mm; the saccadic amplitude was reduced to 8 degrees, with a maximum velocity of 273 deg/s, which means also that the Reynolds number has been decreased to 114.6. In Figure (4.7) the two velocity profiles are shown. The total simulation time was one saccadic motion plus an additional six times the saccadic period, to evaluate the relaxation movement of the filament.

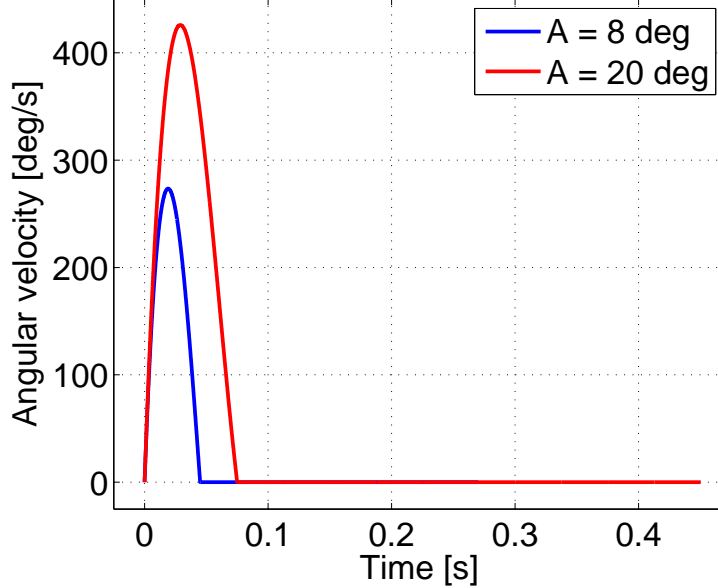


Figure 4.7: Saccadic velocity profiles used in our simulations for different amplitudes. After the saccadic movement the simulation continued at angular velocity equal to zero to evaluate the relaxation movement of the filament.

In both cases we evaluated the bending stiffness using the following formula :

$$K_b = E \cdot I = E \cdot \frac{bh^3}{12}, \quad (4.2)$$

where E is the Young Modulus, I is the area moment of inertia of the filament cross-section, h is the thickness of the detached retina and b is the depth of the filament. Since in literature different values can be found for the Young Modulus [20] [21] and the thickness [20] [22] [23], we were able to define a range of values for the bending stiffness, which order of magnitude goes from 10^{-10} Pa·m⁴ to 10^{-7} Pa·m⁴.

Eventually we approximated the vitreous humour as water, which means that we considered a density of $\rho_0 = 10^3$ Kg/m³ and a kinematic viscosity of $\nu = 10^{-6}$ m²/s.

4.3 Results with Newren *et al.* model

Retinal Break

In this section we show the results produced with the model made by Newren *et al.* [12] and observe the behavior of the forces the filament exerts on the plate and its movement during the whole simulation. Since the bending stiffness can be chosen in the range between 10^{-10} Pa·m⁴ and 10^{-7} Pa·m⁴, as shown in Table (4.2), we decided to set this value to $6.66 \cdot 10^{-10}$ Pa·m⁴, whereas higher values are characterized by a stiffer movement of the filament. As discuss in the previous chapter, the stretching coefficient is not a physical value but a numerical one, since this parameter is chosen such that the filament do not exceeds a certain value of stretching.

Along with the parameters shown in Table (4.2), we simulated three different lengths for the filament: 1.5mm, 3mm and 4.5mm.

In Figures (4.8) and (4.9) it is possible to analyze the movement of the filament tip with respect to the first fixed point. Analyzing this movement it can be noticed how the filament tends to a certain relaxed position depending on its length. Moreover Figure (4.11) demonstrates that increasing the filament length, from 3mm to 4.5mm, leads to completely different dynamics. This can be explained by the fact that since the bending stiffness is kept constant, the apparent stiffness of the larger filament is smaller. Since we think this kind of movement is hard to be found inside the eye, we decided to exclude this length from further simulations.

Along with the movement we also observed the force the filament exerts on the plate during the simulation. What we found was that the forces and the torque signals vary rapidly, and in a unphysical manner, with time. The amplitudes and the frequencies are large which prevents us to study the dynamic behavior of the filament. Since all Lagrangian points composing the filament are connected through springs, and all of them are free to move in traction and compression, we think that their action could influence the force signal, resulting in noise. In Figure (4.10) this issue is pointed out with the horizontal force the filament applies on the plate, using 1.5mm as its length. Eventually, the same type of noise has been found in all the cases we tested.

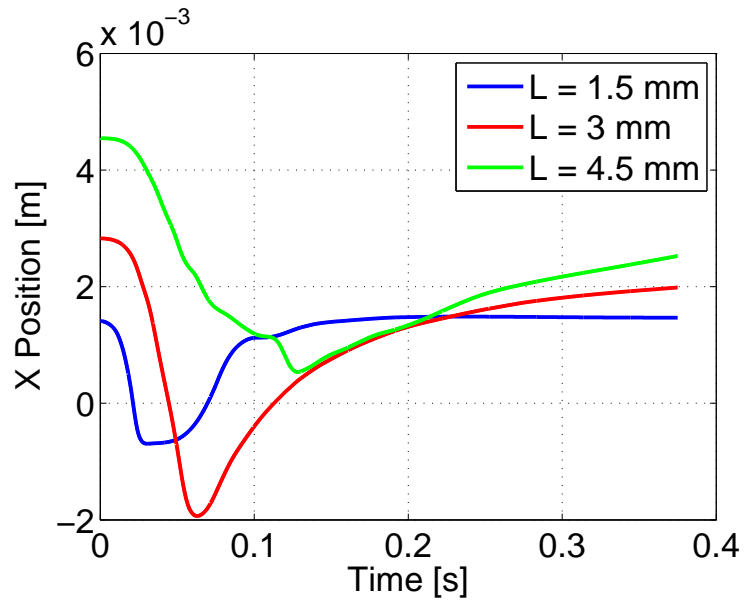


Figure 4.8: Position of the x coordinate of the end point in respect to the first fixed point.

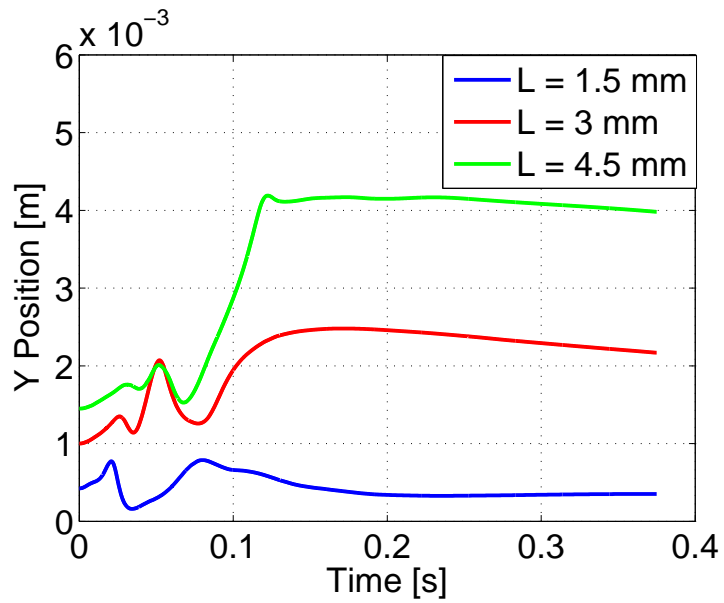


Figure 4.9: Position of the y coordinate of the end point in respect to the first fixed point.

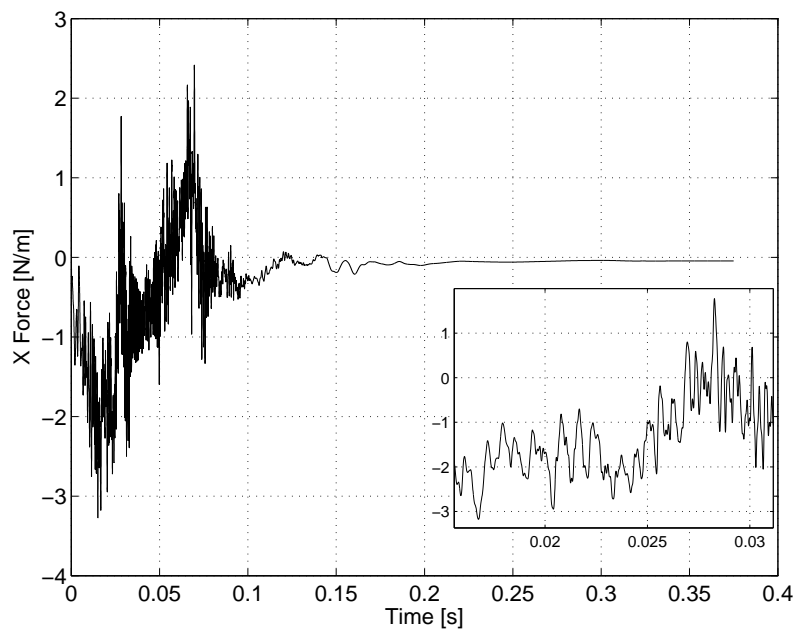


Figure 4.10: An example of the force, per unit depth, exerted on the plate which affected by noise due to the action of the springs connecting the Lagrangian points. In this case the horizontal force is shown for a filament with length $L_f = 1.5\text{mm}$.

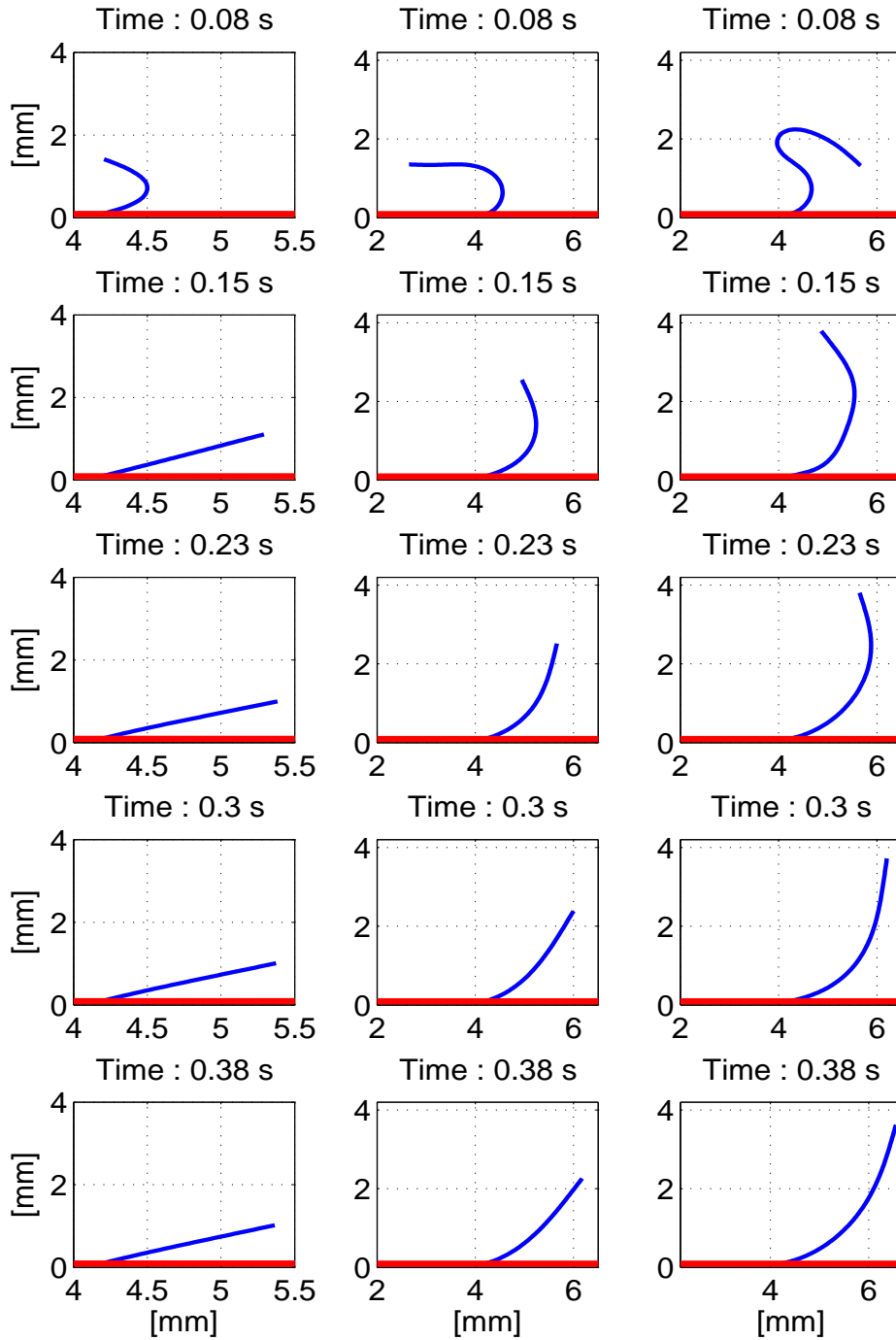


Figure 4.11: Movement of the filament during the simulation after the saccade movement. The first column is referred at the filament with length $L_f = 1.5$ mm; the second column is with $L_f = 3$ mm; while the third column shows the movement for $L_f = 4.5$ mm. The saccadic movement started at 0 second and ended at 0.08 seconds, from 0.08 seconds till the end of the simulation the velocity of the plate was equal to zero.

Retinal Hole

Along with the retinal break, we simulated the retinal hole with the geometry illustrated in the previous chapter. A spring, working only in traction, has been introduced between the two end points to avoid that the filaments will move independently of one another. The idea with the spring is to model the action of the third dimension by limiting the relative mobility of the two filaments. In other words, the filaments are allowed to come closer but not further apart since they are limited by the width of the hole. We fixed the distance between them to 1mm.

For these simulations we used the same parameters presented in Table (4.1) and Table (4.2) and we decided to fix the bending stiffness to the value $6.66 \cdot 10^{-10} \text{ Pa} \cdot \text{m}^4$. Eventually the three lengths of the filament, 1.5mm, 3mm and 4.5mm, were tested. As for the retinal break, the code works correctly regarding the movement. In Figure (4.12) the displacement, along x axis and y axis, of the end points are shown, for both filaments, with respect to their attached point. The first column represents the movement of the left filament, while the right column represents the other one. In this figure all the lengths used are compared, where the green line corresponds to $L_f = 4.5\text{mm}$, the red line stands for $L_f = 3\text{mm}$ and the blue line describes $L_f = 1.5\text{mm}$.

Studying the movement with Figure (4.12) and Figure (4.14) we noticed that, since the saccade is directed towards the positive values of the x axis, during the accelerated phase the fluid raises the filament from its central section. Due to the presence of a spring between the two end tips, this movement forces the right filament to lower its position, getting closer to the plate. Once the saccade is terminated, the fluid, which still moves, pushes the left filament towards the plate and rises the right one. At the end of the simulation, the left filament is risen again thanks to the action of the spring.

Also in the case of the retinal hole the force signal is noisy and does not allow us to analyze the forces in a proper manner and to compare with the retinal break. In Figure (4.13) there is an example of the signal we obtained, in this case the horizontal and vertical forces of the left filament are shown.

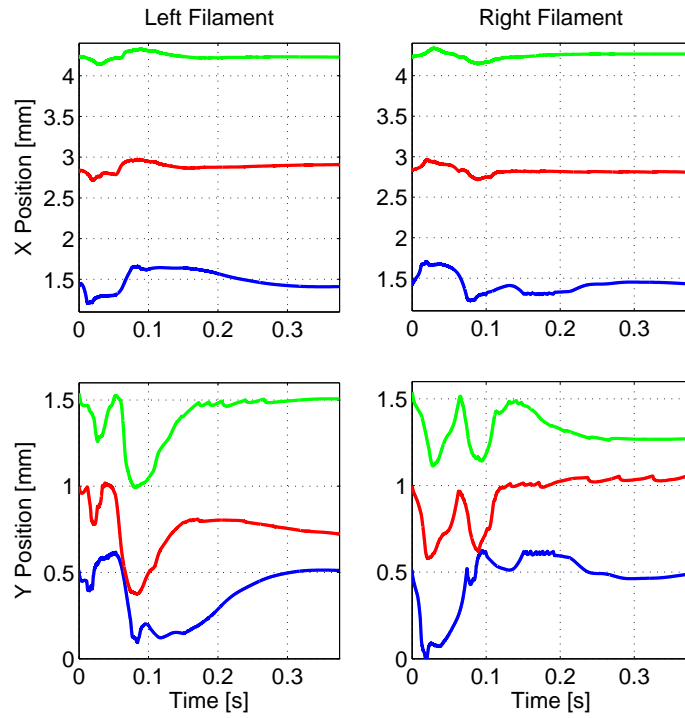


Figure 4.12: Movement of the left filament, first column, and the right filament, right column, during the simulation. The position along the x axis and y axis are shown for all the lengths used: $L_f = 4.5\text{mm}$ (green line); $L_f = 3\text{mm}$ (red line) and $L_f = 1.5\text{mm}$ (blue line).

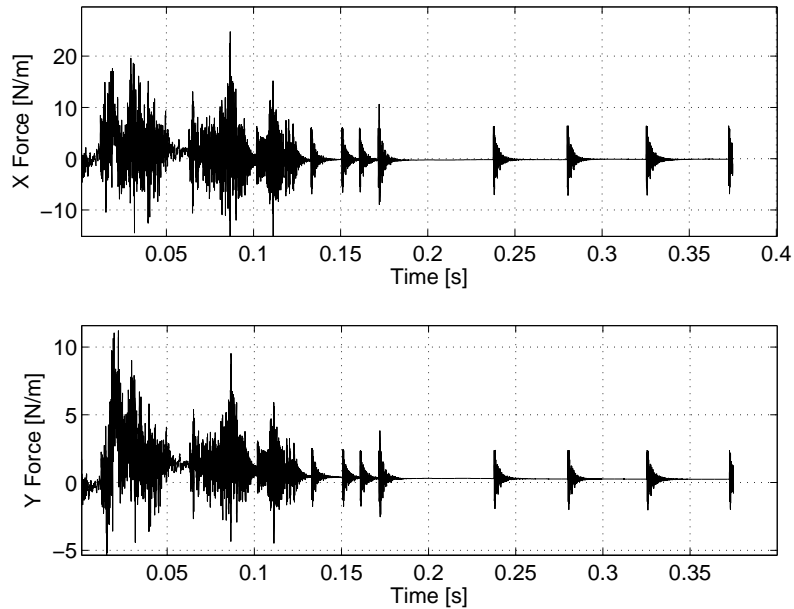


Figure 4.13: An example of the force, per unit depth, exerted on the plate which is afflicted by a noise due to the action of the springs among the Lagrangian points. In this case the horizontal and vertical forces are shown for the left filament with length $L_f = 1.5\text{mm}$.

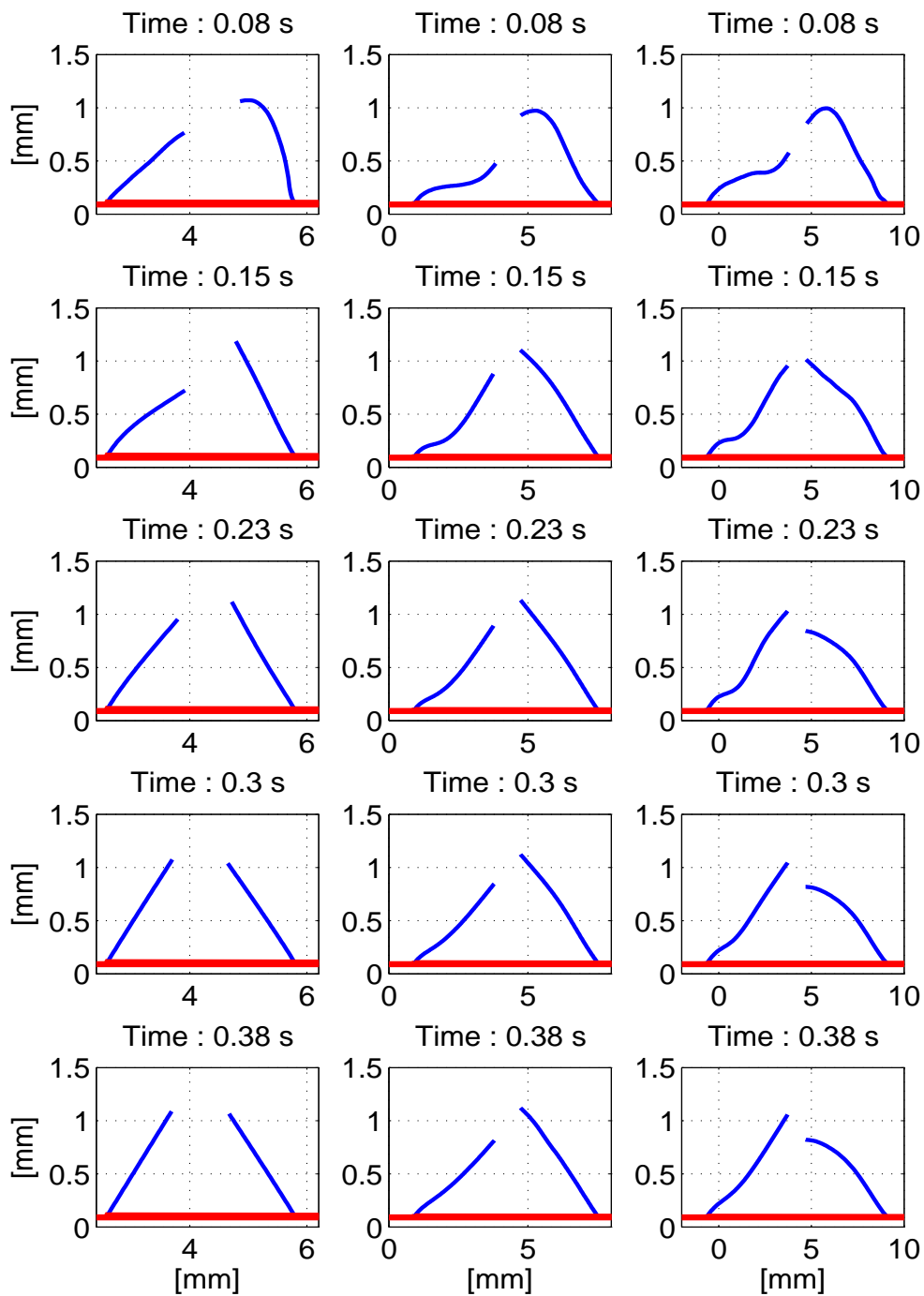


Figure 4.14: Movement of the two filaments during the simulation. The first column is referred to the filament with length $L_f = 1.5$ mm; the second column is with $L_f = 3$ mm; while the third column shows the movement for $L_f = 4.5$ mm. The saccadic movement started at 0 second and ended at 0.08 seconds, from 0.08 seconds till the end of the simulation the velocity of the plate was equal to zero.

4.4 Results with Huang *et al.* model

Once we observed the results obtained with the model of Newren *et al.* [12] we decided to maintain the same solver for the fluid motion, see Peskin [11], and change the filament solver using the solution proposed by Huang *et al.* [13].

We first tested the retinal break using the same parameters of the previous model. Nevertheless the filament collided with the plate immediately after the saccadic movement. Since the code does not handle the contact of the Lagrangian points of the filament with the Lagrangian points of the plate, the filament started to oscillate leading to an increase in amplitude of the force on the attached point. For this reason we used a different set of parameters, shown in Table (4.2), decreasing both the Reynolds number and the characteristic length.

We used the model made by Huang *et al.* to simulate retinal detachments and retinal holes varying the length of the filament and its bending stiffness. The values we used are :

- Bending stiffness : $K_b = 5.25 \cdot 10^{-11} Pa \cdot m^4$; $2.62 \cdot 10^{-10} Pa \cdot m^4$; $1.31 \cdot 10^{-9} Pa \cdot m^4$;
- Filament length : $L_f = 1mm$; $1.5mm$; $2mm$.

Retinal Break

The results we obtained for the retinal break simulations are shown in Figure (4.15), (4.16), (4.17) and (4.18). In Figure (4.15) the movement for the three chosen lengths are presented for different time steps; Figure (4.16) is divided in three rows, each one for a specific length, where the magnitude and the angle of the force vector acting on the plate is presented. In order to clarify if the angle defines a force vector in traction or compression we used a coordinate system orthogonal to the relaxed position of the filament. Considering this system the range in which the force vectors act in traction is $[-90^\circ; 90^\circ]$, while in the remaining range the force is in compression. With a coordinate system orthogonal to the plate these range are $[-70^\circ; 110^\circ]$ for the traction force and $[-180^\circ; -70^\circ] \cup [110^\circ; 180^\circ]$. In Figure (4.17) and (4.18) the torque acting on the plate is shown. Analyzing these graphs the characteristics of the simulated retinal detachment can be defined.

During the accelerated phase of the saccadic movement the filament exerts a counterclockwise torque on the attached point and the magnitude of the force increases until 0.02 seconds, where the maximum velocity is reached. Since the angle of the force vector is higher than 110 degrees, this means that the force is acting in compression. The reason can be found by thinking about the starting condition. At the beginning the fluid has no velocity and the filament is defined at the remaining position. When the plate starts to move, towards the positive values of the x axis, the filament is drifted on its left side resulting in a compression force on the attached point. The force is kept in compression while the plate is in movement. After 0.019 seconds the plate starts to decelerate resulting in a reduction in the magnitude of the force. Analyzing the angle it can be notice how the force is changed in traction near 0.025 seconds, since the angle amplitude is lower than 100 degrees. This can be explained by looking at the position of the filament in Figure (4.15). From 0.019

seconds to 0.04 seconds the filament bends on its left side, enclosing the fluid near the plate. While the the latter is slowing down, the fluid continues its movement towards the right side, against the filament. This action results in a traction force exerted on the plate. The saccade ends at 0.045 seconds and it can be noticed that once the plate terminates its movement, the torque changes its direction in clockwise. Moreover the magnitude of the force is characterized by another peak but in this case the force is acting in traction. For the resting part of the simulation the fluid continues to push the filament against the plate, until the final position is reached. It is interesting to noticed the position of the filament with length $L_f = 1.5\text{mm}$ and $L_f = 2\text{mm}$, with a bending stiffness of $K_b = 2.62 \cdot 10^{-10} \text{Pa} \cdot \text{m}^4$ (red lines), at the time 0.07 seconds and 0.1 seconds respectively. Analyzing the magnitude of force and its angle in Figure (4.16) in can be noticed how a compression force in generated.

The entire simulation can be distinguished into two phases. The first one is characterized by the saccadic movement, where the filament exerts on the plate a counterclockwise torque and a compression force, during the accelerated phase, followed by a traction force. The second phase is defined by the resting plate, where the filaments exerts a counterclockwise torque and a traction force.

Analyzing Figure (4.16) and (4.17) we noticed how the magnitude of force and the torque increase with the bending stiffness. Moreover, studying Figure (4.16), (4.16) and (4.18), it is clear how the bending stiffness of $K_b = 1.31 \cdot 10^{-9} \text{Pa} \cdot \text{m}^4$ results in a filament with an excessive stiffness. In Figure (4.18) we show how the length of the filament has a minimum influence on the torque.

Through Figures (4.19) and (4.20) the pressure field is shown. It is clear that during the accelerated phase of the saccade, which goes from 0 to 0.019 seconds, the filament moves the fluid towards the positive values of the x axis, which results in a positive pressure on the right side of the filament and a negative pressure on the left side. Once the plate starts to decelerate these values are inverted, the pressure is positive on the left side of the filament while the negative pressure is on the right side. This means that while the filament is slowing down the fluid, which has higher velocity, pushes the filament toward the plate. During the final phase of the simulation the fluid loses its velocity and the pressure is stabilized around 0 Pa/m. The described behavior can also be observed in Figures (4.21) and (4.22) where the vorticity is shown. The action of the fluid pushing the filament towards the plate can be explained also due to the presence of a vortex over the filament, once the movement has taken place.

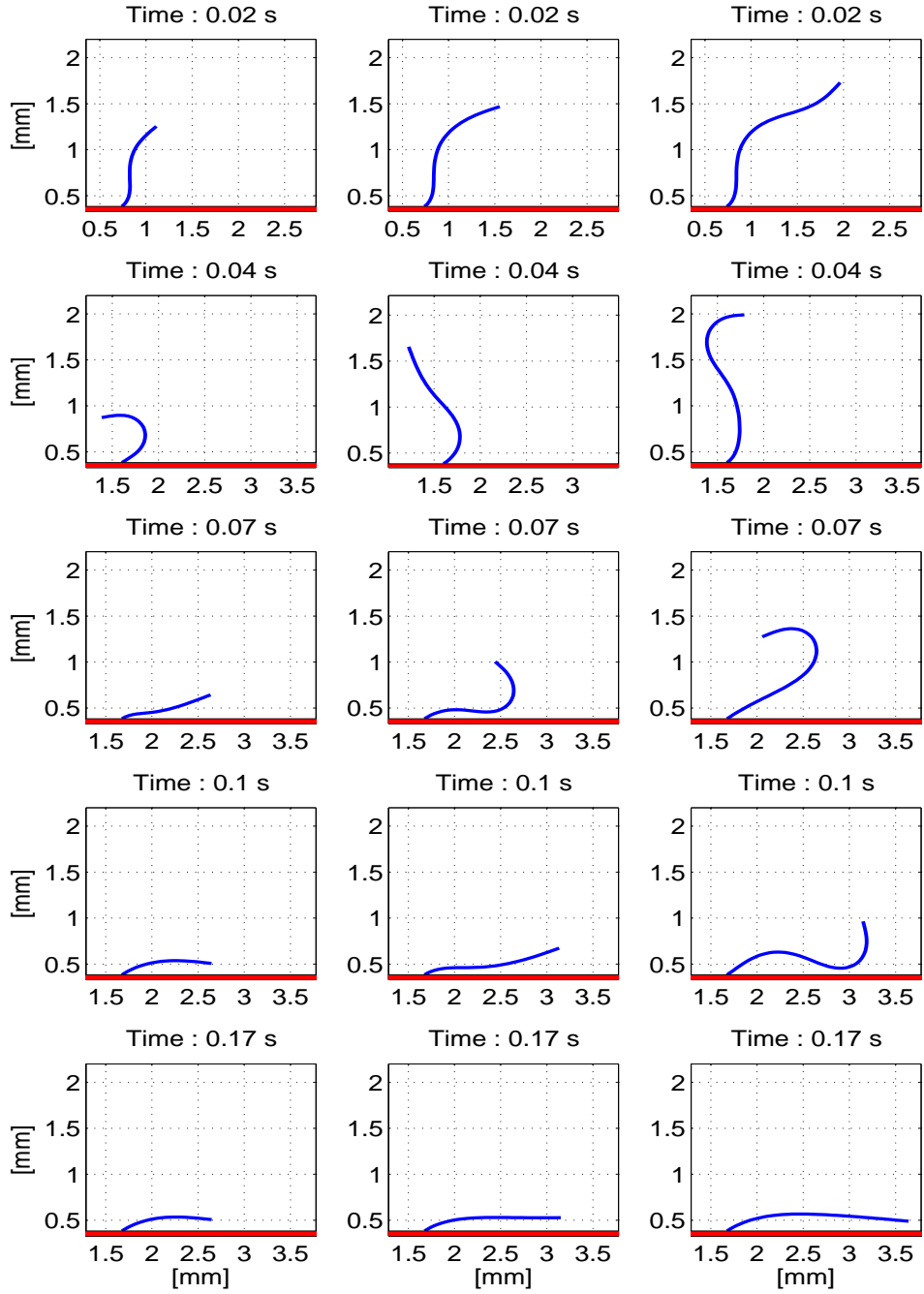


Figure 4.15: Movement of the filament, with a bending stiffness of $2.62 \cdot 10^{-10} Pa \cdot m^4$, during the simulation. The first column is referred at the filament with length $L_f = 1.0$ mm, while the second column shows the movement for $L_f = 1.5$ mm and the last column is for $L_f = 2.0$ mm. The saccadic movement started at 0 second, the maximum velocity is reached at 0.019 seconds and the movement ends at 0.045 seconds. From 0.045 seconds till the end of the simulation the velocity of the plate is equal to zero.

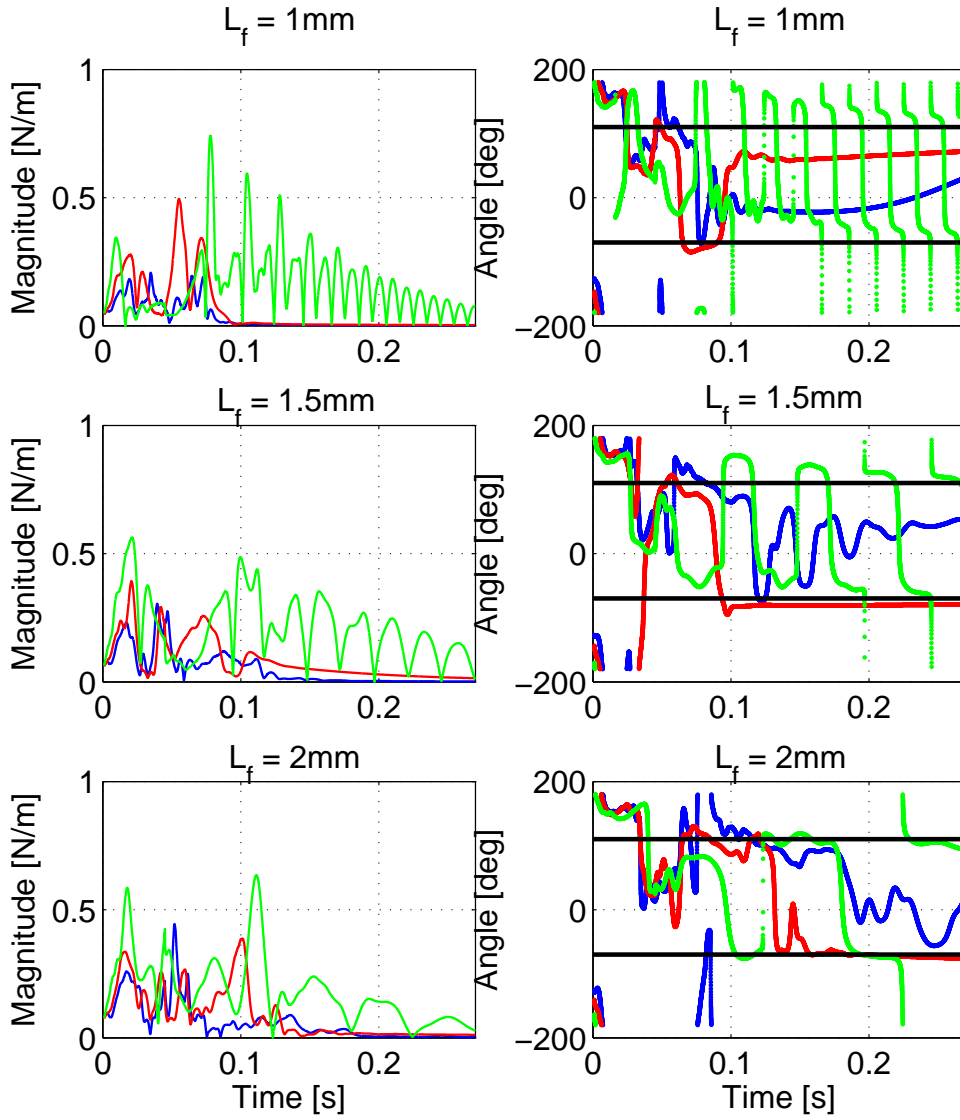


Figure 4.16: Magnitude of force, per unit depth, exerted by the filament of the plate for different lengths L_f . Each line identify a specific bending stiffness: $K_b = 5.25 \cdot 10^{-11} Pa \cdot m^4$ (blue line); $2.62 \cdot 10^{-10} Pa \cdot m^4$ (red line); $1.31 \cdot 10^{-9} Pa \cdot m^4$ (green line). In the angle amplitude two black lines are added to identify the range where the filament exerts a traction force $[-70^\circ; 110^\circ]$ from the range where it applies a compression force on the plate.

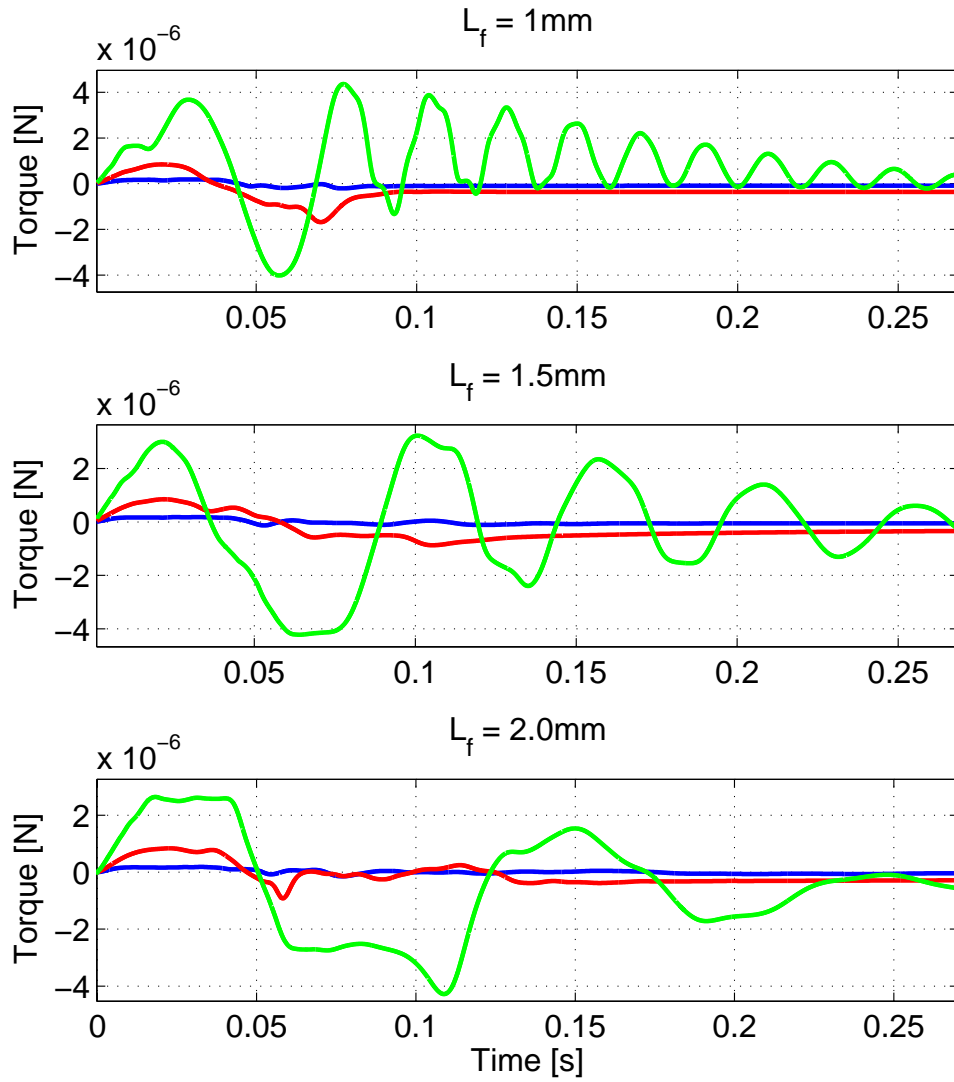


Figure 4.17: Torque, per unit depth, exerted by the filament on the plate for different lengths L_f . Each lines identify a specific bending stiffness: $K_b = 5.25 \cdot 10^{-11} Pa \cdot m^4$ (blue line); $2.62 \cdot 10^{-10} Pa \cdot m^4$ (red line); $1.31 \cdot 10^{-9} Pa \cdot m^4$ (green line). In these figures the positive values of the torque indicates a counterclockwise orientation, while the negative values stand for the counterclockwise orientation.

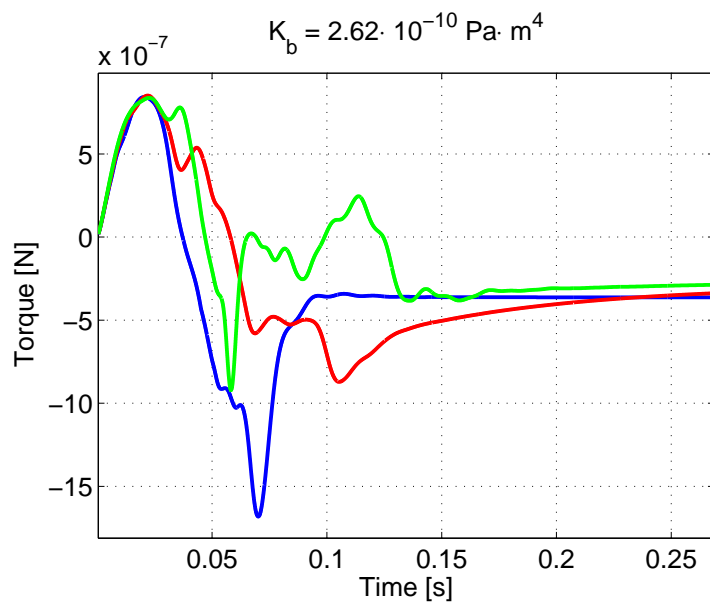


Figure 4.18: Torque, per unit depth, exerted by the filament on the plate for different lengths L_f . In this figure the bending stiffness is fixed at the value of $2.62 \cdot 10^{-10} \text{ Pa} \cdot \text{m}^4$. The positive values of the torque indicates a counterclockwise orientation, while the negative values stand for the counterclockwise orientation.

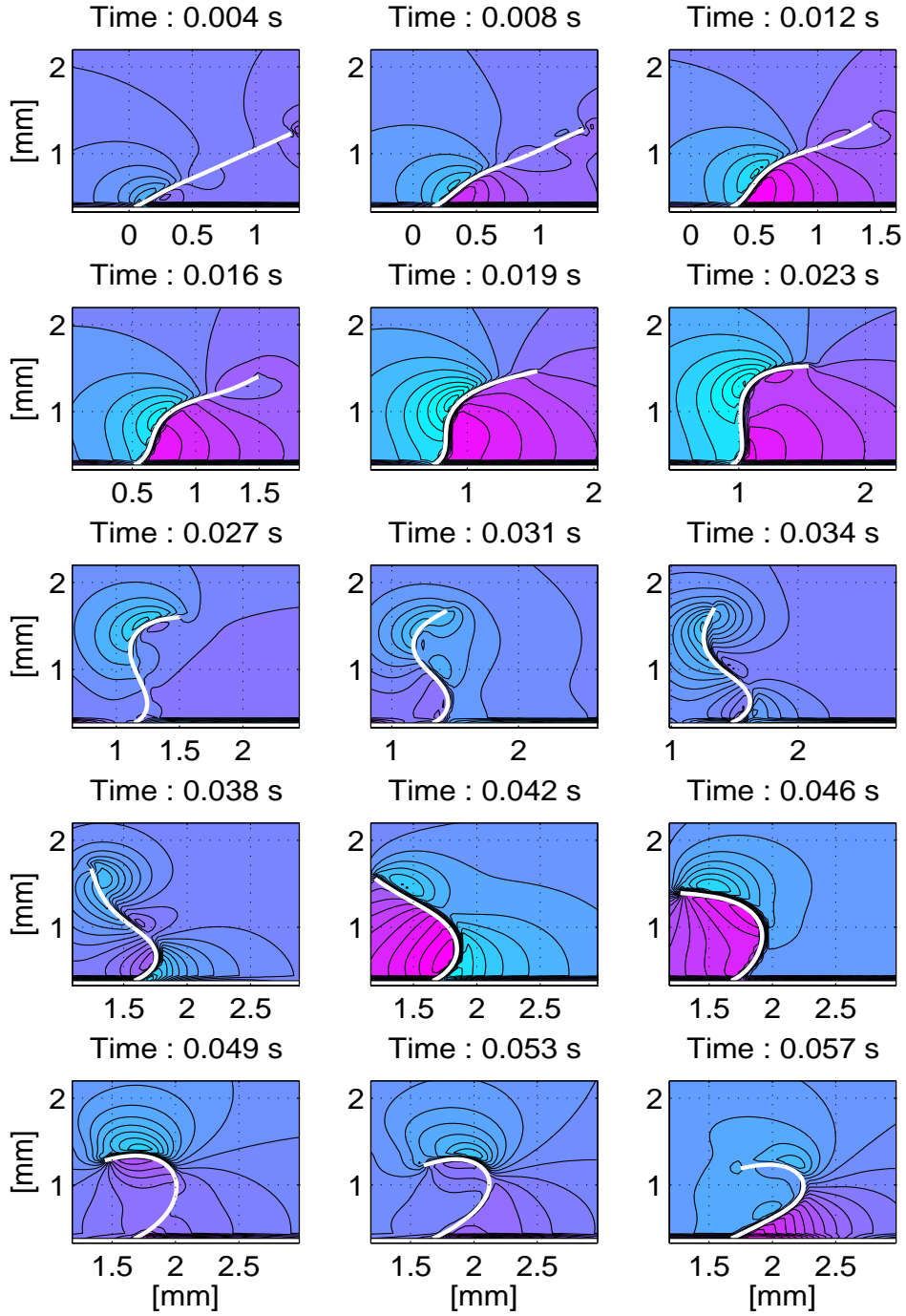


Figure 4.19: Pressure field during a simulation with $L_f = 1.5\text{mm}$ as filament length and bending stiffness of $2.62 \cdot 10^{-10}\text{Pa} \cdot \text{m}^4$. The pressure scale goes from -3.28 Pa (blue color) to 3.28 Pa (magenta color), with intervals of 0.01 Pa . The saccadic movement started at 0 second, the maximum velocity is reached at 0.019 seconds and the movement ends at 0.045 seconds. From 0.045 seconds till the end of the simulation the velocity of the plate is equal to zero.

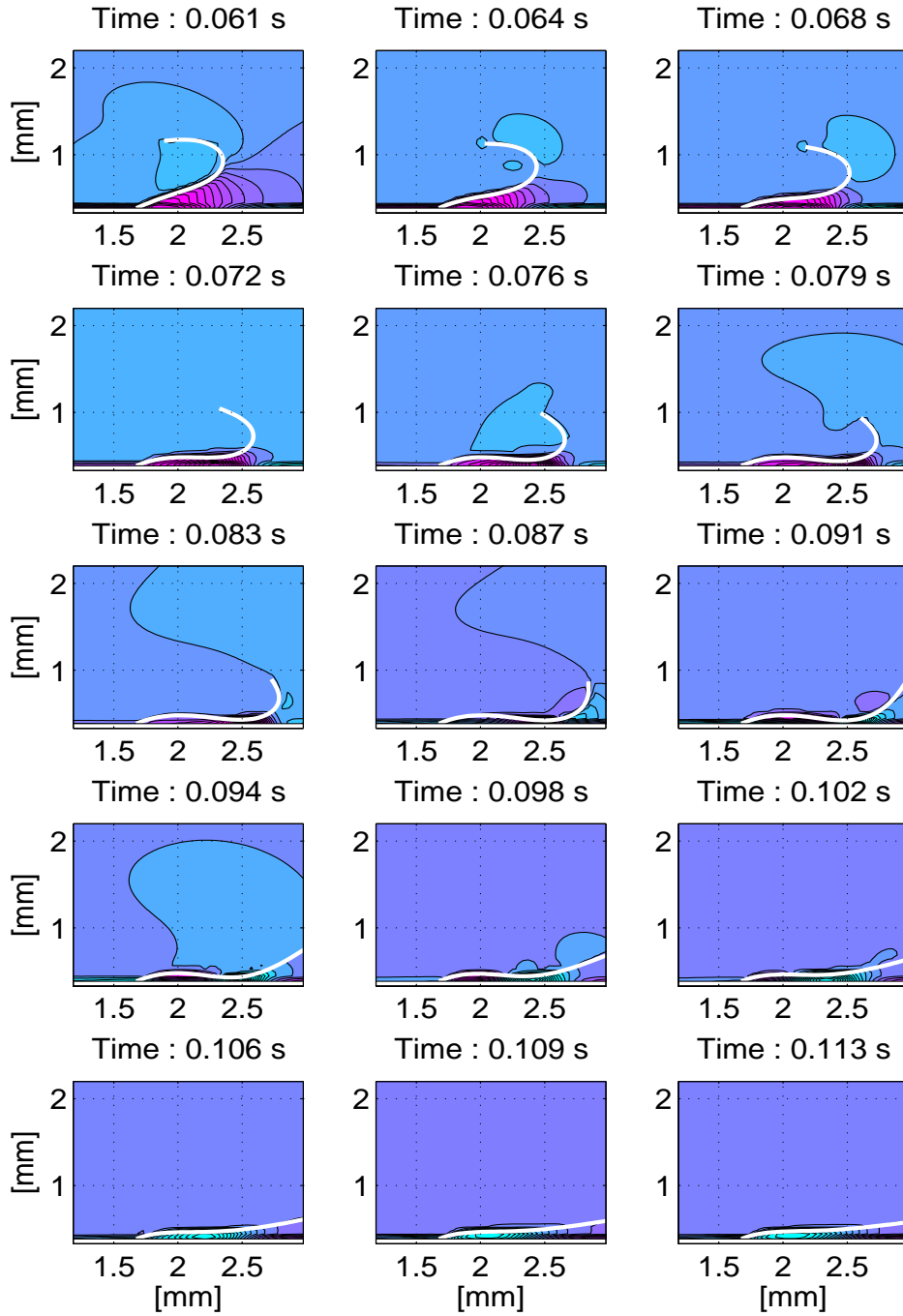


Figure 4.20: Pressure field during a simulation with $L_f = 1.5\text{mm}$ as filament length and bending stiffness of $2.62 \cdot 10^{-10} \text{Pa} \cdot \text{m}^4$. The pressure scale goes from -3.28 Pa (blue color) to 3.28 Pa (magenta color), with intervals of 0.01 Pa . The saccadic movement started at 0 second, the maximum velocity is reached at 0.019 seconds and the movement ends at 0.045 seconds. From 0.045 seconds till the end of the simulation the velocity of the plate is equal to zero.

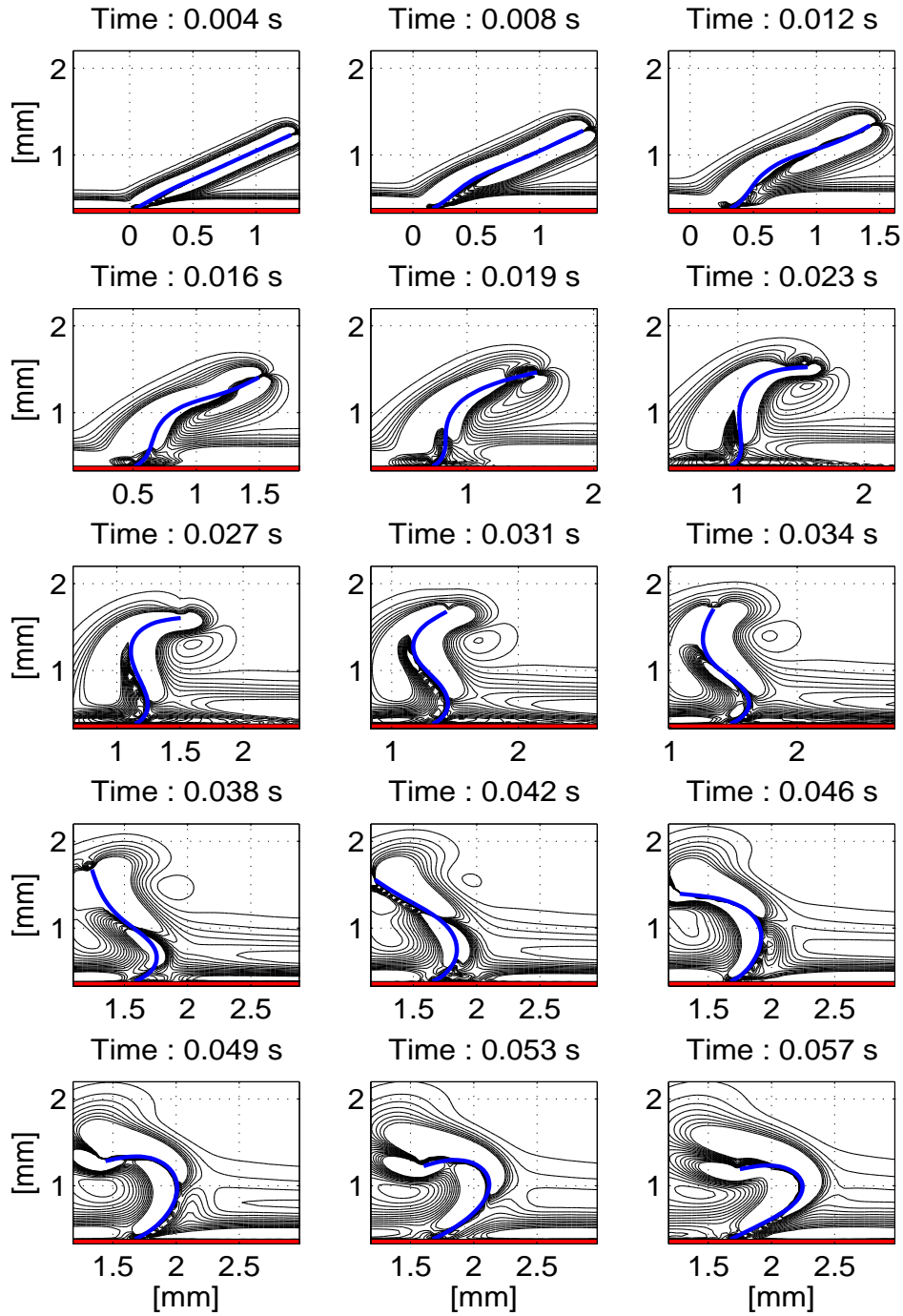


Figure 4.21: Vorticity field during a simulation with $L_f = 1.5\text{mm}$ as filament length and bending stiffness of $2.62 \cdot 10^{-10} \text{Pa} \cdot \text{m}^4$. The saccadic movement started at 0 second, the maximum velocity is reached at 0.019 seconds and the movement ends at 0.045 seconds. From 0.045 seconds till the end of the simulation the velocity of the plate is equal to zero.

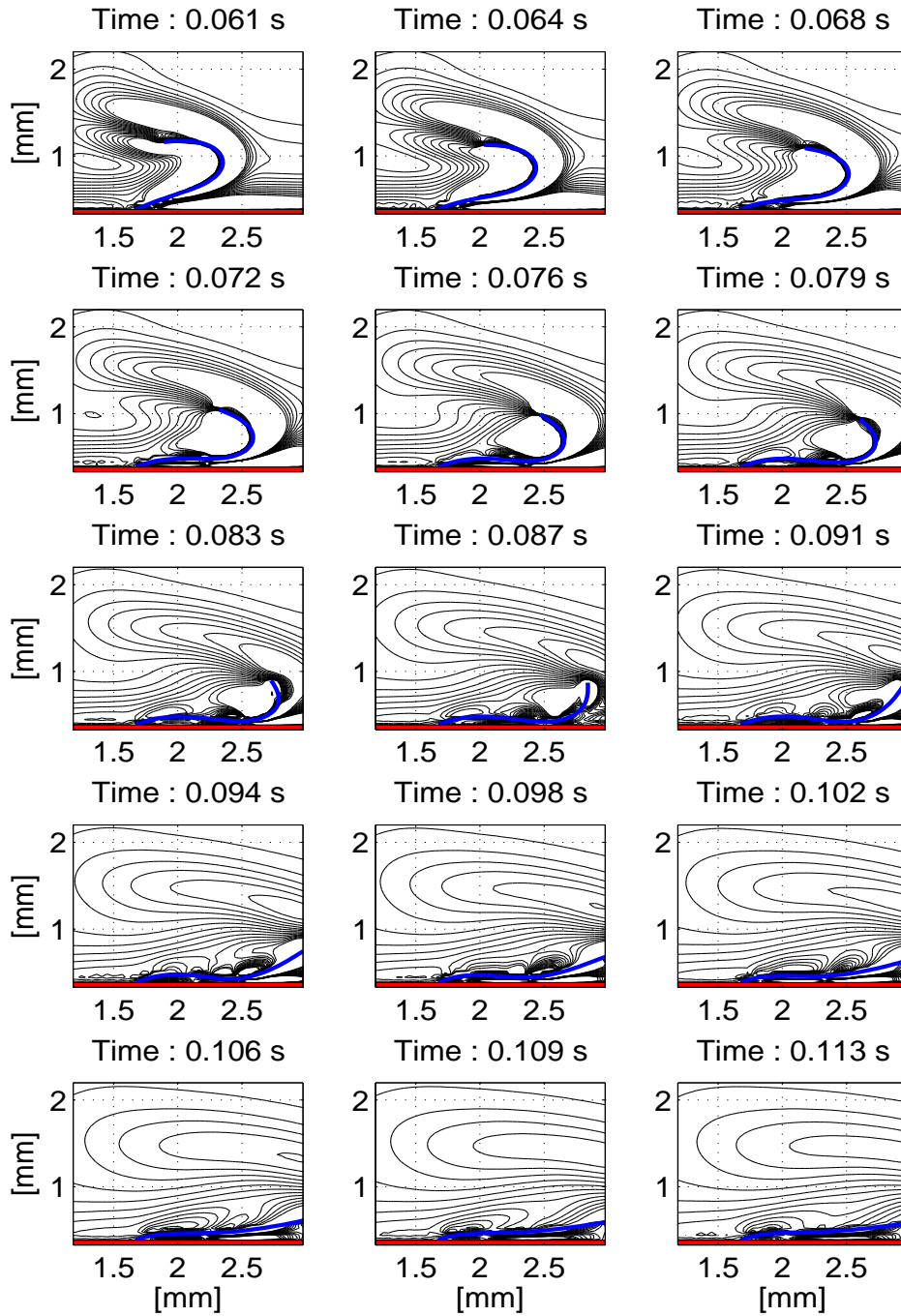


Figure 4.22: Vorticity field during a simulation with $L_f = 1.5\text{mm}$ as filament length and bending stiffness of $2.62 \cdot 10^{-10}\text{Pa} \cdot \text{m}^4$. The saccadic movement started at 0 second, the maximum velocity is reached at 0.019 seconds and the movement ends at 0.045 seconds. From 0.045 seconds till the end of the simulation the velocity of the plate is equal to zero.

Retinal Hole

To simulate the retinal hole we used the same parameters as in the case of the retinal break. The results are shown in Figure (4.23), (4.24), (4.25), (4.26) and (4.27). Figure (4.23) shows the movement of the filaments with the three chosen lengths at different time steps; the magnitude and the angle of the force vector defined on the attached point is presented in Figures (4.24), (4.25), (4.26) for the length $L_f = 1\text{mm}$, 1.5mm and 2mm respectively. In these figures we used the same notation adopted in Figure (4.16) for the retinal break. In Figure (4.27) the torque acting on the plate is shown.

During the accelerated phase of the saccade the left filament behaves as the filament studied in the retinal break, which means it exerts a compression force on the plate. Nevertheless the right filament, even if it generates first a compression force, has a traction force on the plate while the maximum velocity is reached, at 0.019 seconds. This can be explained by studying Figure (4.23). Unlike the previous case, the filaments are not able to move freely, due to the presence of the spring connecting the two end points. Moreover the fluid between the filaments is an additional obstacle to the movement, since it could leave the simulated subretinal space only through the hole. This leads to a position of the filaments illustrated in the first row of Figure (4.23), where the left filament has a higher position and curvature with respect to the right filament. This specific configuration generates a compression force on the left attached point and a traction force on the right attached point. As for the forces also the torque has opposite directions, counterclockwise for the left filament and clockwise for the right filament. While the plate reduces its velocity, between 0.019 seconds and 0.045 seconds, the fluid inside the simulated subretinal space moves towards the right filament before exits through the hole. This generates a traction force which can be observed in Figures (4.24) (4.25) (4.26). Once the saccadic movement is ended, the magnitude of force on the left attached point tends toward zero, working mostly in traction, and its torque preserves a clockwise direction. A different behavior is observed for the right filament. The fluid inside the subretinal space produces an oscillating movement of the filament, which can be seen in the third and fourth row of Figure (4.23), generating a force working mostly in traction on the plate. Moreover this movement explains also why the left filament produces a traction force on the plate.

Examining the results obtained we noticed how the magnitude of force and the torque increase by lowering the bending stiffness, moreover the force increases its magnitude by increasing the length of the filaments. As for the retinal break, the length have not a strong influence on the torque.

Eventually with these experiments we noticed how the higher bending stiffness, in presence of filaments with length of 1.5mm and 2mm , is less influenced by the oscillating movement observed in the retinal break.

Analyzing Figures (4.28)-(4.29) and Figures (4.30)-(4.31) more information on the movement can be defined. During the acceleration movement, which goes from 0 to 0.019 seconds, the values of high pressure can be found inside the subretinal space. This value decreases with the deceleration phase of the plate. Around 0.022 seconds it can be noticed how a vortex is generated, pushing the left filament towards the plate. While the filaments are slowing down, the fluid continues its movement

towards the right side, raising the right filament and the pressure under it. Once the saccadic movement is finished an oscillation of the filaments can be noticed, which is produced by an oscillating pressure.

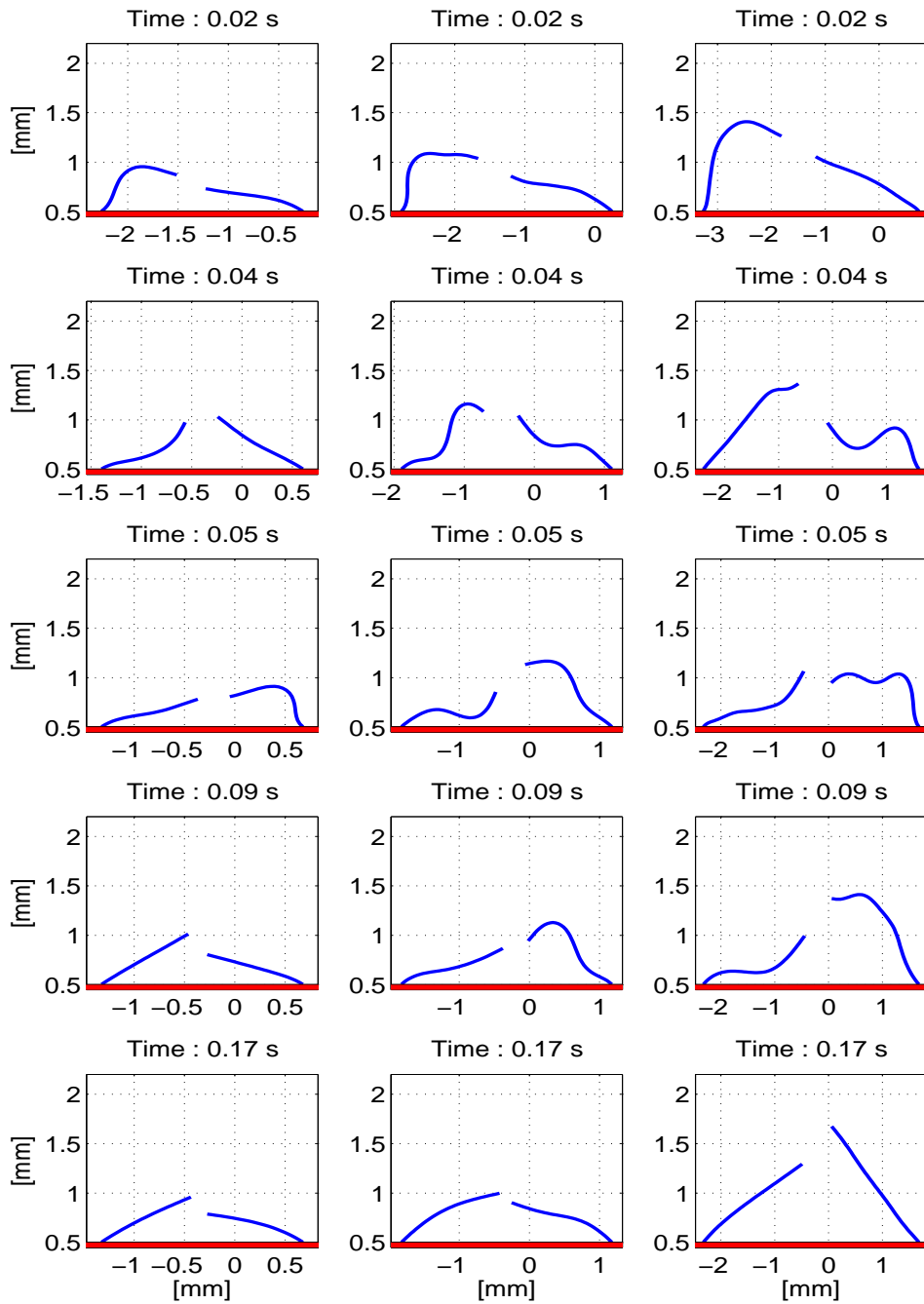


Figure 4.23: Movement of the filaments, with a bending stiffness of $2.62 \cdot 10^{-10} Pa \cdot m^4$, during the simulation. The first column is referred at the filament with length $L_f = 1.0mm$, while the second column shows the movement for $L_f = 1.5mm$ and the last column is for $L_f = 2.0mm$. The saccadic movement started at 0 second, the maximum velocity is reached at 0.019 seconds and the movement ends at 0.045 seconds. From 0.045 seconds till the end of the simulation the velocity of the plate is equal to zero.

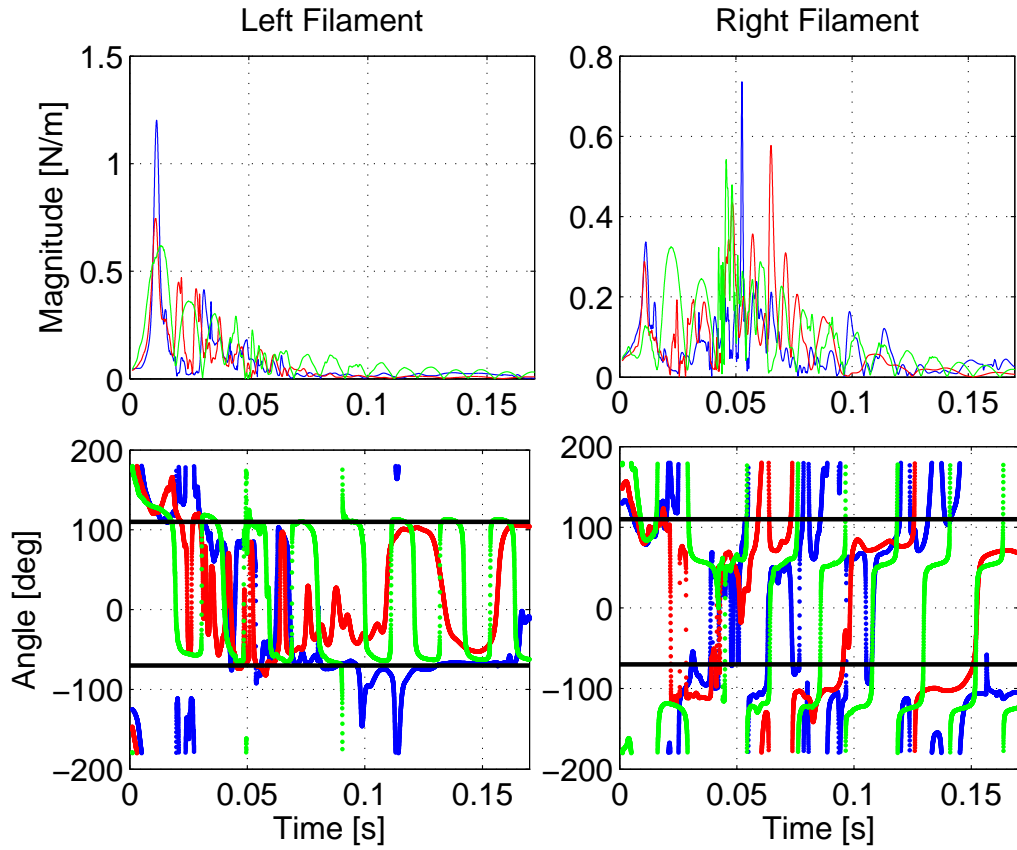


Figure 4.24: Magnitude, per unit depth, of force exerted by the left and right filaments of the plate with a lengths of $L_f = 1\text{mm}$. Each line identify a specific bending stiffness: $K_b = 5.25 \cdot 10^{-11} \text{Pa} \cdot \text{m}^4$ (blue line); $2.62 \cdot 10^{-10} \text{Pa} \cdot \text{m}^4$ (red line); $1.31 \cdot 10^{-9} \text{Pa} \cdot \text{m}^4$ (green line). In the angle amplitude two black lines are added to identify the range where the filament exerts a traction force $[-70^\circ; 110^\circ]$ from the range where it applies a compression force on the plate.

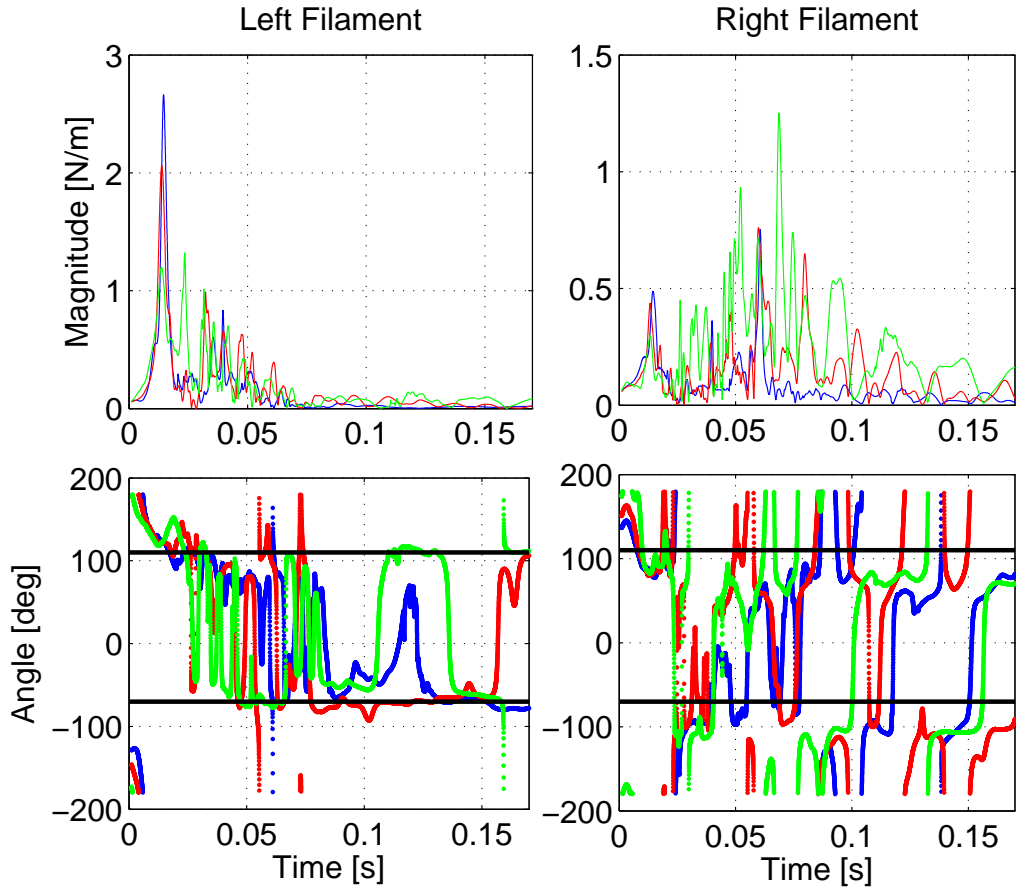


Figure 4.25: Magnitude, per unit depth, of force exerted by the left and right filaments of the plate with a lengths of $L_f = 1.5\text{mm}$. Each line identify a specific bending stiffness: $K_b = 5.25 \cdot 10^{-11} \text{Pa} \cdot \text{m}^4$ (blue line); $2.62 \cdot 10^{-10} \text{Pa} \cdot \text{m}^4$ (red line); $1.31 \cdot 10^{-9} \text{Pa} \cdot \text{m}^4$ (green line). In the angle amplitude two black lines are added to identify the range where the filament exerts a traction force $[-70^\circ; 110^\circ]$ from the range where it applies a compression force on the plate.

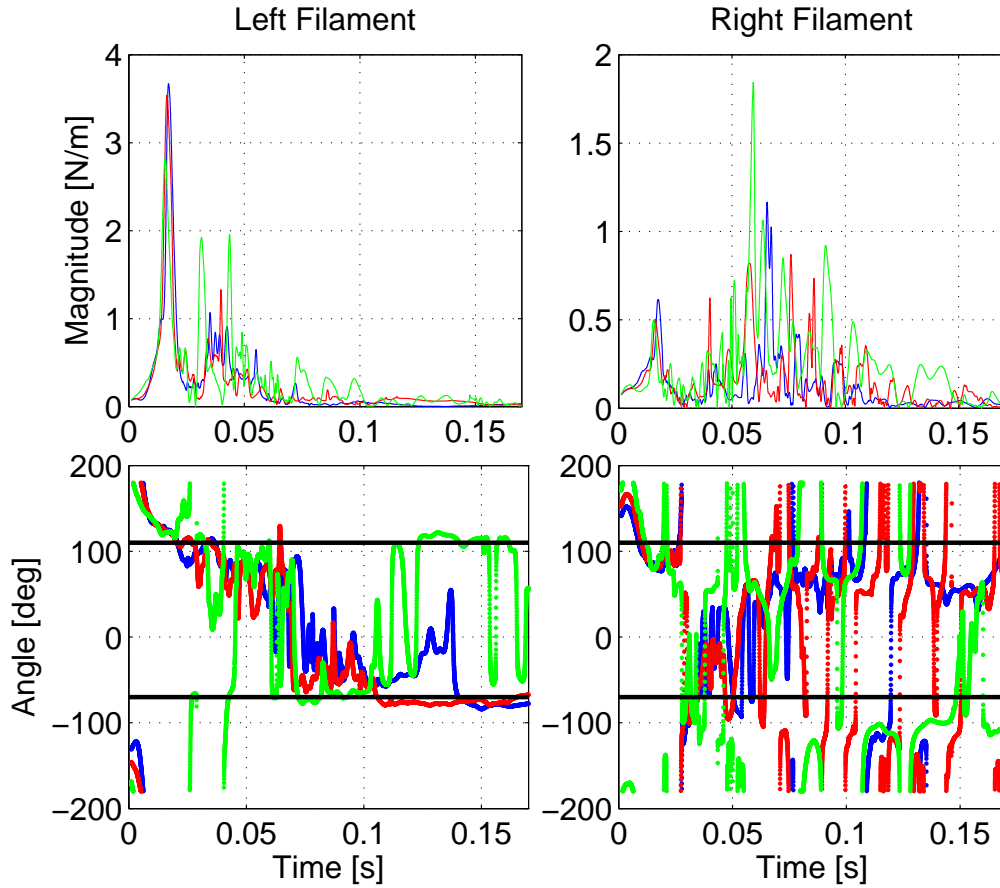


Figure 4.26: Magnitude, per unit depth, of force exerted by the left and right filaments of the plate with a lengths of $L_f = 2\text{mm}$. Each line identify a specific bending stiffness: $K_b = 5.25 \cdot 10^{-11} \text{Pa} \cdot \text{m}^4$ (blue line); $2.62 \cdot 10^{-10} \text{Pa} \cdot \text{m}^4$ (red line); $1.31 \cdot 10^{-9} \text{Pa} \cdot \text{m}^4$ (green line). In the angle amplitude two black lines are added to identify the range where the filament exerts a traction force $[-70^\circ; 110^\circ]$ from the range where it applies a compression force on the plate.

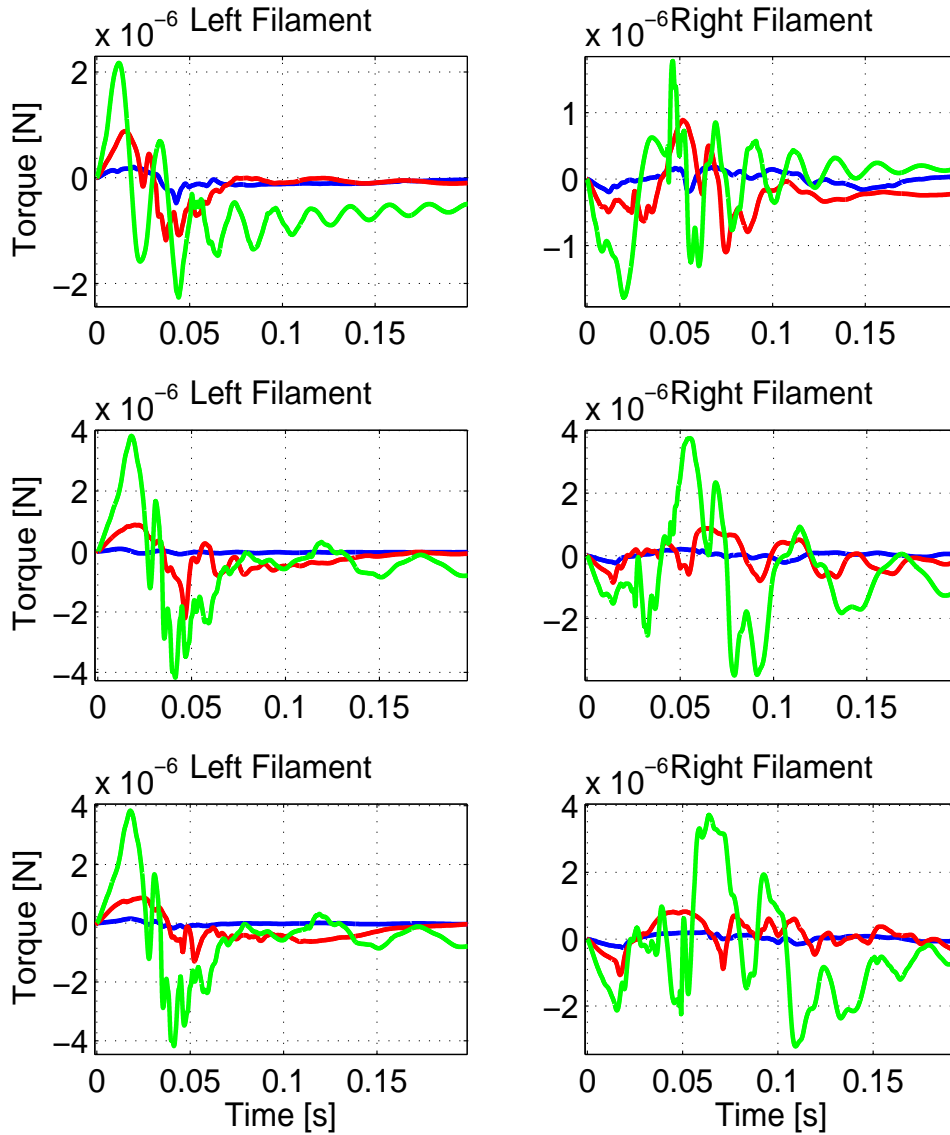


Figure 4.27: Torque, per unit depth, exerted by the left and right filaments of the plate for different lengths. In the first row $L_f = 1.0\text{mm}$; in the second row $L_f = 1.5\text{mm}$; in the third row $L_f = 2.0\text{mm}$. Each line identify a specific bending stiffness: $K_b = 5.25 \cdot 10^{-11} \text{Pa} \cdot \text{m}^4$ (blue line); $2.62 \cdot 10^{-10} \text{Pa} \cdot \text{m}^4$ (red line); $1.31 \cdot 10^{-9} \text{Pa} \cdot \text{m}^4$ (green line). In these figures the positive values of the torque indicates a counterclockwise orientation, while the negative values stand for the counterclockwise orientation.

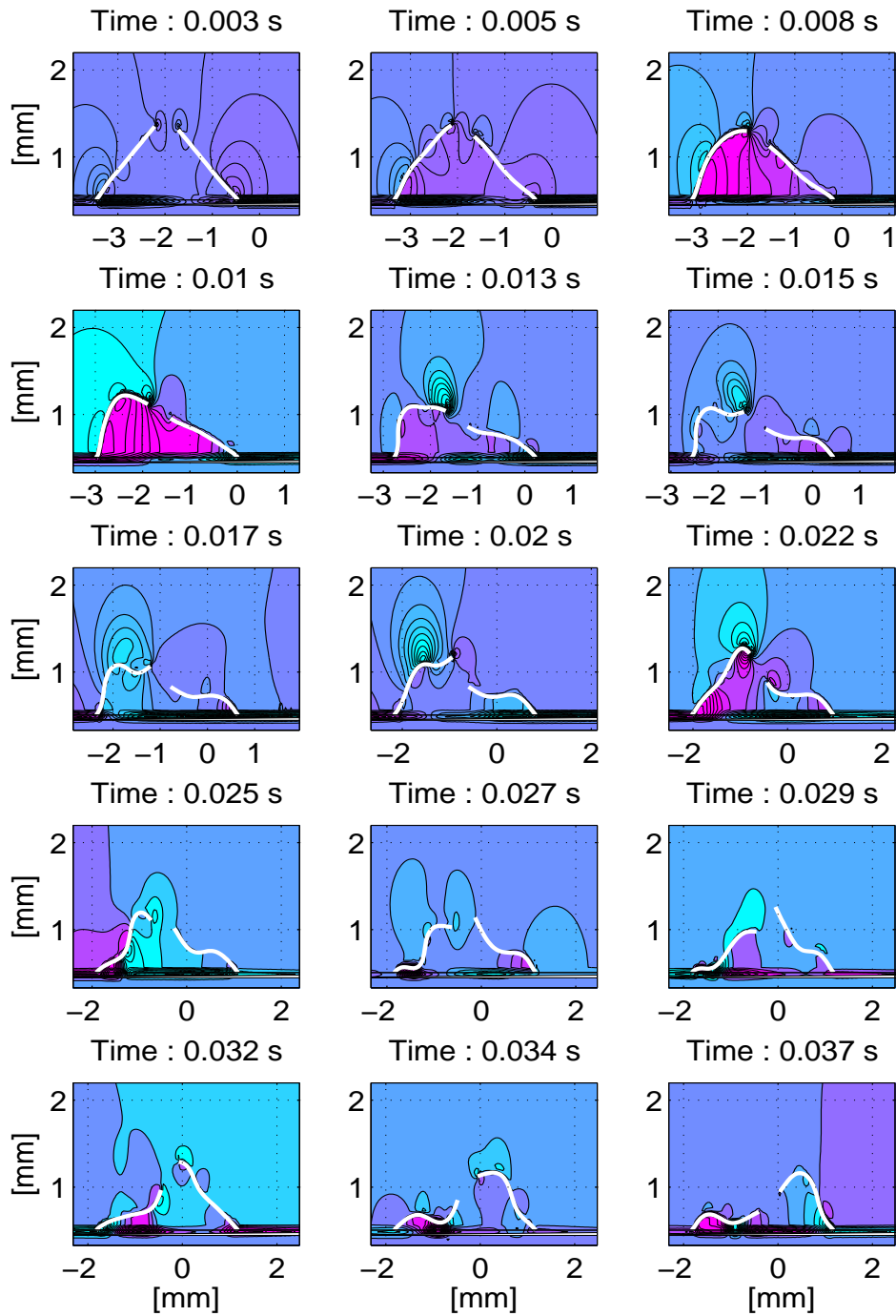


Figure 4.28: Pressure field during a simulation with $L_f = 1.5\text{mm}$ as filaments lengths and bending stiffness of $2.62 \cdot 10^{-10}\text{Pa} \cdot \text{m}^4$. The pressure scale goes from -4.92 Pa (blue color) to 4.92 Pa (magenta color), with intervals of 0.15 Pa . The saccadic movement started at 0 second, the maximum velocity is reached at 0.019 seconds and the movement ends at 0.045 seconds.

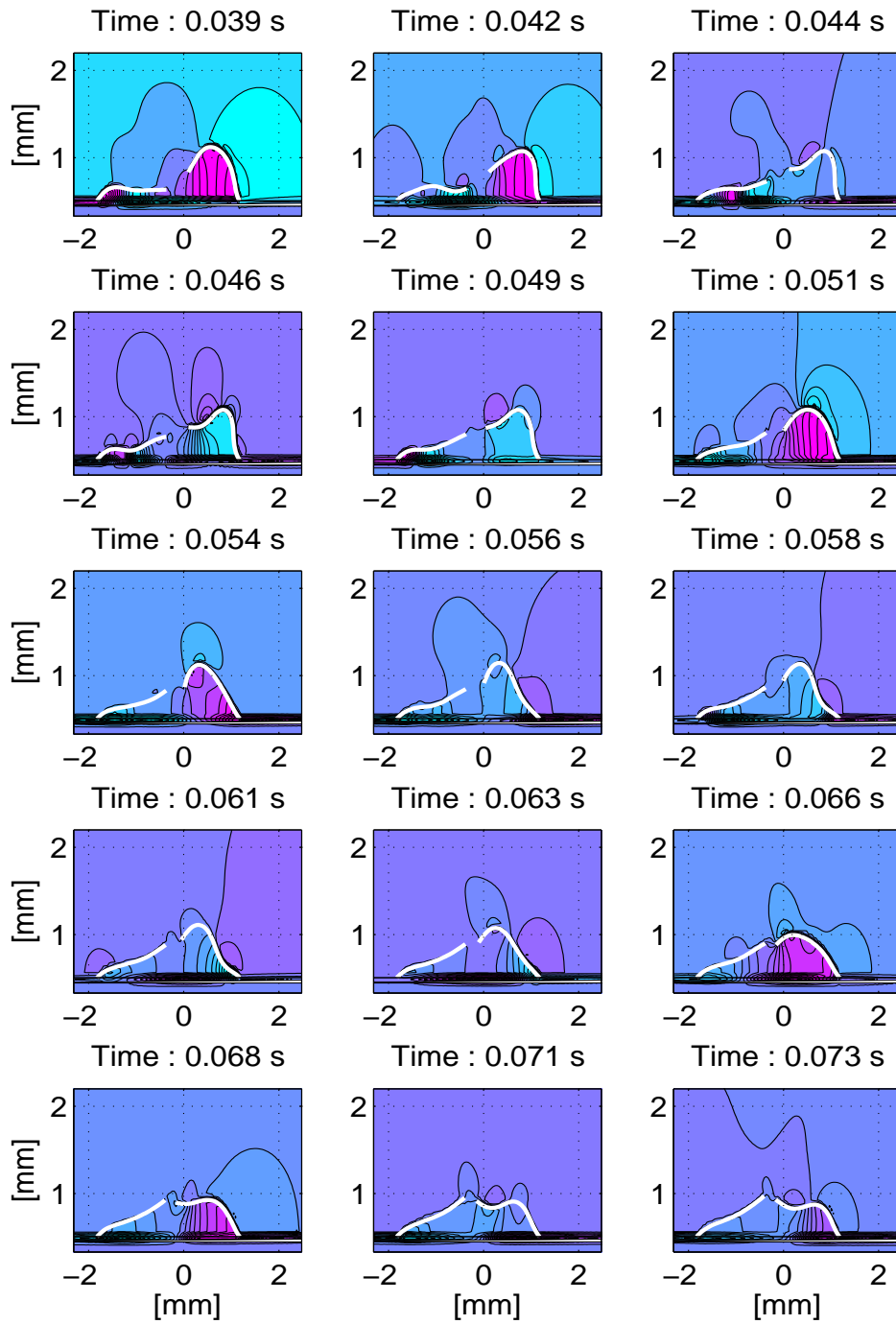


Figure 4.29: Pressure field during a simulation with $L_f = 1.5\text{mm}$ as filaments lengths and bending stiffness of $2.62 \cdot 10^{-10}\text{Pa} \cdot \text{m}^4$. The pressure scale goes from -4.92 Pa (blue color) to 4.92 Pa (magenta color), with intervals of 0.15 Pa . The saccadic movement started at 0 second, the maximum velocity is reached at 0.019 seconds and the movement ends at 0.045 seconds.

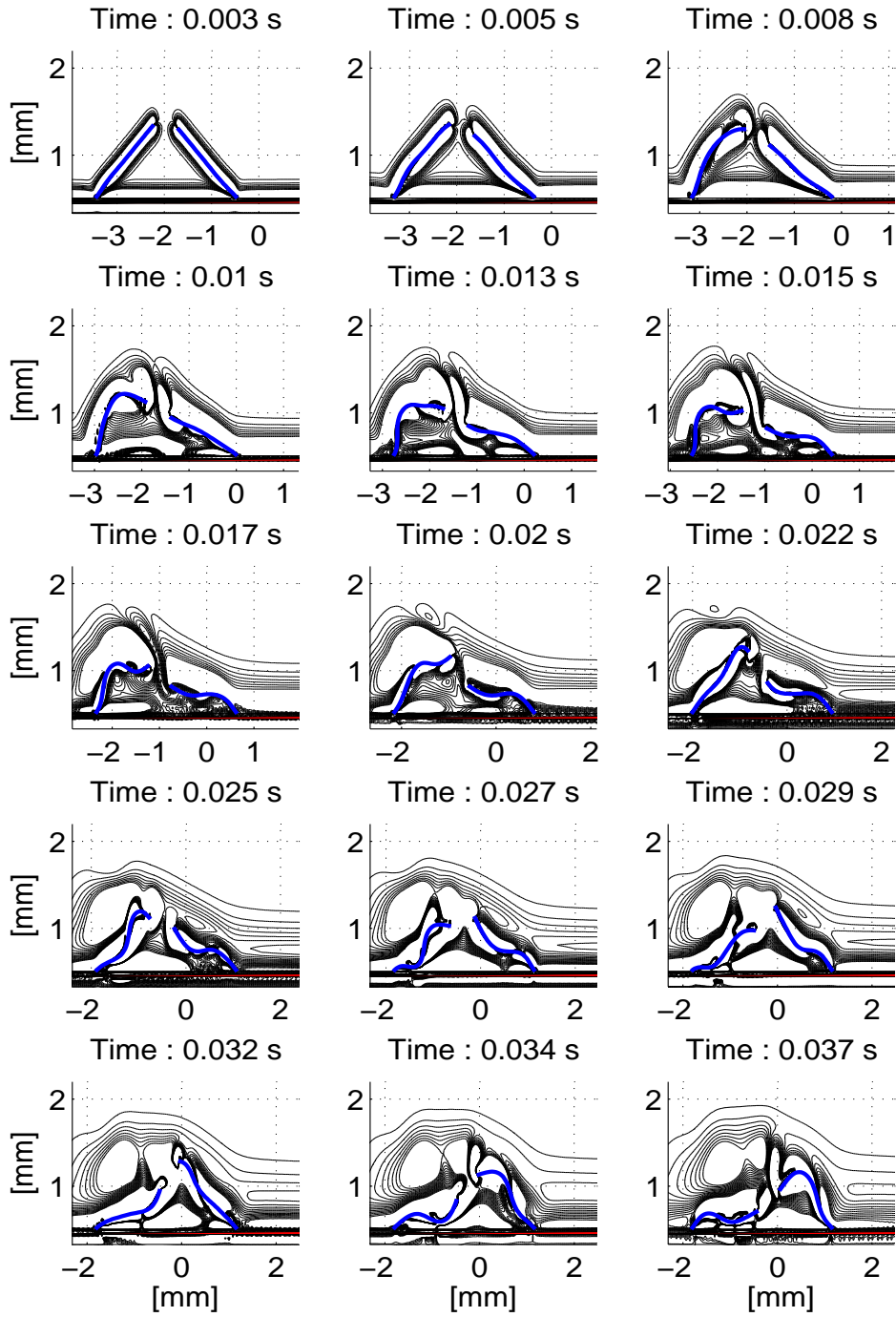


Figure 4.30: Vorticity field during a simulation with $L_f = 1.5\text{mm}$ as filament length and bending stiffness of $2.62 \cdot 10^{-10} \text{Pa} \cdot \text{m}^4$. The saccadic movement started at 0 second, the maximum velocity is reached at 0.019 seconds and the movement ends at 0.045 seconds. From 0.045 seconds till the end of the simulation the velocity of the plate is equal to zero.

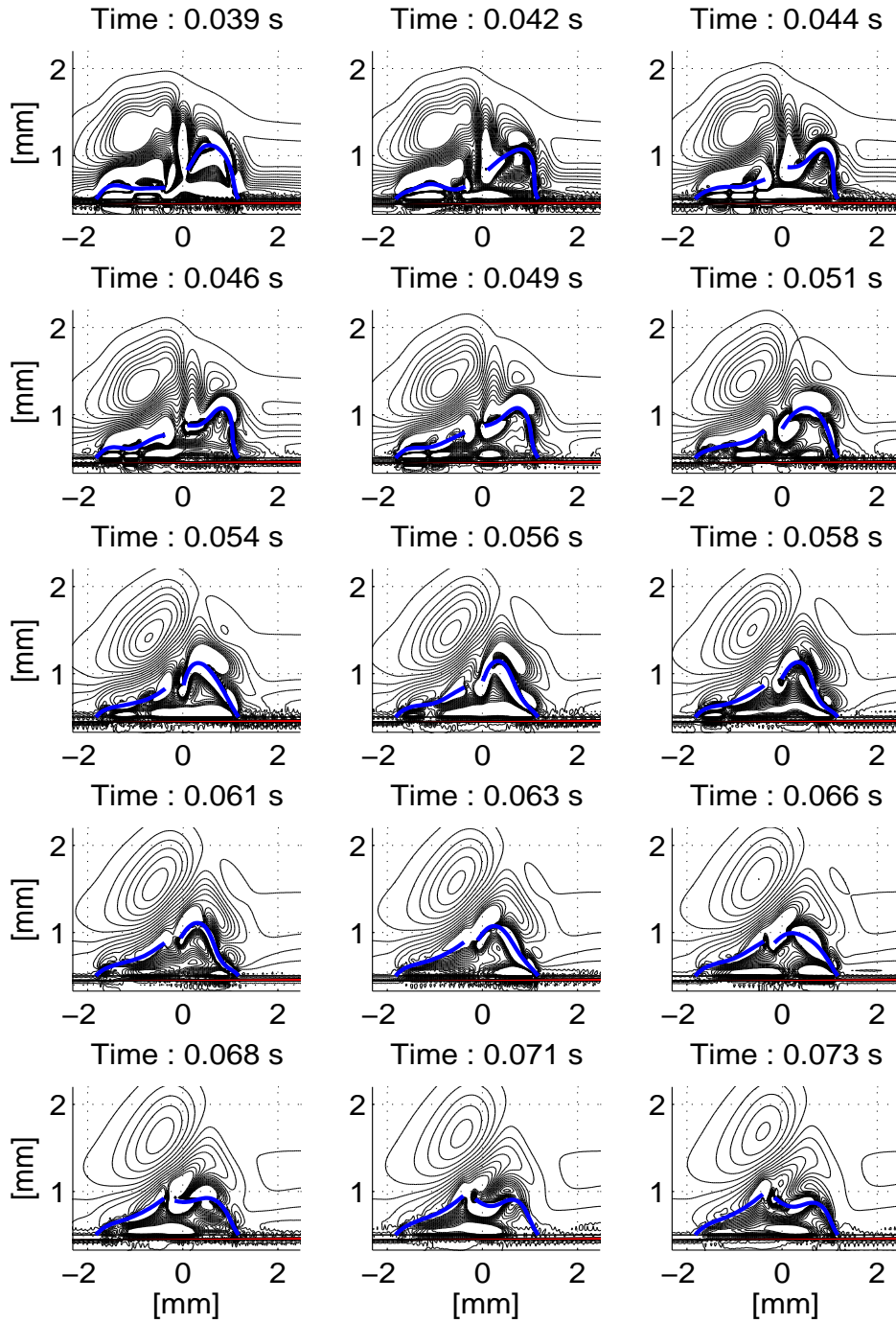


Figure 4.31: Vorticity field during a simulation with $L_f = 1.5\text{mm}$ as filament length and bending stiffness of $2.62 \cdot 10^{-10} \text{Pa} \cdot \text{m}^4$. The saccadic movement started at 0 second, the maximum velocity is reached at 0.019 seconds and the movement ends at 0.045 seconds. From 0.045 seconds till the end of the simulation the velocity of the plate is equal to zero.

Chapter 5

Conclusions and future developments

From the experiments we have performed we can now discuss about the results obtained and compare retinal breaks with retinal detachments.

Analyzing Figures (5.1) (5.2) (5.3) and (5.4) the main features of our simulations are shown. These figures show the maximum peaks of the magnitude of the force along with the time in which the peaks appear for all the bending stiffness and lengths used. In Figures (5.3) and (5.4) the values for both filaments are shown.

Comparing Figures (5.1) and (5.3) we noticed how retinal holes generate in magnitude higher forces on the plate, moreover the oscillations of the filament with a bending stiffness of $1.31 \cdot 10^{-9} Pa \cdot m^4$ (green lines), showed during the simulation of retinal breaks, are balanced by the spring action in case of retinal holes, which prevents a free movement of the filaments.

Studying the dynamics of retinal holes through Figures (5.3) and (5.4) we demonstrated how the left filament is characterized by higher values in compression of the magnitude of force during the accelerated phase of the saccade, which starts at 0 second till 0.019 seconds; while lower traction peaks are defined during the decelerated phase of the saccade, which goes from 0.019 seconds to 0.045 seconds. The right filament behaves differently. The magnitude of force has higher peaks in traction, localized during the relaxation phase of the filament which goes from 0.045 seconds till the end of the simulation. Eventually it is clear how the magnitude of force increases simulating longer filaments.

Observing the forces and the torque in both cases, through Figures (4.16) and (4.18) for the retinal break and Figures (4.24) - (4.26) and (4.27) for the retinal hole, oscillations of the signals are evident. A reason of this behavior can be found analyzing the evolution of pressure signal in a specific point of the Eulerian grid. In Figure (5.5) the pressure values of two Eulerian points, under and over the filament at a position of $0.5 \cdot L_f$ from the attachment point, are saved during the whole simulation of retinal break. It can be noticed how this signal is afflicted by the same of noise we found analyzing the forces. Using the absolute value of the pressure, shown in Figure (5.6), only to simplify a comparison of its behavior with the magnitude of force we noticed how the two types of signals are similar. With these results we see that the main component of the forces are due to the pressure which in the present case oscillates. The same behavior was observed for retinal holes.

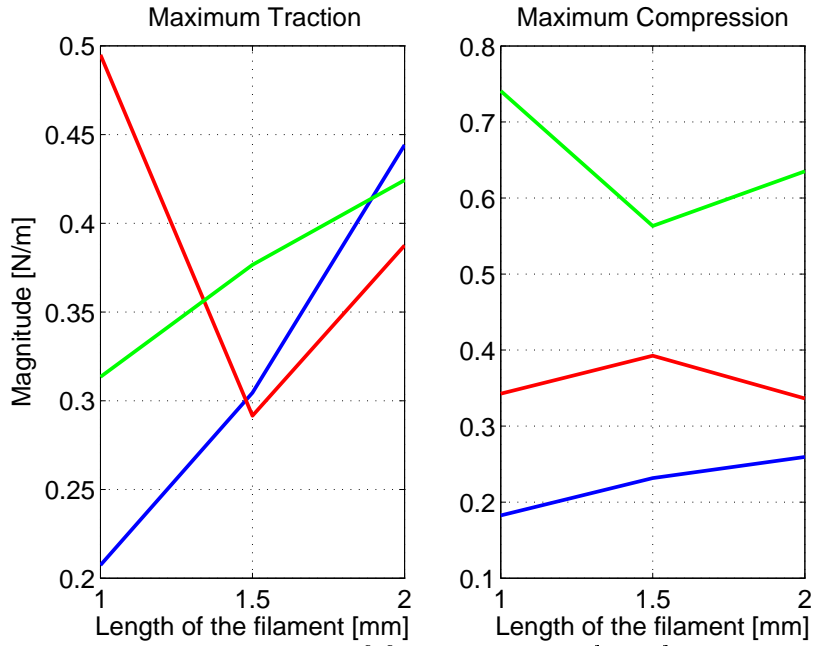


Figure 5.1: Maximum magnitude of force, per unit length, distinguished between traction and compression for retinal break. These results have been obtained for all the lengths used and a bending stiffness of $2.62 \cdot 10^{-10} Pa \cdot m^4$. Each lines identify a specific bending stiffness: $K_b = 5.25 \cdot 10^{-11} Pa \cdot m^4$ (blue line); $2.62 \cdot 10^{-10} Pa \cdot m^4$ (red line); $1.31 \cdot 10^{-9} Pa \cdot m^4$ (green line).

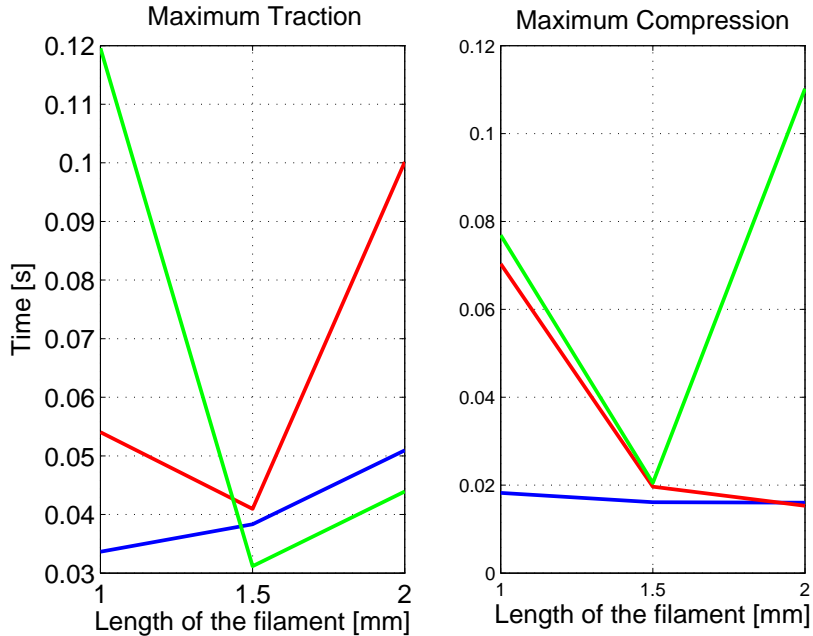


Figure 5.2: Time in which the maximum values shown in Figure (5.1) are defined for retinal break. These results have been obtained for all the lengths used and a bending stiffness of $2.62 \cdot 10^{-10} Pa \cdot m^4$. Each lines identify a specific bending stiffness: $K_b = 5.25 \cdot 10^{-11} Pa \cdot m^4$ (blue line); $2.62 \cdot 10^{-10} Pa \cdot m^4$ (red line); $1.31 \cdot 10^{-9} Pa \cdot m^4$ (green line).

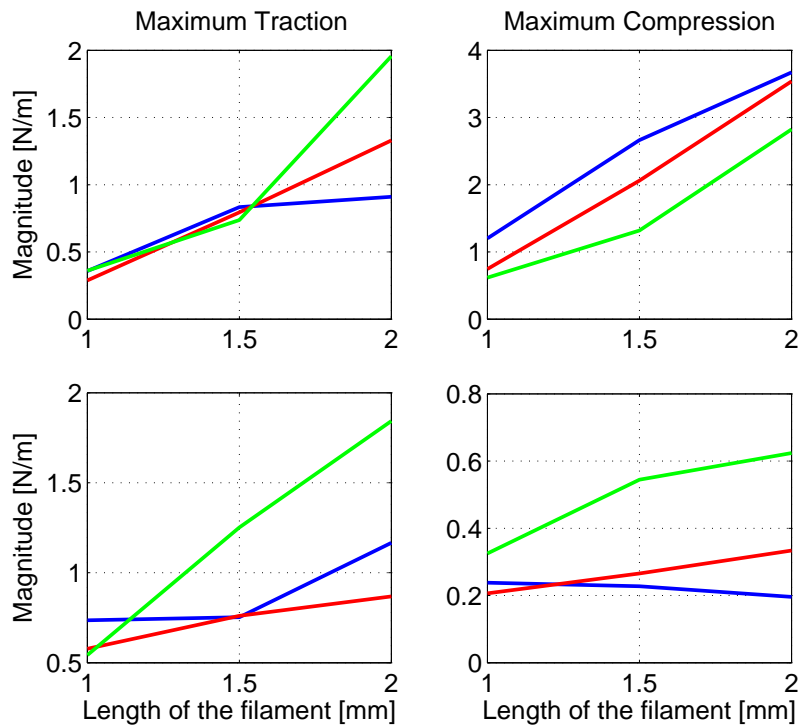


Figure 5.3: Maximum magnitude of force, per unit length, distinguished between traction and compression for retinal hole . These results have been obtained for all the lengths used and a bending stiffness of $2.62 \cdot 10^{-10} Pa \cdot m^4$. The first row represents the left filament, while the second row represent the right filament. Each lines identify a specific bending stiffness: $K_b = 5.25 \cdot 10^{-11} Pa \cdot m^4$ (blue line); $2.62 \cdot 10^{-10} Pa \cdot m^4$ (red line); $1.31 \cdot 10^{-9} Pa \cdot m^4$ (green line).

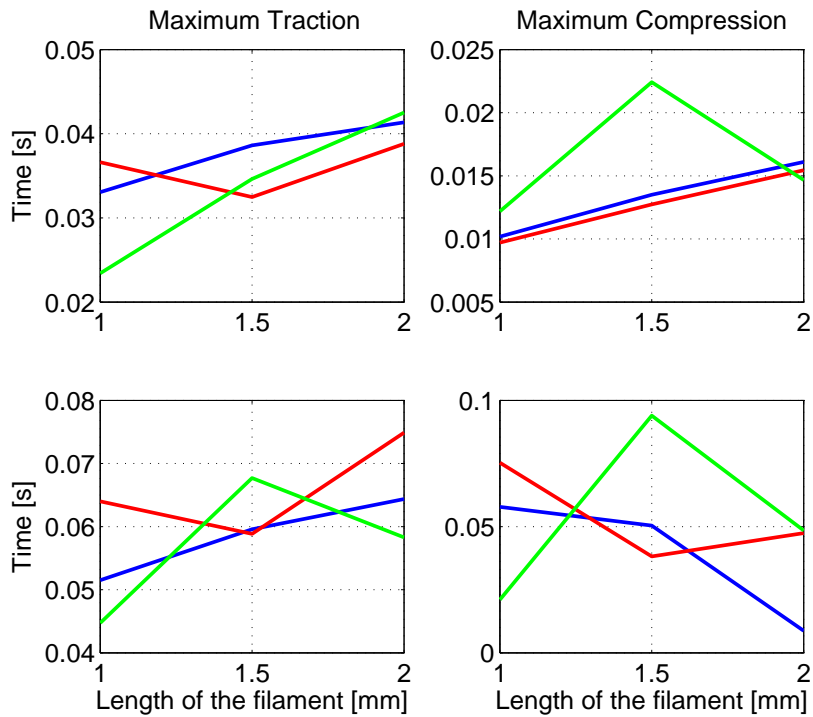


Figure 5.4: Time in which the maximum values shown in Figure (5.3) are defined for retinal hole. These results have been obtained for all the lengths used and a bending stiffness of $2.62 \cdot 10^{-10} Pa \cdot m^4$. The first row represents the left filament, while the second row represent the right filament. Each lines identify a specific bending stiffness: $K_b = 5.25 \cdot 10^{-11} Pa \cdot m^4$ (blue line); $2.62 \cdot 10^{-10} Pa \cdot m^4$ (red line); $1.31 \cdot 10^{-9} Pa \cdot m^4$ (green line).

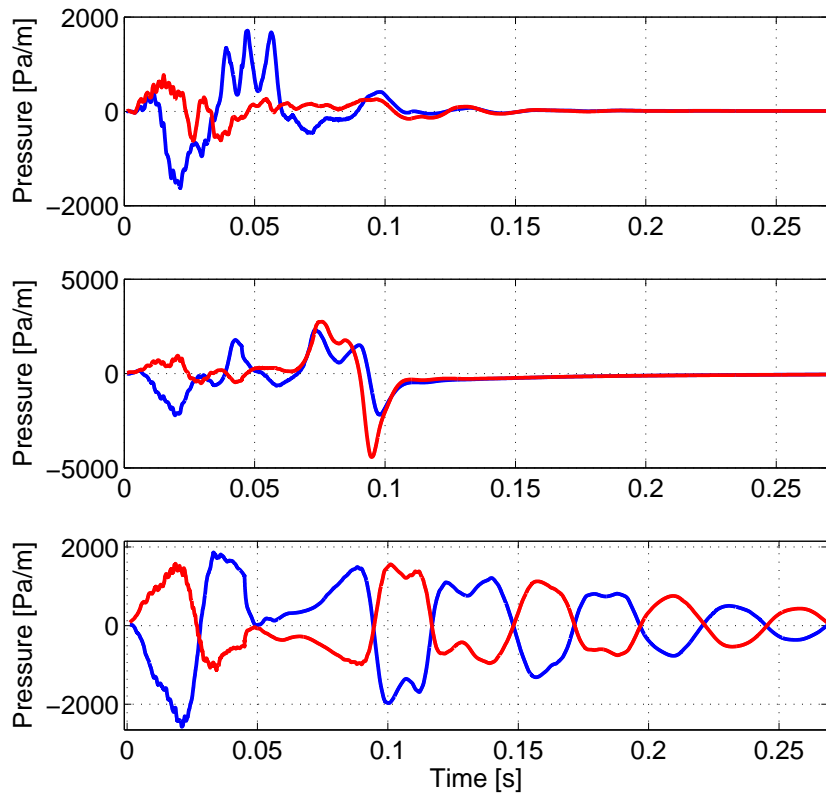


Figure 5.5: Pressure signal calculated for the retinal break in two Eulerian points: one under the filament (red line) and one over the filament (blue line). The length of the filament used was $L_f = 1.5\text{mm}$. The three rows identify the three bending stiffness: $K_b = 5.25 \cdot 10^{-11} \text{Pa} \cdot \text{m}^4$ (first row); $2.62 \cdot 10^{-10} \text{Pa} \cdot \text{m}^4$ (second row) and $1.31 \cdot 10^{-9} \text{Pa} \cdot \text{m}^4$ (third row).

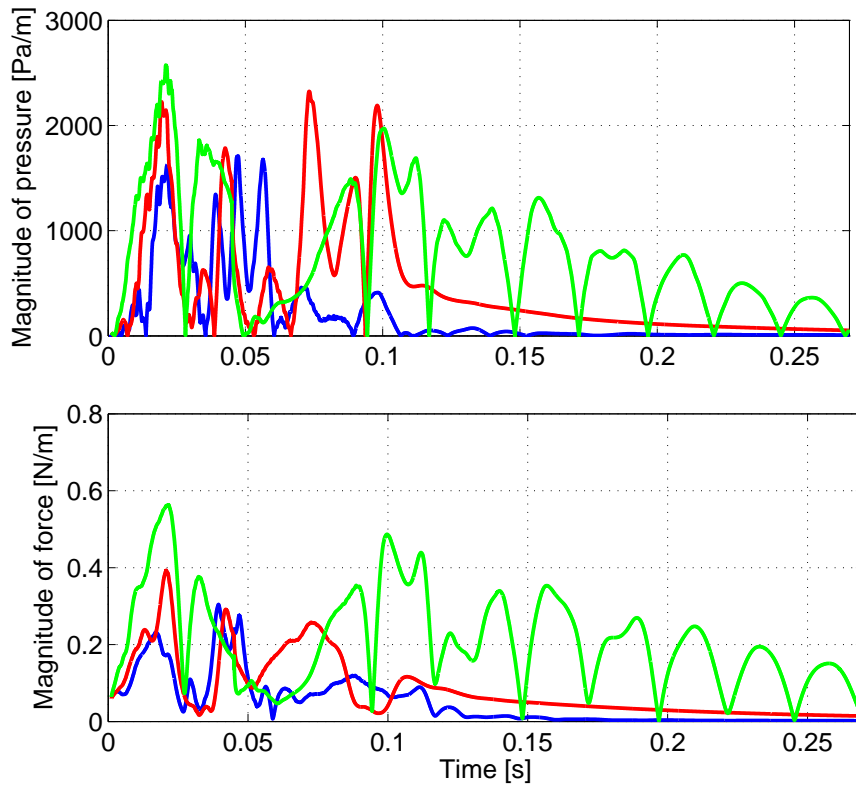


Figure 5.6: Comparison between the absolute value of the pressure (evaluated in the same points of Figure (5.5)) with the magnitude of force vector for the retinal break. The length of the filament used was $L_f = 1.5\text{mm}$. The three lines identify the three bending stiffness: $K_b = 5.25 \cdot 10^{-11} Pa \cdot m^4$ (blue line); $2.62 \cdot 10^{-10} Pa \cdot m^4$ (red line) and $1.31 \cdot 10^{-9} Pa \cdot m^4$ (green line).

This work has shown how the retinal holes produce higher traction forces on the attached retina, which means that the presence of a retinal hole might promote a further separation of the neurosensory retina from the underlying retinal pigment epithelium.

Our study was a first step to simulate the retinal detachment, and further analysis can be made for different cases by exploring other conditions, such as the movement of the plate, the filaments, the fluid and the geometry considered.

During the simulations only small saccadic amplitudes were tested, and it is of interest to consider different amplitudes of saccadic movements and Rapid Eye Movements in order to evaluate their influence during the detachment process.

In the literature we found different values for the Young modulus of the retina, leading to different bending stiffness. A specific analysis of the mechanical properties of the retina can be applied to define the most reasonable values of this tissue to simulate.

In our virtual experiments we fixed a certain starting position of the filament, and it would be of interest to perform further studies with different filament orientations and shapes in order to determine which case can promote retinal detachment involving higher forces on the attached point.

It is also of interest to modify the model in order to simulate the development of detachment during saccadic eye movements. For this purpose a future goal is to include the Winkler foundation theory at the model, which allows to use a time law that defines the evolution of the detached retina.

In order to allow a wider range of parameters, such as bending stiffness and filament length, it would be useful to include a model which accounts for collisions.

During our tests we simplified the surrounding fluid as Newtonian. Since the vitreous humour is a visco-elastic gel, it will be interesting to compare our results with the values obtained simulating a visco-elastic fluid.

Eventually an improvement of the geometry used can be accomplished by replacing the moving plate with a cylinder, oscillating around its axis of symmetry, or a moving sphere.

Chapter 6

Acknowledgments

First of all I would like to thank Professor Jan Pralits and Professor Rodolfo Repetto for giving me the opportunity to collaborate with the Royal Institute of Technology of Stockholm. They showed patience during my work and their continuous support sustained me during the thesis.

I would also like to express my gratitude to Professor Shervin Bagheri for all the time he dedicated to me since he first introduced me the Immersed Boundary Method and the numerical aspect of the project.

I thank Damiano Natali for his valuable advices and the willingness he always showed to me.

With this thesis my path as a student of Biomedical Engineering at the University of Genoa has its conclusion, thus I would like to thank all the fellow students who shared with me this experience, especially Giorgio and Giulia who always cheered me during hard times, Paco for his five-days-of-studies before any exams and Bibi for his precious advices regarding new interesting songs. A special thanks goes to Nose who entertained me with his songs, I'm looking forward to buy your first album.

I would like to thank my flatmates who saw my dark side during finals, especially the Bacci brothers, Sasha, Gian and Laura (yes, I missed you). May the lords of the subsoil guide you and the power of the sweet dreams pasta assists you. I would also like to thank Michela for her midnight coffee and her green tea yogurt.

A special thanks goes also to Anne, even if she thought each time I made a mistake an eye exploded she shared her flat with me. The time we spent together was really great and your music is wonderful too.

Finally I am very thankful to my family who supported me in different ways during these years.

List of Figures

1.1	Vertical sagittal section of human eye.	8
1.2	Posteriorly directed fluid flow through the vitreous into the subretinal space in an eye with rhegmatogenous retinal detachment.	10
1.3	Irregular posterior extensions of the vitreous due to horseshoe-shaped retinal tears (A) and retinal hole with a free operculum (B).	10
1.4	Retinal tear with an encircling buckle.	11
1.5	Imaginary clock-hour map drawn on the optic nerve.	13
1.6	Summary of pneumatic retinopexy. A, the volume of the subretinal fluid is determined by inflow of fluid vitreous (green arrow) and the outflow through the retinal pigment epithelial pump into the choroid (red arrow). B, the area of the retinal break is treated with multiple contiguous applications of transconjunctival cryotherapy. C, injection of the gas bubble through the needle. D, the head is positioned so that the intravitreal gas bubble closes the retinal break. E, with the beak closed, the retina usually reattached by the first postoperative day. F, the gas bubble is spontaneously absorbed.	14
2.1	Example of saccadic eye movement, at different amplitudes, used by Repetto <i>et al.</i> [5]. (a) Angular displacement $\theta(t)$; (b) angular velocity $\Omega(t) = d\theta/dt$	18
3.1	An example of the geometry used in two dimensions. Figure (a) represents a rigid plate with one filament, which simulates the retinal break. In Figure (b) two filaments are used for the retinal hole. In this case a fictitious spring, working only in traction, is added between them to create a connection which resembles the original case in three dimensions.	21
3.2	Example of a generic immersed body, defined by the domain Γ and the function $\mathbf{X}(s,t)$, immersed in a full-filled region Ω	23
3.3	The immersed body used in this work, defined by the Lagrangian points $\mathbf{X}(s,t)$. The edges of the computational box Ω are placed at a certain distance from the domain Γ such that the boundaries won't affect the movement of the body. The black lines represent the Eulerian stretched grid.	23
3.4	Dirichlet and Neumann boundary conditions: the velocity and its derivative at the edges of the box are equal to zero; the dashed line is the computational domain while the red line is the plate.	27

3.5	Clamped condition at the fixed end of the filament. The red dots represents the Lagrangian points of the plate, while the blue dots are the Lagrangian points of the filament.	28
3.6	Periodic boundary conditions: the velocity	29
3.7	Colocated grid. The horizontal and vertical velocities are computed in the middle of each mesh with \rightarrow and \uparrow respectively, as for the pressures at each \bullet	36
3.8	Staggered grid. The horizontal and vertical velocities are delineated with \rightarrow and \uparrow respectively at the edges of each mesh, while the pressures are computed in every \circ at each center.	37
3.9	A cell of the staggered grid.	37
4.1	Mean absolute error of the numerical solution of the second Stokes' problem for different minimum grid spacing.	39
4.2	Magnification of the mean absolute error showed in Figure (4.1).	40
4.3	Position assumed by the end x -coordinate of the filament for different dimensions of the domain, from the smallest Box 1 (green line) to the biggest Box 4 (red line).	41
4.4	Detail of Figure (4.3).	41
4.5	Position assumed by the end x -coordinate of the filament for different dimensions of the domain, where the notation $1.5 \cdot W$ and $2 \cdot W$ denotes a box width equal to 1.5 and 2 times the width of First Box, while with $1.5 \cdot H$ and $2 \cdot H$ the height of the box has been increased 1.5 and 2 times the height of First Box. Eventually the notation $2 \cdot H \& 2 \cdot W$ denotes a domain with twice the size of First Box.	43
4.6	Detail of Figure (4.5).	44
4.7	Saccadic velocity profiles used in our simulations for different amplitudes. After the saccadic movement the simulation continued at angular velocity equal to zero to evaluate the relaxation movement of the filament.	45
4.8	Position of the x coordinate of the end point in respect to the first fixed point.	47
4.9	Position of the y coordinate of the end point in respect to the first fixed point.	47
4.10	An example of the force, per unit depth, exerted on the plate which affected by noise due to the action of the springs connecting the Lagrangian points. In this case the horizontal force is shown for a filament with length $L_f = 1.5\text{mm}$	48
4.11	Movement of the filament during the simulation after the saccade movement. The first column is referred at the filament with length $L_f = 1.5\text{mm}$; the second column is with $L_f = 3\text{mm}$; while the third column shows the movement for $L_f = 4.5\text{mm}$. The saccadic movement started at 0 second and ended at 0.08 seconds, from 0.08 seconds till the end of the simulation the velocity of the plate was equal to zero.	49

4.12	Movement of the left filament, first column, and the right filament, right column, during the simulation. The position along the x axis and y axis are show for all the lengths used: $L_f = 4.5\text{mm}$ (green line); $L_f = 3\text{mm}$ (red line) and $L_f = 1.5\text{mm}$ (blue line).	51
4.13	An example of the force, per unit depth, exerted on the plate which is afflicted by a noise due to the action of the springs among the Lagrangian points. In this case the horizontal and vertical forces are shown for the left filament with length $L_f = 1.5\text{mm}$	51
4.14	Movement of the two filaments during the simulation. The first column is referred at the filament with length $L_f = 1.5\text{mm}$; the second column is with $L_f = 3\text{mm}$; while the third column shows the movement for $L_f = 4.5\text{mm}$. The saccadic movement started at 0 second and ended at 0.08 seconds, from 0.08 seconds till the end of the simulation the velocity of the plate was equal to zero.	52
4.15	Movement of the filament, with a bending stiffness of $2.62 \cdot 10^{-10} Pa \cdot m^4$, during the simulation. The first column is referred at the filament with length $L_f = 1.0\text{mm}$, while the second column shows the movement for $L_f = 1.5\text{mm}$ and the last column is for $L_f = 2.0\text{mm}$.The saccadic movement started at 0 second, the maximum velocity is reached at 0.019 seconds and the movement ends at 0.045 seconds. From 0.045 seconds till the end of the simulation the velocity of the plate is equal to zero.	55
4.16	Magnitude of force, per unit depth, exerted by the filament of the plate for different lengths L_f . Each line identify a specific bending stiffness: $K_b = 5.25 \cdot 10^{-11} Pa \cdot m^4$ (blue line); $2.62 \cdot 10^{-10} Pa \cdot m^4$ (red line); $1.31 \cdot 10^{-9} Pa \cdot m^4$ (green line). In the angle amplitude two black lines are added to identify the range where the filament exerts a traction force $[-70^\circ; 110^\circ]$ from the range where it applies a compression force on the plate.	56
4.17	Torque, per unit depth, exerted by the filament on the plate for different lengths L_f . Each lines identify a specific bending stiffness: $K_b = 5.25 \cdot 10^{-11} Pa \cdot m^4$ (blue line); $2.62 \cdot 10^{-10} Pa \cdot m^4$ (red line); $1.31 \cdot 10^{-9} Pa \cdot m^4$ (green line). In these figures the positive values of the torque indicates a counterclockwise orientation, while the negative values stand for the counterclockwise orientation.	57
4.18	Torque, per unit depth, exerted by the filament on the plate for different lengths L_f . In this figure the bending stiffness is fixed at the value of $2.62 \cdot 10^{-10} Pa \cdot m^4$. The positive values of the torque indicates a counterclockwise orientation, while the negative values stand for the counterclockwise orientation.	58

4.19	Pressure field during a simulation with $L_f = 1.5\text{mm}$ as filament length and bending stiffness of $2.62 \cdot 10^{-10} Pa \cdot m^4$. The pressure scale goes from $-3.28 Pa$ (blue color) to $3.28 Pa$ (magenta color), with intervals of $0.01 Pa$. The saccadic movement started at 0 second, the maximum velocity is reached at 0.019 seconds and the movement ends at 0.045 seconds. From 0.045 seconds till the end of the simulation the velocity of the plate is equal to zero.	59
4.20	Pressure field during a simulation with $L_f = 1.5\text{mm}$ as filament length and bending stiffness of $2.62 \cdot 10^{-10} Pa \cdot m^4$. The pressure scale goes from $-3.28 Pa$ (blue color) to $3.28 Pa$ (magenta color), with intervals of $0.01 Pa$. The saccadic movement started at 0 second, the maximum velocity is reached at 0.019 seconds and the movement ends at 0.045 seconds. From 0.045 seconds till the end of the simulation the velocity of the plate is equal to zero.	60
4.21	Vorticity field during a simulation with $L_f = 1.5\text{mm}$ as filament length and bending stiffness of $2.62 \cdot 10^{-10} Pa \cdot m^4$. The saccadic movement started at 0 second, the maximum velocity is reached at 0.019 seconds and the movement ends at 0.045 seconds. From 0.045 seconds till the end of the simulation the velocity of the plate is equal to zero.	61
4.22	Vorticity field during a simulation with $L_f = 1.5\text{mm}$ as filament length and bending stiffness of $2.62 \cdot 10^{-10} Pa \cdot m^4$. The saccadic movement started at 0 second, the maximum velocity is reached at 0.019 seconds and the movement ends at 0.045 seconds. From 0.045 seconds till the end of the simulation the velocity of the plate is equal to zero.	62
4.23	Movement of the filaments, with a bending stiffness of $2.62 \cdot 10^{-10} Pa \cdot m^4$, during the simulation. The first column is referred at the filament with length $L_f = 1.0\text{mm}$, while the second column shows the movement for $L_f = 1.5\text{mm}$ and the last column is for $L_f = 2.0\text{mm}$. The saccadic movement started at 0 second, the maximum velocity is reached at 0.019 seconds and the movement ends at 0.045 seconds. From 0.045 seconds till the end of the simulation the velocity of the plate is equal to zero.	65
4.24	Magnitude, per unit depth, of force exerted by the left and right filaments of the plate with a lengths of $L_f = 1\text{mm}$. Each line identify a specific bending stiffness: $K_b = 5.25 \cdot 10^{-11} Pa \cdot m^4$ (blue line); $2.62 \cdot 10^{-10} Pa \cdot m^4$ (red line); $1.31 \cdot 10^{-9} Pa \cdot m^4$ (green line). In the angle amplitude two black lines are added to identify the range where the filament exerts a traction force $[-70^\circ; 110^\circ]$ from the range where it applies a compression force on the plate.	66
4.25	Magnitude, per unit depth, of force exerted by the left and right filaments of the plate with a lengths of $L_f = 1.5\text{mm}$. Each line identify a specific bending stiffness: $K_b = 5.25 \cdot 10^{-11} Pa \cdot m^4$ (blue line); $2.62 \cdot 10^{-10} Pa \cdot m^4$ (red line); $1.31 \cdot 10^{-9} Pa \cdot m^4$ (green line). In the angle amplitude two black lines are added to identify the range where the filament exerts a traction force $[-70^\circ; 110^\circ]$ from the range where it applies a compression force on the plate.	67

4.26	Magnitude, per unit depth, of force exerted by the left and right filaments of the plate with a lengths of $L_f = 2\text{mm}$. Each line identify a specific bending stiffness: $K_b = 5.25 \cdot 10^{-11} Pa \cdot m^4$ (blue line); $2.62 \cdot 10^{-10} Pa \cdot m^4$ (red line); $1.31 \cdot 10^{-9} Pa \cdot m^4$ (green line). In the angle amplitude two black lines are added to identify the range where the filament exerts a traction force $[-70^\circ; 110^\circ]$ from the range where it applies a compression force on the plate.	68
4.27	Torque, per unit depth, exerted by the left and right filaments of the plate for different lengths. In the first row $L_f = 1.0\text{mm}$; in the second row $L_f = 1.5\text{mm}$; in the third row $L_f = 2.0\text{mm}$. Each line identify a specific bending stiffness: $K_b = 5.25 \cdot 10^{-11} Pa \cdot m^4$ (blue line); $2.62 \cdot 10^{-10} Pa \cdot m^4$ (red line); $1.31 \cdot 10^{-9} Pa \cdot m^4$ (green line). In these figures the positive values of the torque indicates a counterclockwise orientation, while the negative values stand for the counterclockwise orientation.	69
4.28	Pressure field during a simulation with $L_f = 1.5\text{mm}$ as filaments lengths and bending stiffness of $2.62 \cdot 10^{-10} Pa \cdot m^4$. The pressure scale goes from -4.92 Pa (blue color) to 4.92 Pa (magenta color), with intervals of 0.15 Pa. The saccadic movement started at 0 second, the maximum velocity is reached at 0.019 seconds and the movement ends at 0.045 seconds.	70
4.29	Pressure field during a simulation with $L_f = 1.5\text{mm}$ as filaments lengths and bending stiffness of $2.62 \cdot 10^{-10} Pa \cdot m^4$. The pressure scale goes from -4.92 Pa (blue color) to 4.92 Pa (magenta color), with intervals of 0.15 Pa. The saccadic movement started at 0 second, the maximum velocity is reached at 0.019 seconds and the movement ends at 0.045 seconds.	71
4.30	Vorticity field during a simulation with $L_f = 1.5\text{mm}$ as filament length and bending stiffness of $2.62 \cdot 10^{-10} Pa \cdot m^4$. The saccadic movement started at 0 second, the maximum velocity is reached at 0.019 seconds and the movement ends at 0.045 seconds. From 0.045 seconds till the end of the simulation the velocity of the plate is equal to zero.	72
4.31	Vorticity field during a simulation with $L_f = 1.5\text{mm}$ as filament length and bending stiffness of $2.62 \cdot 10^{-10} Pa \cdot m^4$. The saccadic movement started at 0 second, the maximum velocity is reached at 0.019 seconds and the movement ends at 0.045 seconds. From 0.045 seconds till the end of the simulation the velocity of the plate is equal to zero.	73
5.1	Maximum magnitude of force, per unit length, distinguished between traction and compression for retinal break. These results have been obtained for all the lengths used and a bending stiffness of $2.62 \cdot 10^{-10} Pa \cdot m^4$. Each lines identify a specific bending stiffness: $K_b = 5.25 \cdot 10^{-11} Pa \cdot m^4$ (blue line); $2.62 \cdot 10^{-10} Pa \cdot m^4$ (red line); $1.31 \cdot 10^{-9} Pa \cdot m^4$ (green line).	75

5.2	Time in which the maximum values shown in Figure (5.1) are defined for retinal break. These results have been obtained for all the lengths used and a bending stiffness of $2.62 \cdot 10^{-10} Pa \cdot m^4$. Each lines identify a specific bending stiffness: $K_b = 5.25 \cdot 10^{-11} Pa \cdot m^4$ (blue line); $2.62 \cdot 10^{-10} Pa \cdot m^4$ (red line); $1.31 \cdot 10^{-9} Pa \cdot m^4$ (green line).	75
5.3	Maximum magnitude of force, per unit length, distinguished between traction and compression for retinal hole . These results have been obtained for all the lengths used and a bending stiffness of $2.62 \cdot 10^{-10} Pa \cdot m^4$. The first row represents the left filament, while the second row represent the right filament. Each lines identify a specific bending stiffness: $K_b = 5.25 \cdot 10^{-11} Pa \cdot m^4$ (blue line); $2.62 \cdot 10^{-10} Pa \cdot m^4$ (red line); $1.31 \cdot 10^{-9} Pa \cdot m^4$ (green line).	76
5.4	Time in which the maximum values shown in Figure (5.3) are defined for retinal hole. These results have been obtained for all the lengths used and a bending stiffness of $2.62 \cdot 10^{-10} Pa \cdot m^4$. The first row represents the left filament, while the second row represent the right filament. Each lines identify a specific bending stiffness: $K_b = 5.25 \cdot 10^{-11} Pa \cdot m^4$ (blue line); $2.62 \cdot 10^{-10} Pa \cdot m^4$ (red line); $1.31 \cdot 10^{-9} Pa \cdot m^4$ (green line).	77
5.5	Pressure signal calculated for the retinal break in two Eulerian points: one under the filament (red line) and one over the filament (blue line). The length of the filament used was $L_f = 1.5\text{mm}$. The three row identify the three bending stiffness: $K_b = 5.25 \cdot 10^{-11} Pa \cdot m^4$ (first row); $2.62 \cdot 10^{-10} Pa \cdot m^4$ (second row) and $1.31 \cdot 10^{-9} Pa \cdot m^4$ (third row).	78
5.6	Comparison between the absolute value of the pressure (evaluated in the same points of Figure (5.5)) with the magnitude of force vector for the retinal break. The length of the filament used was $L_f = 1.5\text{mm}$. The three lines identify the three bending stiffness: $K_b = 5.25 \cdot 10^{-11} Pa \cdot m^4$ (blue line); $2.62 \cdot 10^{-10} Pa \cdot m^4$ (red line) and $1.31 \cdot 10^{-9} Pa \cdot m^4$ (green line).	79

List of Tables

4.1	List of the physical parameters used during our simulations.	44
4.2	List of the numerical parameters used to simulate the filaments with the Newren and Huang models.	45

Bibliography

- [1] Michael F Marmor. Mechanisms of retinal adhesion. *Progress in retinal research*, 12:179–204, 1993.
- [2] Becker W. *The Neurobiology of saccadic eye movements*. ed R H Wurtz and M E Goldberg (Amsterdam: Elsevier Publisher BV-Biomedical Division), 1989.
- [3] Tim David, Steve Smye, Tim Dabbs, and Teifi James. A model for the fluid motion of vitreous humour of the human eye during saccadic movement. *Physics in medicine and biology*, 43(6):1385, 1998.
- [4] Weber R B and Daroff R B. *Vision Res.* (in Adler’s Physiology of the Eye 7th edn, ed W M J Hart (St Louis, MI: Mosby)), 1972.
- [5] Rodolfo Repetto, Alessandro Stocchino, and Chiara Cafferata. Experimental investigation of vitreous humour motion within a human eye model. *Physics in medicine and biology*, 50(19):4729, 2005.
- [6] S Clemens, P Kroll, E Stein, W Wagner, and P Wriggers. Experimental studies on the disappearance of subretinal fluid after episcleral buckling procedures without drainage. *Graefe’s archive for clinical and experimental ophthalmology*, 225(1):16–18, 1987.
- [7] William Joseph Foster, Nadia Dowla, Saurabh Y Joshi, and Michael Nikolaou. The fluid mechanics of scleral buckling surgery for the repair of retinal detachment. *Graefe’s Archive for Clinical and Experimental Ophthalmology*, 248(1):31–36, 2010.
- [8] William J Foster. Bilateral patching in retinal detachment: fluid mechanics and retinal settling. *Investigative ophthalmology and visual science*, 52(8):5437–5440, 2011.
- [9] R Repetto, I Ghigo, G Seminara, and C Ciurlo. A simple hydro-elastic model of the dynamics of a vitreous membrane. *Journal of Fluid Mechanics*, 503:1–14, 2004.
- [10] R Repetto, A Tatone, A Testa, and E Colangeli. Traction on the retina induced by saccadic eye movements in the presence of posterior vitreous detachment. *Biomechanics and modeling in mechanobiology*, 10(2):191–202, 2011.
- [11] Charles S Peskin. The immersed boundary method. *Acta numerica*, 11, 2002.

- [12] Elijah P Newren, Aaron L Fogelson, Robert D Guy, and Robert M Kirby. A comparison of implicit solvers for the immersed boundary equations. *Computer Methods in Applied Mechanics and Engineering*, 197(25):2290–2304, 2008.
- [13] Wei-Xi Huang, Soo Jai Shin, and Hyung Jin Sung. Simulation of flexible filaments in a uniform flow by the immersed boundary method. *Journal of computational physics*, 226(2):2206–2228, 2007.
- [14] Charles S Peskin. Flow patterns around heart valves: a numerical method. *Journal of computational physics*, 10(2):252–271, 1972.
- [15] Luoding Zhu and Charles S Peskin. Simulation of a flapping flexible filament in a flowing soap film by the immersed boundary method. *Journal of Computational Physics*, 179(2):452–468, 2002.
- [16] J Blair Perot. An analysis of the fractional step method. *Journal of Computational Physics*, 108(1):51–58, 1993.
- [17] Hans Petter Langtangen, Kent-Andre Mardal, and Ragnar Winther. Numerical methods for incompressible viscous flow. *Advances in Water Resources*, 25(8):1125–1146, 2002.
- [18] Shervin Bagheri, Andrea Mazzino, and Alessandro Bottaro. Spontaneous symmetry breaking of a hinged flapping filament generates lift. *Physical review letters*, 109(15):154502, 2012.
- [19] Damiano Natali. A finite volume code for fluid-structure interaction. Private communication, 2014.
- [20] Gregor Wollensak and Eberhard Spoerl. Biomechanical characteristics of retina. *Retina*, 24(6):967–970, 2004.
- [21] Ian A Sigal, John G Flanagan, and C Ross Ethier. Factors influencing optic nerve head biomechanics. *Investigative ophthalmology & visual science*, 46(11):4189–4199, 2005.
- [22] Christopher Bowd, Robert N Weinreb, Brian Lee, Alireza Emdadi, and Linda M Zangwill. Optic disk topography after medical treatment to reduce intraocular pressure. *American journal of ophthalmology*, 130(3):280–286, 2000.
- [23] Mahmut Dogramaci and Tom H Williamson. Dynamics of epiretinal membrane removal off the retinal surface: a computer simulation project. *British Journal of Ophthalmology*, 97(9):1202–1207, 2013.
- [24] Jost B Jonas, Andrea Stroux, Isabel Velten, Anselm Juenemann, Peter Martus, and Wido M Budde. Central corneal thickness correlated with glaucoma damage and rate of progression. *Investigative ophthalmology & visual science*, 46(4):1269–1274, 2005.

- [25] Jost B Jonas, Eduard Berenshtein, and Leonard Holbach. Lamina cribrosa thickness and spatial relationships between intraocular space and cerebrospinal fluid space in highly myopic eyes. *Investigative ophthalmology & visual science*, 45(8):2660–2665, 2004.